

May 2021

Performance of Centrifugally Cast Austenitic Alumina-Forming Alloys in Coking and Decoking Environments

Lizeth Ortiz
University of Wisconsin-Milwaukee

Follow this and additional works at: <https://dc.uwm.edu/etd>



Part of the [Materials Science and Engineering Commons](#)

Recommended Citation

Ortiz, Lizeth, "Performance of Centrifugally Cast Austenitic Alumina-Forming Alloys in Coking and Decoking Environments" (2021). *Theses and Dissertations*. 2709.
<https://dc.uwm.edu/etd/2709>

This Dissertation is brought to you for free and open access by UWM Digital Commons. It has been accepted for inclusion in Theses and Dissertations by an authorized administrator of UWM Digital Commons. For more information, please contact scholarlycommunicationteam-group@uwm.edu.

**PERFORMANCE OF CENTRIFUGALLY CAST AUSTENITIC
ALUMINA-FORMING ALLOYS IN COKING AND DECOKING
ENVIRONMENTS**

by
Lizeth Ortiz

A Dissertation Submitted in
Partial fulfillment of the
Requirements for the Degree of

Doctor of Philosophy
in Engineering

at
The University of Wisconsin - Milwaukee
May 2021

ABSTRACT

PERFORMANCE OF CENTRIFUGALLY CAST AUSTENITIC ALUMINA-FORMING
ALLOYS IN COKING AND DECOKING ENVIRONMENTS

by

Lizeth Ortiz

The University of Wisconsin-Milwaukee, 2021
Under the supervision of Dr. Benjamin Church

Ethylene, the most-produced building block in the petrochemical industry, is produced using thermal cracking operations where reactor materials are exposed to high temperature aggressive environments that limit their life expectancy. These atmospheres degrade the reactor's material due to exposure to high temperatures, to carbon, to sulfur, and to other compounds, affecting negatively its process operations and therefore, its economics.

One of the most undesirable phenomena in ethylene thermal cracking operations is coking, where a carbon layer is deposited on the walls of the furnace tubes causing a reduction in the process efficiency as well as degradation of the alloy. This leads to an inevitable shutdown of the furnace tubes, or decoking, where steam is introduced to remove the carbon layer, causing higher operational costs and less energy efficiency of the plant. As a result, furnace tubes deteriorates with the successive coking-decoking cycles due to corrosion and carburization reducing the lifetime of the reactor material, and negatively impacting the process economics.

Currently, thermal cracking reactors are made of austenitic Fe-Ni-Cr heat resistance steels, or chromia-forming alloys, which form a protective chromium oxide layer during exposure. These alloys rely on chromia scales for protection from high temperature oxidation but their performance is limited in many industrial environments. More recently, research into materials which produce protective layers of aluminum oxide, or alumina-forming alloys, have been explored as a way to further slow the rates of high temperature oxidation and coke build-up. While studies on chromia-forming alloys used for ethylene production are

widely available, there is a lack of published scientific work understanding the performance of alumina-forming alloys in these petrochemical applications.

In this work, the coking resistance of several alumina-forming (3.2 to 4 wt% Al) alloys relative to a traditional chromia-forming (HP) alloy is described. An analysis of oxidation rates, coking kinetics, microstructural impacts of long-term exposure to coking conditions, and coking-decoking cyclic atmospheres are considered in this study. Through microstructural analysis, mechanical testing and kinetic studies, the materials were analyzed to characterize oxide layer formation, carbon build-up, carburization, and changes to the base metal microstructure.

Overall, the alumina-forming alloys showed superior performance in coking-related environments relative to the traditional HP alloy. Results show that the alumina-forming alloys gained approximately 80-95% less mass than that of the chromia-forming alloy after exposure to static coking and cyclic coking-decoking conditions. In addition, the AFA alloys had not major microstructural changes. In contrast, higher carbon build-up and severe carburization was found in the HP alloy. Furthermore, coking kinetic parameters were evaluated at 900, 950, and 1000 °C, in a ethylene-hydrogen atmosphere, and an estimation of the apparent carbon diffusion coefficient in the matrix of both AFA and HP alloys were obtained.

The information developed in this study will better support the use of AFA materials in petrochemical applications, such as ethylene thermal cracking operations. Additionally, coking kinetics and diffusion parameters of AFA alloys have now been measured, allowing for these parameters to be used as the metric for coke formation and relative indication of performance. Therefore, with a better understanding of the coking resistance of alumina-forming alloys, a higher productivity and a reduction in the operational costs can be achieved when implemented in thermal cracking operations.

To
my beloved husband
Samir Rosas

TABLE OF CONTENTS

LIST OF FIGURES	viii
LIST OF TABLES	xiii
ACKNOWLEDGMENTS	xiv
1 Introduction	1
1.1 Background	3
1.2 Current materials: Chromia-forming Alloys	4
1.3 Potential materials: Alumina-forming Alloys	5
1.3.1 Alloying additions	7
1.3.2 Crystal Structure	8
1.4 Chromia-forming vs. Alumina-forming alloys	8
1.5 Economics	10
1.6 Scope and Objectives of the thesis	12
1.7 Organization of the thesis	12
2 Preoxidation	14
2.1 Introduction	14
2.1.1 Thermodynamics of Oxidation	16
2.1.2 Kinetics of Oxidation	18
2.2 Methodology	20

2.2.1	Material composition	20
2.2.2	Sample preparation	21
2.2.3	Experimental conditions	22
2.2.4	Characterization	23
2.3	Results and discussion	24
2.3.1	Change of mass	24
2.3.2	Microstructural analysis of as-cast alloys	25
2.3.3	Microstructural analysis of oxidized alloys	27
2.4	Summary	30
3	Coking kinetics	32
3.1	Introduction	32
3.2	Theory	34
3.2.1	Determination of kinetics coking rate	36
3.2.2	Carburization attack	37
3.3	Methodology	40
3.3.1	Test materials and specimen preparation	40
3.3.2	Experimental conditions	41
3.3.3	Characterization	42
3.4	Results and Discussion	43
3.4.1	Determination of coking kinetics rate	44
3.4.2	Microstructural Analysis	51
3.4.3	Estimation of Apparent Carbon Diffusion Coefficient	62
3.4.4	Discussion of Coking Mechanism	68
3.5	Summary	70
4	Coking Long-term Performance	72
4.1	Introduction	72

4.2	Methodology	74
4.3	Results and Discussion	74
4.3.1	Determination of coking kinetics rate	74
4.3.2	Microstructural Analysis	77
4.4	Integrity of the oxide layer	88
4.5	Summary	91
5	Coking-Decoking Cyclic Conditions	93
5.1	Introduction	93
5.2	Methodology	94
5.2.1	Material composition	94
5.2.2	Sample preparation	95
5.2.3	Experimental conditions	95
5.2.4	Characterization	96
5.3	Results and Discussion	98
5.4	Conclusions	107
6	Conclusions	110
6.1	Future work	113
6.2	Acknowledgments	114
	Bibliography	115
	Curriculum Vitae	126

LIST OF FIGURES

1.1	US Ethane Production and Consumption.	4
1.2	Phase diagram of Fe-Cr-Al-(20, 25, 30) Ni-1Nb-2Mo-0.1C showing limitations of Cr and Al additions in a range of 600 to 1200 °C; and at 650, 700, 750 and 800 °C phases, predicted by thermodynamic calculation.	6
1.3	Superimposed ternary phase diagram of Fe-Cr-Ni near the Fe-rich corner at 1200 °C and at 800 °C.	6
1.4	A schematic representation of growth rate data and thermodynamic stability data for specific oxides.	9
1.5	Simulated run length and net annual decoking downtime of an industrial ethane cracker as a function of the reduction in coking rate.	11
2.1	BSE-SEM image from an AFA and an HP alloy tested at 800°C in air for 2000 hours.	15
2.2	BSE-SEM of an AFA alloy (4Al/0.6Nb/0.1Ti) after 100 h at 900 °C in air . .	16
2.3	Ellingham/Richardson diagram for metal oxides. Standard free energies of formation as a function of temperature.	17
2.4	Free energy changes, ΔG , expressed as oxygen potential for various oxidation reaction temperatures	18
2.5	Mass change of samples during steam pre-oxidation treatments at 915 °C. . .	19
2.6	Digital images of samples in the as-cast state	21

2.7	Experimental conditions for the Preoxidation Step	23
2.8	Specific change of mass after preoxidation.	25
2.9	Optical microscopy of as-cast samples of surface microstructure of AFA-3.8 alloy and HP alloy.	26
2.10	SEM cross-section of as-cast microstructure of AFA-3.8 alloy and HP alloy. .	26
2.11	EDS mapping cross-section of as-cast microstructure of AFA-3.8 alloy. . . .	27
2.12	EDS mapping cross-section of as-cast microstructure of HP alloy.	27
2.13	Digital images of some alloys after preoxidation	28
2.14	SEM cross-section of samples after preoxidation for a) AFA-3.8 alloy and b) HP alloy.	28
2.15	EDS mapping cross-section after preoxidation for AFA-3.8 alloy.	29
2.16	EDS mapping cross-section after preoxidation for HP alloy.	29
2.17	XRD analysis for the AFA-3.8 and the HP alloy after preoxidation.	30
3.1	Schematic depth profile illustrating a suggested mode of formation of nanoparticles of Ni that can act as potential catalytic agents for producing carbon filaments.	35
3.2	Example of carbon concentration profile based on a standard Fick's second law solution, and a Boltzmann-Matano analysis.	38
3.3	Specific change of mass at after exposure to coking conditions.	45
3.4	Specific change of mass per area for each AFA and HP alloys.	46
3.5	Regression data for each alloy exposed to coking conditions at three different temperatures for 100 h.	48
3.6	Arrhenius plots for each alloy for determination of coking kinetic parameters.	50
3.7	Digital images of alloys after exposure to coking conditions for 100 h. . . .	51
3.8	XRD analysis for the AFA and the HP alloy after exposure to 900, 950, and 1000 °C for 100 h at each temperature.	52

3.9	Optical microscopy images for the HP, AFA-3.2, AFA-3.5, and AFA-4.0 alloys after 100 h of exposure at 900, 950, and 1000 °C.	53
3.10	SEM cross-sectional images of the HP alloy after 100 h of coking.	55
3.11	SEM cross-sectional images of the AFA-3.2 alloy after 100 h of coking.	56
3.12	SEM cross-sectional images of the AFA-3.5 alloy after 100 h of coking.	57
3.13	SEM cross-sectional images of the AFA-4.0 alloy after 100 h of coking.	58
3.14	Profiles obtained from EDS analysis at three different temperatures for 100 h of coking for each alloy.	59
3.15	Example of EDS area spectrum performed on each sample. SEM image corresponds to the AFA-4.0 alloy exposed after 100 h at 950 °C.	60
3.16	Carbon profiles obtained from EDS analysis at three different temperatures for 100 h of coking.	61
3.17	Fitted curves to Fick’s second law solution model according to equation 3.10.	64
3.18	Apparent carbon diffusion coefficients as a function of carbon concentration, and distance, using Boltzmann-Matano analysis for the HP alloy.	66
4.1	Specific change of mass per surface area for alloys exposed to 950 °C for a total of 1000 h. Reported values correspond to 1 sample per material.	75
4.2	Regression data for AFA and HP alloys exposed to the coking atmosphere at 950 °C for 1000 h. Units are given in $\text{mg}\cdot\text{cm}^{-2}$ for $\Delta m/S$, and in hours for t	76
4.3	Digital images of alloys after 1000 h of exposure to coking conditions	77
4.4	XRD analysis for the AFA and the HP alloy after exposure to 950 °C for a total of 1000 h.	78
4.5	Optical microscopy images for the HP alloy after long-term exposure to coking atmosphere.	79
4.6	Optical microscopy images for the AFA-3.2 alloy after long-term exposure to coking atmosphere.	79

4.7	Optical microscopy images for the AFA-3.5 after long-term exposure to coking atmosphere.	80
4.8	Optical microscopy images for the AFA-4.0 alloy after long-term exposure to coking atmosphere.	80
4.9	Carburization depth measured by optical microscopy for the AFA and HP alloys.	81
4.10	SEM cross-sectional images of the HP alloy after 1000 h of coking.	83
4.11	SEM cross-sectional images of the AFA-3.2 alloy after 1000 h of coking. . . .	84
4.12	SEM cross-sectional images of the AFA-3.5 alloy after 1000 h of coking. . . .	85
4.13	SEM cross-sectional images of the AFA-4.0 alloy after 1000 h of coking. . . .	86
4.14	Profiles obtained from EDS analysis after 1000 h of coking at 950 °C.	87
4.15	Carbon profiles obtained from EDS analysis after 1000 h of exposure.	88
4.16	High magnification SEM cross-sectional images of samples after exposure to coking conditions for 1000 h.	89
4.17	EDS analysis of the HP alloy after 1000 h of exposure to coking conditions. .	90
4.18	EDS analysis of the AFA-3.2 alloy after 1000 h of exposure to coking conditions.	90
4.19	EDS analysis of the AFA-3.5 alloy after 1000 h of exposure to coking conditions.	90
4.20	EDS analysis of the AFA-4.0 alloy after 1000 h of exposure to coking conditions.	91
5.1	Schematic representation of the cyclic coking-decoking experiments	96
5.2	Digital images of alloys after each step in a coking-decoking cycle.	98
5.3	Specific change of mass per area for each coking-decoking cycle. Filled markers denote coking and open markers denote decoking step.	100
5.4	XRD analysis at each stage.	101
5.5	Optical microscopy images after coking cycle 10, for AFA-3.8-3.8 alloy and HP alloy.	103
5.6	Optical microscopy images after decoking cycle 10 for AFA-3.8-3.8 alloy and HP alloy.	103

5.7	SEM cross sections after coking cycle 10, for AFA-3.8 alloy and HP alloy. . .	104
5.8	EDS mapping cross-section after coking cycle 10 for AFA-3.8 alloy.	105
5.9	EDS mapping cross-section after coking cycle 10 for HP alloy.	105
5.10	SEM cross sections after decoking cycle 10, for AFA-3.8 alloy and HP alloy. .	105
5.11	EDS mapping cross-section after decoking cycle 10 for AFA-3.8 alloy.	106
5.12	EDS mapping cross-section after decoking cycle 10 for HP alloy.	106
5.13	Microhardness distribution of each alloy at each stage.	107

LIST OF TABLES

1.1	Comparison of Al_2O_3 vs. Cr_2O_3 oxide scales.	10
2.1	Nominal compositions of the alloy samples in wt.%.	20
2.2	Average surface area of 15 samples per alloy exposed to preoxidation conditions.	21
3.1	Activation Energy reported by other authors in similar cracking environments.	37
3.2	Reported carbon diffusion coefficient at temperatures of interest.	40
3.3	Nominal compositions of the alloy samples in wt.%. Other alloying additions (Nb, Mo, C, etc.) complete 100%.	41
3.4	Test conditions.	42
3.5	Mass of gained respect to the HP Alloy	44
3.6	Rate constant (k) and time exponent of the rate law (n) for all tests.	47
3.7	Calculated Activation Energy and pre-exponential factor.	49
3.8	Calculated D_{app} using Fick's solution for the AFA alloys.	63
3.9	Calculated D_{app} using Fick's solution for the HP alloy. Units are given in $\text{cm}^2\cdot\text{s}^{-1}$	65
3.10	Apparent Carbon diffusion coefficients for the AFA and the HP alloys obtained from each model.	68
4.1	Rate constant (k) and time exponent of the rate law (n) for long-term test. .	76
5.1	Nominal compositions of the alloy samples	95

ACKNOWLEDGMENTS

During my graduate studies, I have learned and grown both professionally and emotionally. I have had the opportunity to play different roles. I have been a student, a TA, a lecturer, a mentor, a mentee, and mostly, a researcher. I have so many good memories, and stories that have shaped me into the person I am today, and for that, I am grateful to each person I have encountered during my time at UWM.

I would like to express my gratitude to my advisor, Dr. Benjamin Church. His guidance and continuous support showed me what a good advisor is, and how I want to be once I have students under my supervision. I definitely consider him as a role model, and my friend.

I would like to thank Dr. Abu-Zahra, who supported me with funding for my graduate studies. I learned so much with each teaching experience.

Additionally, Dr. Abu-Zahra, Dr. Hardscastle, Dr. Otieno and Dr. Rohatgi, thank you all for being part of my PhD committee. Your insight provided enhanced my dissertation. Each interaction I had with you was very enriching for my research and professional life.

Finally, I must express my gratitude to my husband and my parents, for providing me with unfailing support and continuous encouragement throughout my graduate studies. This accomplishment would not have been possible without them.

Chapter 1

Introduction

Thermal cracking operations are used for manufacturing of petrochemical intermediate feedstocks such as ethylene or propylene from alkanes such as ethane, propane, butane, naphtha and gas oil. During these operations, reactor materials are exposed to high temperature aggressive environments that limit their life expectancy. These atmospheres degrade the reactor's material due to exposure to high temperatures, to carbon, to sulfur, and other compounds, affecting negatively its process operations and therefore, its economics.^[1,2]

One of the most undesirable phenomena in thermal cracking operations is called coking, where carbon deposition from a gas phase leads to carbon build-up causing a reduction in the process efficiency as well as corrosive attack and degradation of the alloy. During coking, a continuous layer of coke is formed on the inner walls of the tubes reactors reducing the heat transfer across the reactor wall, increasing the reactor tube metal temperature to 1100 - 1200 °C, and increasing the pressure to more than 1.5 atm.^[3,4] This leads to an inevitable shutdown of the furnace tubes for removing of carbon build-up, or decoking, which increases the operational costs and reduces the energy efficiency of the plant. In addition, the furnace tube material deteriorates with the successive coking-decoking cycles due to corrosion and carburization causing a need for replacement of the reactor coils every 4 to 10 years.^[5] Therefore, an understanding of the coke formation and its removal, is desirable to reduce

carbon build-up such that the run length of the furnace tubes increases, which leads to a higher productivity and less operating costs.

Among all thermal cracking operations, the production of ethylene is of particular interest because it is the most-produced building block in the petrochemical industry. The ethylene production process and other petrochemical processes can be improved by developing materials that resist coking, retain long-term oxidation and corrosion resistance, and yet remain economically favorable for implementation. Typical alloys used in these applications are austenitic Fe-Ni-Cr heat resistance steels which form a protective chromium oxide layer during exposure. The chromia layer acts as a diffusion barrier that restricts the transport of gas-phase constituents (oxygen, carbon) and alloy constituents (Fe, Ni, Cr, and others) so that the inevitable reactions between the gas and solid are slowed.^[1,6] These heat resistant stainless steels rely on chromia scales for protection from high temperature oxidation but their performance is limited in many industrial environments. Depletion of chromium in the alloy due to carburization can degrade the alloy's ability to regenerate a protective oxide scale thus resulting in faster coke build-up and further carburization.

More recently, research into alloys which produce protective layers of aluminum oxide have been explored as a way to further slow the rates of high temperature oxidation and coke build-up.^[2,7] Alumina-forming austenitic stainless steel alloys are thought to be an alternative to the traditional alloys due to a more stable oxide scale as well as superior corrosion and creep resistance for many industrial environments.^[8] The protective oxide layer enables the use of these alloys at higher temperatures and for longer periods of time than stainless steel alloys that form a protective chromium oxide layer. This aluminum oxide layer makes them suitable for a wide range of energy production, chemical, and process industry applications, where the use of more durable materials capable of withstanding higher temperatures can result in significant cost and energy savings as well as reduction in environmental emissions.^[9]

1.1 Background

Ethylene, the most-produced building block in the petrochemical industry, is produced by pyrolysis of ethane using steam crackers operating around 900 - 1000°C. Operating in this temperature range results in a higher ethylene selectivity compared to other heavier paraffins.^[1,2,6] In addition to high temperature operations, thermal cracking atmospheres involves high carbon activity, in the range of 100 to 1000, and oxygen partial pressures, in the range of 10^{-16} to 10^{-20} .^[6,7] These conditions result in deterioration of mechanical properties of the reformer tubes which is more pronounced at the surface than in the bulk of the material due to carburization, oxidation, creep, thermal cycling, and coking.^[10-12]

Ethylene (C_2H_4) is used as a raw building block for many industrial critical materials such as polyethylene, PVC, polystyrene, ethylene glycol, and countless other products. The annual world-wide production is over 100 million tons with US production representing roughly 25% of the total. US based production has increased from an average of 0.717 million barrels per day (b/d) in 2000 to 2 million b/d in 2021¹. More than half of the production of ethylene is used to produce polyethylene, one of the most important materials today. The market grows continuously with an average rate of 4% worldwide and can be related to the gross national product growth in an area or a certain country.^[13]

The leading technology applied for production of ethylene is steam cracking, a high temperature pyrolysis in the presence of steam, which was developed in the 1960s, and has remained largely unchanged since that time.^[13] Ethane is mainly used as a petrochemical feedstock for the production of ethylene, which is a building block for plastics, resins, and other industrial products. As shown in Figure 1.1, U.S. ethane consumption is increasing as existing ethylene crackers have expanded and new plants have begun operating. The systems for producing this raw chemical incorporate large reactors that are made of alloys that provide 1) high temperature mechanical strength and 2) chemical resistance to attack

¹U.S. Energy Information Administration. "U.S. Gas Plant Production of Ethane-Ethylene". www.eia.gov. Accessed on 01/17/21

under the aggressive carbon-rich conditions of the system.^[14] Therefore, such applications demand an optimum combination of microstructural stability, creep resistance, excellent oxidation resistance, and additionally, resistance to coking and carburization in case of ethylene pyrolysis applications.

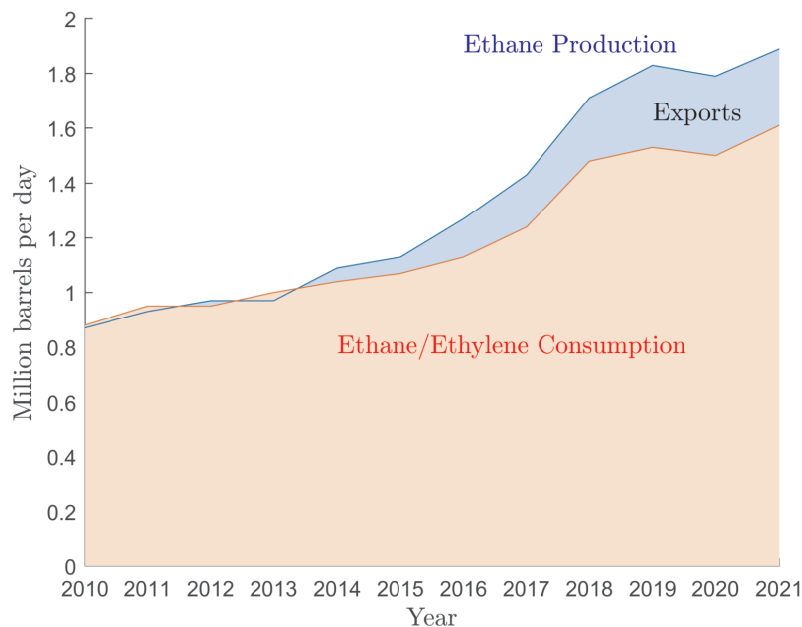


Figure 1.1: US Ethane Production and Consumption.

1.2 Current materials: Chromia-forming Alloys

Traditionally, ethylene production reactors have used cast heat resistant austenitic stainless steel alloys such as High-Performance (HP) alloys.^[15] These HP alloys form chromium oxide scales during exposure to oxidizing conditions and are classified as chromia-forming austenitic alloys.

Chromia-forming alloys use Cr_2O_3 -based scales for protection. Chromium is used primarily to its easy formation of a passive layer and therefore good corrosion resistance.^[16] However, this chromia scale can be susceptible to accelerated oxidation in the presence of water vapor.^[17] The excellent metallurgical compatibility of chromium in Fe/Fe(Ni) allows

ready formation of a protective Cr_2O_3 -based scale with wide alloy design flexibility optimizing oxidation resistance with other needed properties such as creep resistance, weldability, etc.^[18] Because they combine good creep strength and oxidation resistance, are widely used in energy production and chemical processing environments. However, strong oxidation, carburization, sulfidation or nitriding can occur if the environment does not promote chromium oxide formation or if the protectivity of the scale is destroyed by other mechanisms.^[7,14,16]

1.3 Potential materials: Alumina-forming Alloys

Alumina-forming austenitic stainless steels have been recently developed for structural use in aggressive oxidizing environments at 600-900 °C. These alloys show a promising combination of oxidation resistance, creep resistance, tensile properties, and potential for good welding behavior. Recently investigations indicate the potential to achieve superior oxidation resistance compared to conventional Cr_2O_3 -forming iron- and nickel- based heat-resistant alloys.^[18] This is due to the slower growth rate and greater stability of alumina, particularly in the presence of water vapor species encountered in many industrial process and energy production environments.^[19]

Studies have shown that these alloys have potential in process environments involving aggressive water vapor, carbon, and sulfur species in temperatures ranging from 500 to 900 °C.^[14] It is speculated that the key factor controlling how long Al_2O_3 scale formation occurs in AFA alloys is oxygen solubility in the alloys. To promote protective Al_2O_3 scale formation, it has been explored that alloying addition levels of 3-6 wt.% aluminum and 10-25 wt.% chromium can destabilize the parent austenitic matrix structure, resulting in duplex ferritic/austenitic microstructure and a loss of creep resistance. This structure can be stabilized by additions of nickel so the AFA alloys can develop a good oxide scale and retain good creep resistance for the application as shown in Figure 1.2 and Figure 1.3.^[18]

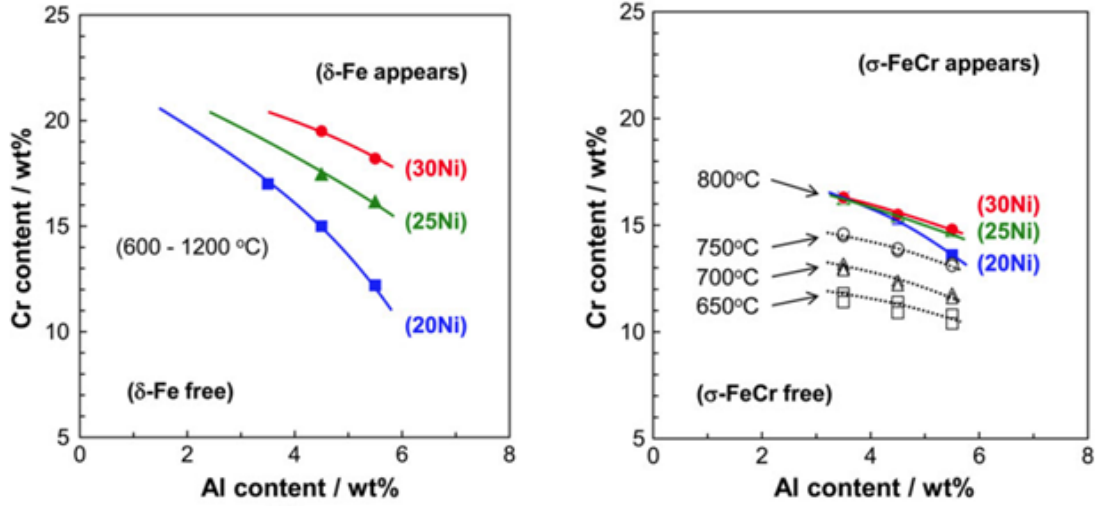


Figure 1.2: Phase diagram of Fe-Cr-Al-(20, 25, 30) Ni-1Nb-2Mo-0.1C showing limitations of Cr and Al additions in a range of 600 to 1200 °C; and at 650, 700, 750 and 800 °C phases, predicted by thermodynamic calculation.^[20]

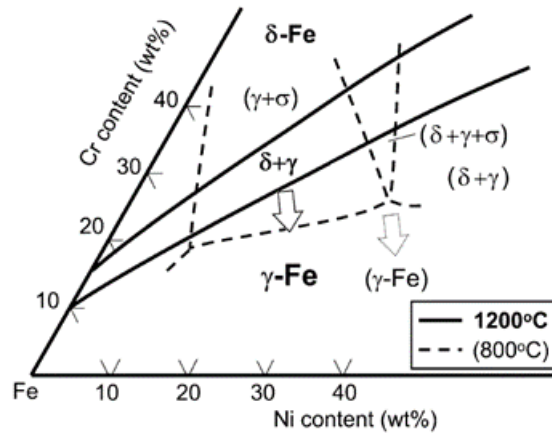


Figure 1.3: Superimposed ternary phase diagram of Fe-Cr-Ni near the Fe-rich corner at 1200 °C (bold lines) and at 800 °C (broken lines). Arrows indicate the direction of phase boundaries shifting by the Al addition due to the strong δ -Fe stabilizing effect of Al relative to γ -Fe.^[20]

The AFA alloys are intended to offer better chemical resistance to the steam and carbon-rich atmospheres found in thermal cracking operations, such as those used in ethylene production. By forming aluminum oxide scales instead of chromium oxide scales upon exposure to oxidizing conditions, these alloys serve as a promising choice in materials selection for the steel reactors.

1.3.1 Alloying additions

Studies on the alloy composition have explored the effects of alloying additions on oxidation and creep behavior concluding:

- It has been identified that AFA alloys with a relatively low Al and Cr contents (2.5 to 4 wt.% and 14 to 15 wt.% respectively, have formed alumina scale and permitted stabilization of an FCC austenitic matrix phase for creep strength with low additions of Ni.^[9]
- Niobium additions (0.6 to 3 wt.% Nb) seems to enhance the oxidation resistance, particularly in water-vapor containing environments.^[9,18]
- Increasing niobium, aluminum, and/or nickel content all favor the establishment and maintenance of protective Al_2O_3 scale formation in these alloys.^[21]
- Some tolerance for vanadium and titanium is important because they can be used to enhance MC carbide formation for improved creep resistance.^[18]
- Use of nitrogen, titanium, and vanadium degrade the ability to form an alumina a surface layer in the AFA composition range and must be minimized.^[9]
- Alloys can be strengthened by gamma prime precipitates (γ' -Ni₃Al) with the proper balance of Al, Ni, Nb, and Ti additions.^[9]
- Carbides precipitates should be incorporated for creep strength.^[9] C levels of 0.3 – 0.4 wt.% C are required to balance creep properties with oxidation resistance.^[18]
- It has been found that cast AFA alloys containing 14wt.% Cr - 3.5 wt.% Al with approximately 25 wt.% Ni are restricted to maximum operating temperatures of 800 - 850 °C depending on the water vapor levels in the environment.^[22]
- The creep resistance of the alloys seems to be strongly dependent on the level of Nb additions. Al additions also help to increase the creep resistance.^[23]

1.3.2 Crystal Structure

Ferritic Fe-Cr-Al-based alloys capable of forming Al_2O_3 are widely used in specialty applications such as heating elements and furnace liners. However, they are not suitable for structural applications above 500 - 600 °C because of their poor creep resistance resulting from their open body-centered cubic structure. Investigations have shown that to obtain a good creep resistance, an austenitic face-centered cubic structure is needed. Austenitic stainless steel has a face-centered cubic (FCC) crystal structure that is stabilized by nickel; exhibits better high-temperature creep strength than ferritic stainless steel, which features a body-centered cubic (BCC) crystal structure. Studies in the role of Manganese in the high-temperature oxidation resistance of AFA alloys have been done above 800 °C in air and in air with 10% water vapor.^[24] Manganese is a strong face-centered cubic stabilizer and much cheaper than nickel, usually added into austenitic steels to realize solid-solution strengthening, stabilize the austenite matrix, and reduce the raw material cost. AFA alloys usually have between 1% and 2% Mn, but its role in the oxidation process is not well clarified yet. Researchers have found that excessive additions of Mn in AFA alloys tend to stimulate formation of the coarse spinel $\text{CrMn}_{1.5}\text{O}_4$ and Cr_2O_3 which is responsible for the degradation in the oxidation performance. Therefore, exists an upper limit for the Mn addition, and the tolerable amount of Mn in these alloys is decreased with the increase of the service temperatures and presence of water vapor. Also, the oxidation resistance is moderately degraded with additions of larger than 1% Mn at 800 °C, even in dry air.^[24]

1.4 Chromia-forming vs. Alumina-forming alloys

Different types of low cost Fe- and Ni- based alloys are widely used to meet the requirements of heat exchangers, steam crackers or tubes in the petrochemical applications. However, because of higher operating temperature and aggressive environment, most of the materials are not suitable for such applications. Above 700 °C, the commonly used alloys are suscep-

tible to severe oxidation and creep deformation. The presence of water vapor (especially during the decoking process), accelerates the rate of oxidation and increases Cr evaporation. The stability and the performance of the alloys are influenced by several factors such as microstructure, grain size, chemical composition, phase precipitation, scale formation, and operating temperature.^[26]

Al_2O_3 scales offer a superior degree of protection to Cr_2O_3 scales in many high-temperature environments.^[18,25] Studies of the chromium evaporation from chromia and alumina forming alloys at 850 and 950 °C for 500 h in air containing 2.6% and 12% water vapor have shown that chromium evaporation rate from thermally grown alumina scales is approximately two orders of magnitude lower than that formed on a conventional chromia forming alloy.^[26] It has been concluded that lower Cr evaporation rate in the alumina-forming alloy is due to the development of thin protective alumina scale on the surface along with the formation of Cr, Fe and Ni-rich islands.

A comparison of the advantages and disadvantages of the alumina scale versus chromia scale is presented in Table 1.1. Additionally, thermodynamics information regarding oxide scales is shown in Figure 1.4.

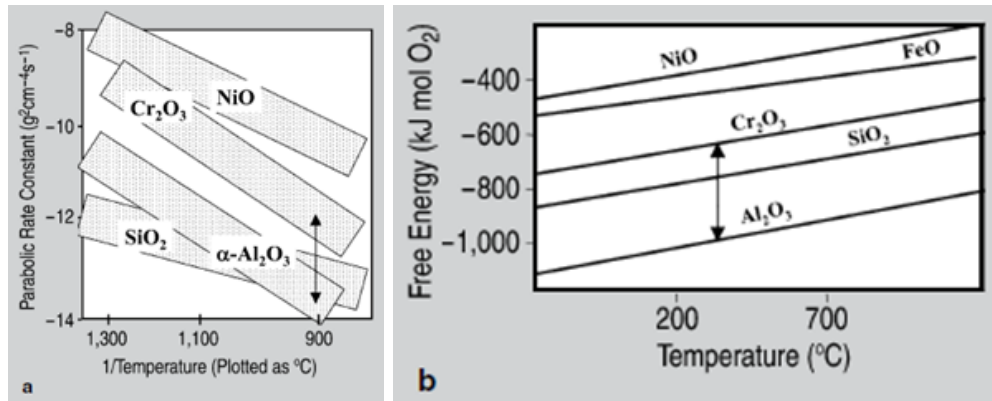


Figure 1.4: A schematic representation of (a) growth rate data and (b) thermodynamic stability data for specific oxides. The arrows mark differences between Al_2O_3 and Cr_2O_3 .^[18]

Table 1.1: Comparison of Al_2O_3 vs. Cr_2O_3 oxide scales.

AFA alloys	HP Alloys
Al_2O_3 scales grow at a rate that is 1 to 2 orders of magnitude lower than that of Cr_2O_3	The presence of water vapor accelerates the rate of oxidation and increases Cr evaporation.
Diffusion of carbon (D_C) is lower through alumina than chromia. Aluminum additions also reduce D_C within austenitic matrix.	Diffusion of carbon occurs due to presence of a porous, non-uniform chromia layer that allows carbon ingress.
Alumina is more thermodynamically stable to higher temperatures and for longer time periods than chromia. $\text{Al}_2\text{O}_3 > \text{SiO}_2 > \text{Cr}_2\text{O}_3$	Loss of Cr through evaporation of Cr_2O_3 and/or $\text{CrO}_2(\text{OH})_2$ at high oxygen partial pressures $>1850^\circ\text{F}$ (1000°C) which represents a temperature limitation.
Greater stability in the presence of water vapor. Significant oxidation volatility is not typically observed until temperatures reach 1200°C .	Volatile chromium oxy-hydroxide species can form and significantly reduce oxidation lifetime of the alloy.
A uniform and dense alumina scale can reduce the propensity for catalytic coke formation.	Local breakdowns in scale and subsequent transport of carbide or Fe ions to surface act as nucleation sites for catalytic coking.
It has been proven to be particularly beneficial in the presence of aggressive carbon- or sulfur-species encountered in combustion and chemical process industry applications.	Above 1900°F (1040°C) in the presence of carbon (i.e. coke layer), Cr carbide is thermodynamically favorable and its formation will cause eventual failure of oxide layer.

1.5 Economics

In this section, the results of simulations of ethylene steam cracking operations done by Andrés Muñoz Gandarillas are presented.^[27] The author estimated the potential economic benefits of using specialized coils materials in thermal cracking reactors by simulating a process taken as a base a coil that is made of a typical high-temperature alloy. The base case simulation predicted a run length of 48 days. Then, assuming the same process conditions, the run length when the coking rate was reduced in steps of 5% was calculated. Results are presented in Figure 1.5.

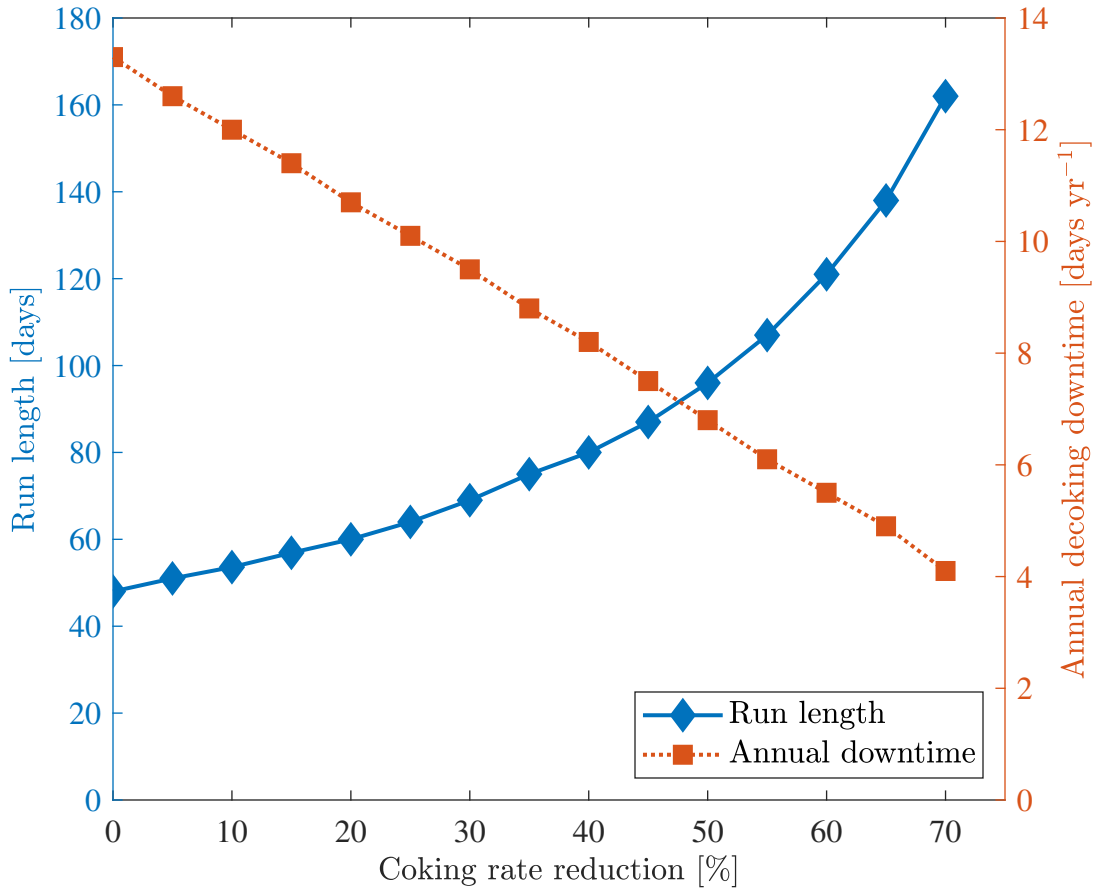


Figure 1.5: Simulated run length and net annual decoking downtime of an industrial ethane cracker as a function of the reduction in coking rate. Data was taken from Muñoz Gandarillas, Andrés thesis.^[27]

As shown in Figure 1.5, it can be seen that the implementation of materials that reduce the coking rate have a positive impact on the run length of the reactor, and therefore, reduces the annual downtime of the process operations. With the implementation of new materials such as AFA alloys, when a 10% reduction of coking rate is achieved, the profit margin of the process can increase by 85000 US\$ per year, compared to a traditional alloy.^[27] These values are an estimation of the potential benefits that new materials, such as AFA alloys, can bring into the costs of ethylene production by reducing the coking rates in the reactors.

1.6 Scope and Objectives of the thesis

Cast heat resistant tube alloys used for ethylene production are limited due to carbon diffusion, and carburization that occurs during exposure to high carbon containing atmospheres. Extensive literature on chromia-forming alloys used in ethylene cracking operations is widely available. However, there is a lack of published scientific work understanding the AFA alloys in petrochemical applications. Detailed studies comparing the performance of chromia-forming alloys and alumina-forming alloys are needed to support the wider adoption of the AFA alloys in petrochemical processing systems. This research will set to contribute to the study of coking and decoking kinetics in ethane-hydrocarbon atmospheres. An analysis on the change of mass, observation of microstructural changes, and mechanical strength will be discussed. Furthermore, additional data such as coking kinetic parameters, carbon diffusion coefficients, and element profiles will be discussed.

Futhermore, the following research objectives were established:

- To describe the oxide performance of both AFA and HP alloys in coking conditions.
- To estimate the coking kinetic parameters and carbon diffusion coefficient of AFA alloys.
- To describe the coking resistance of AFA alloys in long-term coking conditions.
- To evaluate the performance of AFA alloys in coking-decoking cyclic conditions.

1.7 Organization of the thesis

This dissertation shows the performance of AFA alloys against a traditional HP alloy after exposure to oxidation, coking, and decoking environments. The organization of the document is as follows:

- Chapter 2 introduces the results obtained from the preoxidation step. All alloys were exposed to a 100% steam environment before exposure to coking and/or decoking conditions. The purpose of this step was to form the oxide layer at the surface, same as the process encountered when new tubes are placed into service.
- Chapter 3 presents the results obtained after exposure to coking conditions at three different temperatures. Estimation of coking kinetic parameters, carbon diffusion coefficient, and microstructural changes is discussed in this chapter.
- Chapter 4 presents the results obtained after exposure to long-term coking conditions. A description of the performance of the alloys based on microstructural changes, carbon diffusion and carburization is discussed.
- Chapter 5 presents the results obtained after exposure to 10 coking-decoking cycles. A discussion of the effect of exposure to continuous coking-decoking atmospheres is done based on microstructural changes, mechanical properties and stability of oxide layer.
- Chapter 6 gives a summary of the main findings and future direction of the work.

Chapter 2

Preoxidation

The aim of this chapter is to present the results of the preoxidation treatment of alumina-forming alloys and chromia-forming alloys. The preoxidized alloys were later exposed to coking or coking-decoking cyclic conditions. Data collected includes change in mass data, and microstructural analysis after preoxidation, compared to the as-cast state. Data presented in this section has been previously published.^[28]

2.1 Introduction

The oxidation phenomenon is considered as the most important corrosion reaction at high temperature and is one of the primary considerations that determine the durability of heat-resistant alloys. The metals and alloys oxidize when are exposed to air or environments with high oxygen potential, at elevated temperature with a strong effect of temperature over oxidation rate^[29]. The key factor for a good oxidation resistance is to establish an external, continuous layer of a slow-growing, thermodynamically stable oxide phase.^[18] For high-temperature applications, such as higher than 600 °C, Cr_2O_3 and Al_2O_3 are the principal oxides used for the protection of metallic alloys.

Studies on centrifugally cast AFA alloys in an oxidation environment of air with 10 vol.% water vapor, and laboratory air (no added water vapor) have been done.^[22] Oxidation

exposures were conducted in 100 h cycles at 750 and 800 °C, and 800 °C and 900 °C for 1000 - 2000 h using 500 h cycles respectively. Their results show that the oxidation resistance of the AFA alloys was superior to the chromia-forming alloys (HK¹ and HP² steel). Figure 2.1 shows a BSE-SEM images of an AFA and a HP alloys after exposure to air for 2000 hours at 800 °C. It is noticeable that the oxide layer formed by the AFA alloys is thinner than that of the formed by the HP alloys. In addition, it was reported that in some regions of the AFA alloys, the oxide layer was multi-layered, with the outside layer comprising of a locally nodular-like Fe-Ni-Cr rich oxide, undercut by a continuous alumina layer. The oxide on HP was multilayered in some regions as well, with the same nodular-like Fe-Ni-Cr rich oxide followed by an interior layer being rich in Cr.^[22]

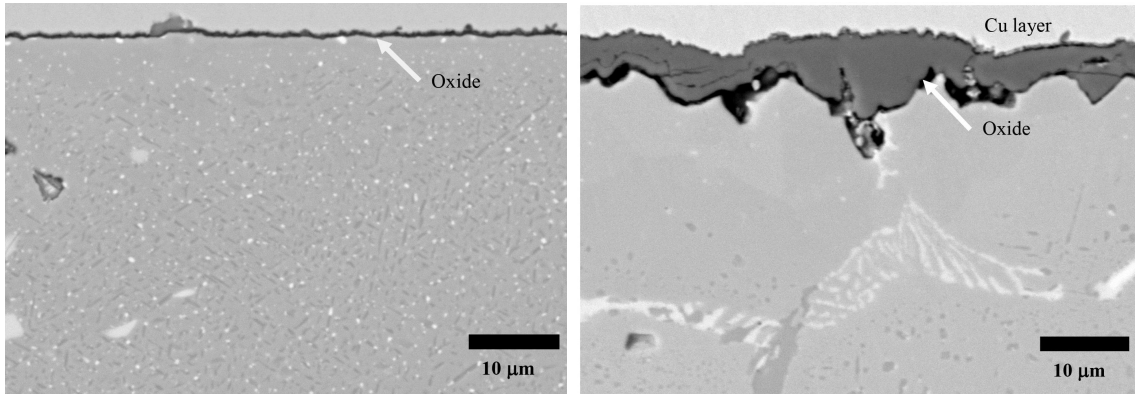


Figure 2.1: BSE-SEM image from an AFA and an HP (right) alloy tested at 800°C in air for 2000 hours.^[22]

Since the formation of the alumina scale in the AFA alloys occurs at a slow growth rate, the change in mass for the samples after exposure, even after 5000 h has been reported as a positive mass gains around $<0.5 \text{ mg}\cdot\text{cm}^{-2}$.^[30] These small changes in mass are consistent with protective alumina scale formation in the range of a few microns thick.^[6] Additionally, researches have found that Al_2O_3 scale consists primarily of Al and O, with only minor amounts of Cr, Fe, Mn, and Nb.^[22] Oxidation tests of AFA alloys (rage composition of 20 wt.% Ni - 12-14 wt.% Cr - 2.5-4 wt.% Al) for 1000 hours in air and in air-10% water vapor

¹HK austenitic s.s.: 24-28 wt.% Cr, 18-22 wt.% Ni

²HP austenitic s.s.: 24-28 wt.% Cr, 33-37 wt.% Ni

environments have been done.^[20,23,30] Results have shown that AFA alloys did not form protective alumina scales at 1000 °C in air. However, excellent oxidation resistance at 650 and 700 °C was observed. The loss of protective oxidation behavior was associated with a transition to internal oxidation and nitridation of Al. Furthermore, the solubility of Al in the austenitic matrix is on the order of 2 to 2.5 wt.% Al, so that the higher-Al containing alloy, exhibited second phase dispersion of B2[(Ni,Fe)Al] acting as a Al reservoirs for the growth of alumina scales as shown in Figure 2.2.^[30]

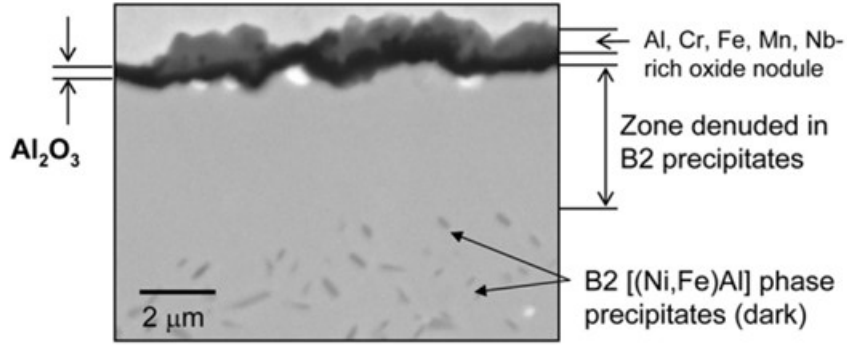


Figure 2.2: BSE-SEM of an AFA alloy (4Al/0.6Nb/0.1Ti) after 100 h at 900 °C in air.^[30]

2.1.1 Thermodynamics of Oxidation

Thermodynamically, it is probable the formation of an oxide over a metal surface when the oxygen potential in the atmosphere is higher than the partial pressure of oxygen in equilibrium with the oxide. This partial pressure in equilibrium could be determined from the standard free energy change (ΔG) for the oxide formation, considering the reaction:



$$\Delta G = -RT \ln \left(\frac{a_{MO_2}}{a_M P_{O_2}} \right) \quad (2.2)$$

Assuming the metal and oxide activities as the unity, the P_{O_2} can be expressed as:

$$P_{O_2} = \exp\left(\frac{\Delta G}{RT}\right) \quad (2.3)$$

The standard free energy of formation for various oxides as a function of temperature and the relative partial pressures of oxygen in equilibrium with the oxide are summarized in Ellingham/Richardson diagram as shown in Figure 2.3. From this diagram, it is possible to determine the potential of oxygen in oxidizing atmospheres (P_{O_2}) and reducing atmospheres with gas mixtures (P_{CO}/P_{CO_2}).^[14] Comparing the oxygen potential in the gaseous environment with the oxygen partial pressure in equilibrium with the evaluated oxide, it is possible to determine thermodynamically if this is stable or not under conditions worked in the laboratory.

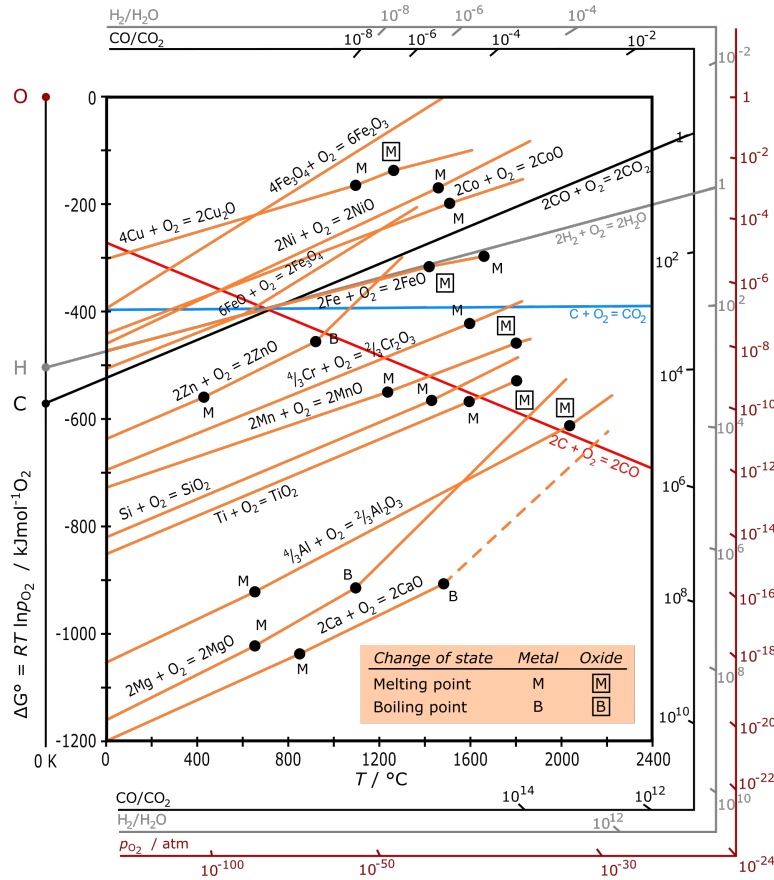


Figure 2.3: Ellingham/Richardson diagram for metal oxides. Standard free energies of formation as a function of temperature.

Moreover, researches have used published algorithms to evaluate the free energy changes, ΔG , for the various oxidation reactions that can take place in the metal's surface. As shown in Figure 2.4, it can be seen that for the temperatures of 850 - 915 °C, which are the temperatures worked in this research, ratios of 10^2 to 10^3 of H_2/H_2O are required to form a Cr_2O_3 scale oxide on the surface of the metals.^[31]

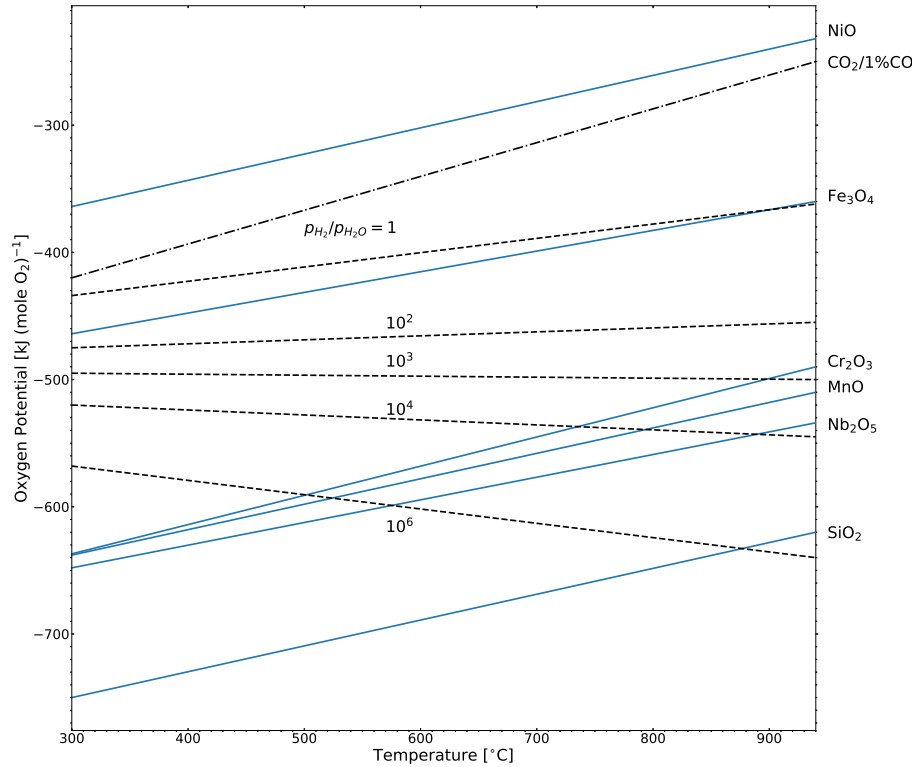


Figure 2.4: Free energy changes, ΔG , expressed as oxygen potential for various oxidation reaction temperatures.^[31]

2.1.2 Kinetics of Oxidation

Kinetics studies of the relative oxide formation of a traditional chromia-forming alloy (35Cr-45Ni-0.4C) against two alumina forming alloys (27Cr-35Ni-0.4C) containing varying amounts of aluminum (2.7 wt.%Al and 2.6 wt.%Al) have been published.^[32] The purpose of the oxidation treatment was to produce a stable surface oxide on the samples. Their environment

conditions were 850 °C for 12 h and raised the temperature up to 915 °C for 1, 10 and 100 hours in 100% steam. They concluded that the alumina forming alloys had parabolic oxidation kinetics while the chromia forming alloy had significant departures from parabolic behavior likely due to chromia volatilization. Furthermore, both alumina-forming alloys were able to form a continuous layer during 100% steam oxidation. The chromia-forming alloy showed mass changes that were non-linear with the root of time indicating that is likely to had competing mechanisms of a) oxidation and b) chromia volatilization that resulted in the observed mass change behavior.

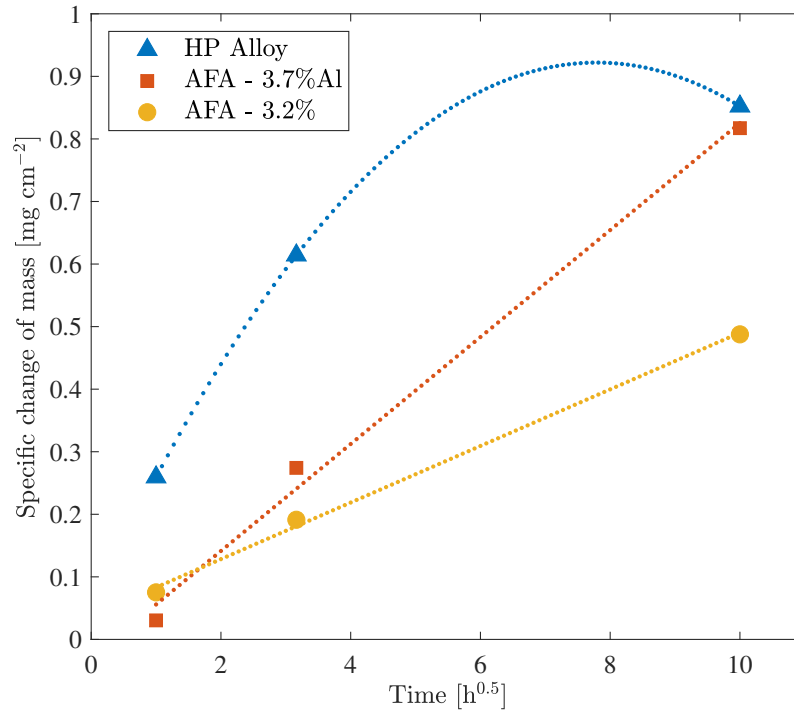


Figure 2.5: Mass change of samples during steam pre-oxidation treatments at 915 °C. Linear trend lines were forced to originate at the origin to emphasize ideal parabolic ($\Delta m \propto t^{0.5}$) kinetics.^[32]

2.2 Methodology

2.2.1 Material composition

Several AFA alloys and one HP alloy, all produced via centrifugal casting, were exposed to preoxidation conditions. The nominal composition for each alloy is described in Table 2.1, with elements related to mechanical strengthening (Nb, Mo, C, etc.) omitted due to proprietary nature. The production process used for the sample tubes was performed by a foundry engaged in the commercial production of ethylene tubes. Digital images of the samples are shown in Figure 2.6.

Table 2.1: Nominal compositions of the alloy samples in wt.%. Other alloying additions (Nb, Mo, C, etc.) complete 100%.

Material	Al	Cr	Fe	Ni
HP	0	26	35	34
AFA - 2.6	2.6	28	27	38
AFA - 3.1	3.1	29	17	46
AFA - 3.2	3.2	28	27	38
AFA - 3.5	3.5	28	25	38
AFA - 3.7	3.7	26	28	37
AFA - 3.8	3.8	23	34	37
AFA - 3.9	3.9	27	25	38
AFA - 4.0	4	23	33	37

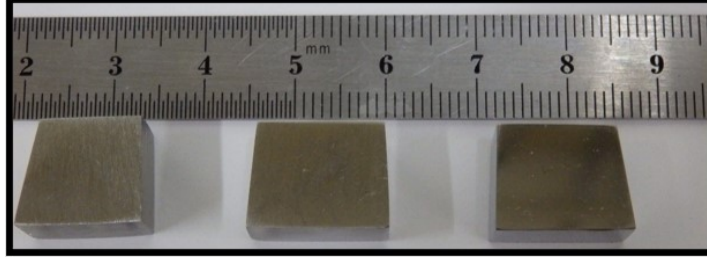


Figure 2.6: Digital images of samples in the as-cast state

2.2.2 Sample preparation

Samples were prepared from as-cast pipe sections, cut with an abrasive saw, ground to 1200-grit SiC abrasive paper on all sides to avoid surface interactions, cleaned with deionized water, and dried with compressed air. Average surface areas are shown in Table 2.2.

Table 2.2: Average surface area of 15 samples per alloy exposed to preoxidation conditions.

Alloys	Average Surface Area [cm ²]
HP	3.80 ± 1.2
AFA - 2.6	3.22 ± 0.5
AFA - 3.1	3.16 ± 0.3
AFA - 3.2	3.33 ± 0.6
AFA - 3.5	3.38 ± 0.8
AFA - 3.7	4.70 ± 1.1
AFA - 3.8	1.80 ± 0.5
AFA - 3.9	2.88 ± 0.8
AFA - 4.0	2.79 ± 0.8

2.2.3 Experimental conditions

Preoxidation test was carried out in a tube furnace, model XST-3-0-24-3V2 eXPRESS-Line by Thermcraft Incorporated, with a quartz tube (51 mm OD, 45 mm ID, 1000 mm length). The three-zone furnace was controlled to create a wide uniform temperature zone that was determined to fluctuate by less than ± 1 °C over 36 cm at a nominal 850 °C setpoint.

Argon gas (99.999% UHP) was flowed at $200 \text{ mL}\cdot\text{min}^{-1}$ through the system for 1 hour to pre-purge the system of air.

Deaerated water was pumped at a rate of $0.5 \text{ mL}\cdot\text{min}^{-1}$ using a peristaltic pump and passed through a glass helical tube, encased in a small secondary tube furnace set at 400 °C to produce steam. The steam was then flowed through heated tubing to prevent condensation and into the main tube furnace. Steam was flowed for 2 hours with the main tube furnace set to 200 °C such that the steam flow produced a steady condensate drip at the exhaust end of the main tube furnace.

The test atmosphere consisted of 100% steam at 850°C for 12 hours and 915 °C for 1 hour, achieving a calculated oxygen partial pressure of 10^{-6} atm. Heating and cooling ramp rates were $10 \text{ }^{\circ}\text{C}\cdot\text{min}^{-1}$. A graphical description of the test is shown in Figure 2.7.

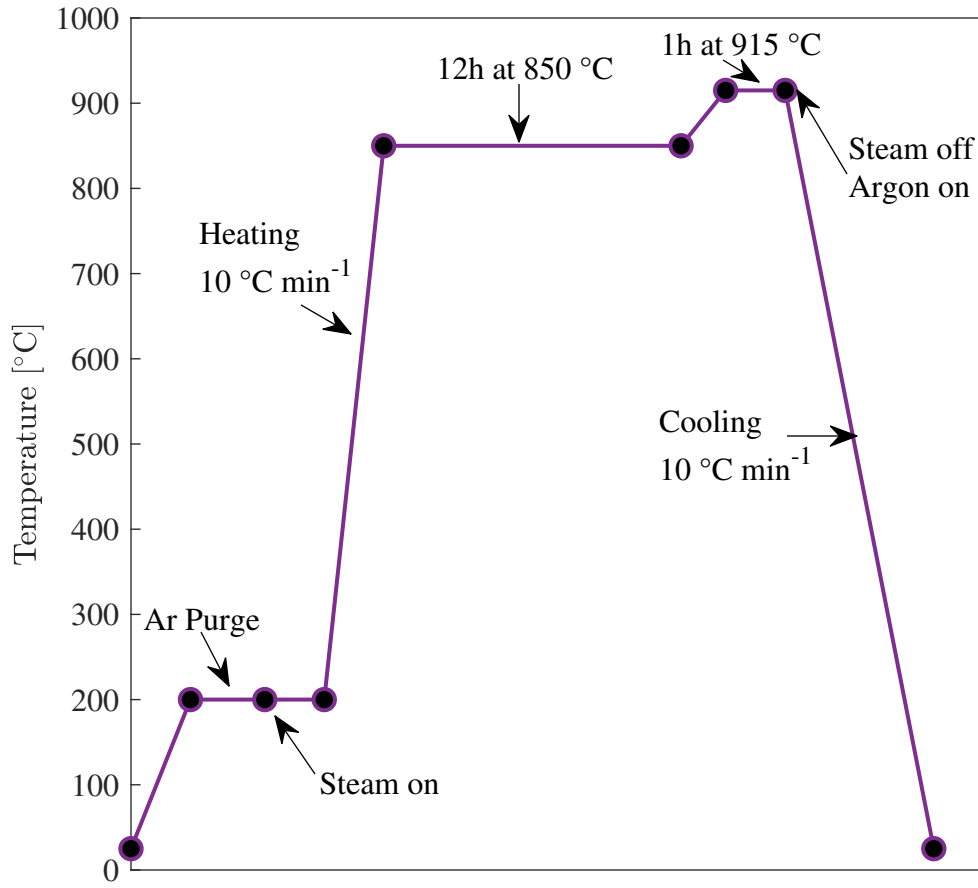


Figure 2.7: Experimental conditions for the Preoxidation Step

2.2.4 Characterization

Samples were characterized in the as-cast and preoxidized states after exposure to oxidizing conditions. Samples for surface analysis, optical microscopy, and microhardness tests were mounted into a black conductive thermosetting resin (Conductotherm 3000) and prepared using common metallographic techniques.

Change of mass

Mass measurements after preoxidation were made with a 0.01 mg resolution analytical balance. This allowed for determination of oxide growth based on change of mass data.

Microstructure analysis

X-ray diffraction (XRD) was performed using a Bruker D8 Discover with Cu K α radiation, scanning the samples from two-theta of 20° to 100° at 0.1°.min⁻¹ and with a sample rotation of 0.5 rpm. XRD analysis was used to identify oxides, carbides and any other phases present at each stage for each material. Sample surfaces for the as-cast condition were prepared by grinding to 1200-grit SiC while subsequent conditions were scanned without any additional surface preparation.

Optical images were taken to identify features in the matrix using a Zeiss Axiovert A1. High magnification images of any developed oxide, and intermetallics, were taken using scanning electron microscopy (SEM) to determine the continuity of the oxide layer. For the elemental composition, energy dispersive x-ray spectrometry (EDS) mapping technique was performed. SEM and EDS were conducted with a JSM-6460 LV operating at an accelerating voltage of 15 keV, a working distance of ~13 mm, and a spotsize of 50.

2.3 Results and discussion

Several samples of each alumina-forming alloy and chromia-forming alloy were exposed to preoxidation conditions with the intent of forming an oxide layer at the surface, same as the process encountered when new tubes are placed into service. Data collected and summarized in this section includes the change in mass and microstructural analysis resulted from exposure to preoxidizing conditions. A main comparison of one AFA alloy against one HP alloy is done in order to illustrate the oxidation performance of the alloys.

2.3.1 Change of mass

Alloys were exposed to a 100% steam atmosphere at 850 °C for 12 hours followed by exposure to 915 °C for 1 hour. Mass was tracked before and after preoxidation for each sample. Average change of mass per unit area is reported in Figure 2.8. The reported values correspond

to an average of 15 samples per material. The comparison of the data shows that the AFA alloys had smaller weight gain during preoxidation compared to the HP alloy. As mentioned in Table 1.1, alumina scales grow at a rate that is 1 to 2 orders of magnitude lower than that of chromia. Then, a smaller weight gain for the AFA alloys indicates that the oxide scale for the AFA alloys, aluminum oxide, is thinner than the oxide scale for HP alloy, chromium oxide.

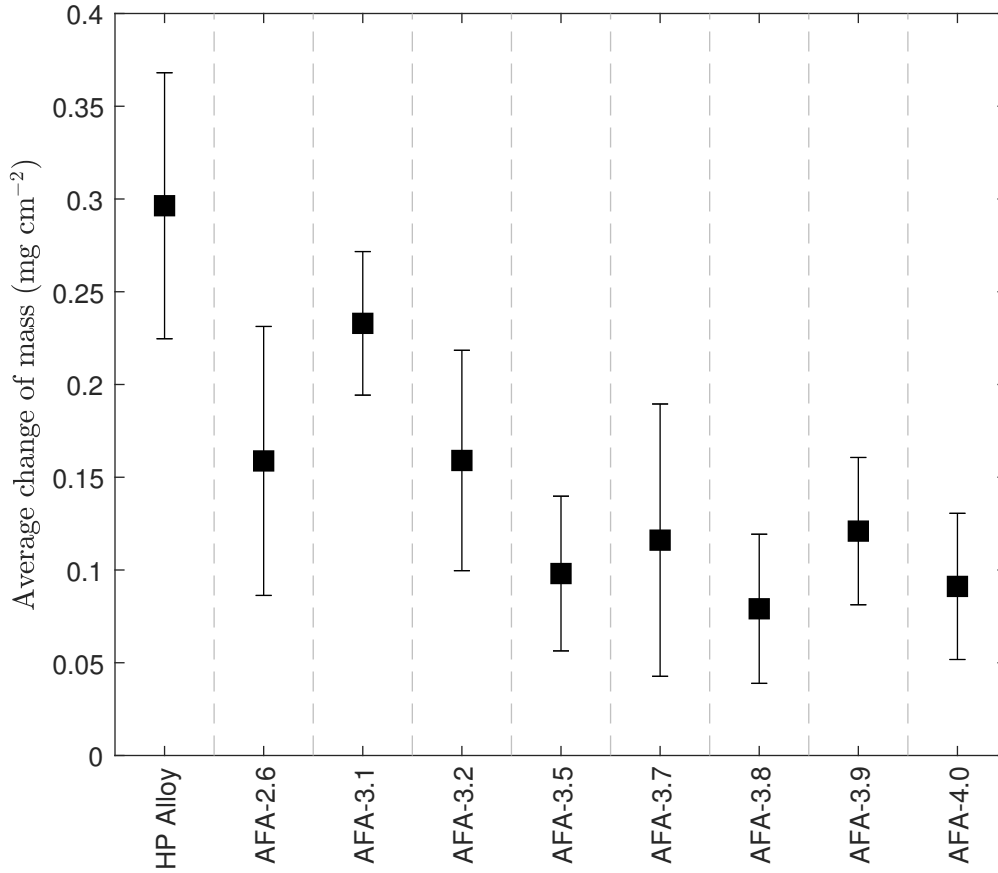


Figure 2.8: Specific change of mass after preoxidation. Average of 15 samples per material.

2.3.2 Microstructural analysis of as-cast alloys

The as-cast optical microstructures for each one AfA and the HP alloy are shown in Figure 2.9. Both alloys are composed of an austenitic dendritic matrix with interdendritic Cr

carbides and Nb carbides.

SEM images of the as-cast samples shown in Figure 2.10 confirm the presence of Cr and Nb carbides in the boundaries. Cr carbides, usually type $M_{23}C_6$, correspond to the dark gray areas while Nb carbides, type NbC, correspond to the bright phase areas (see Figure 2.11 and Figure 2.12 for EDS results). Similar investigations on austenitic stainless steel alloys show the presence of these carbides along the grain boundaries in the as-cast microstructures, and are related to the high-temperature creep strength achieved by these alloys.^[33]

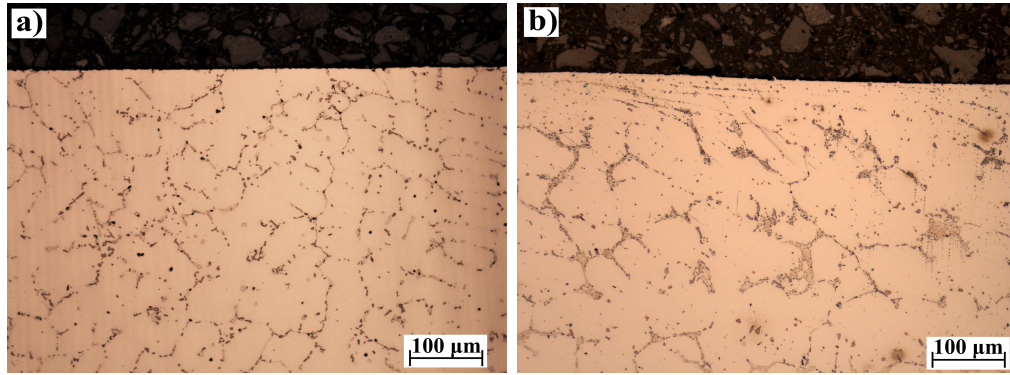


Figure 2.9: Optical microscopy of as-cast samples of surface microstructure of a) AFA-3.8 alloy and b) HP alloy.

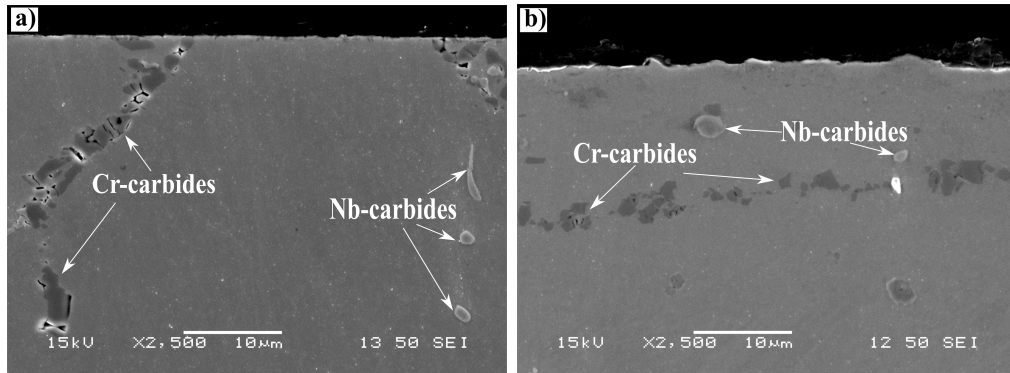


Figure 2.10: SEM cross-section of as-cast microstructure of a) AFA-3.8 alloy and b) HP alloy.

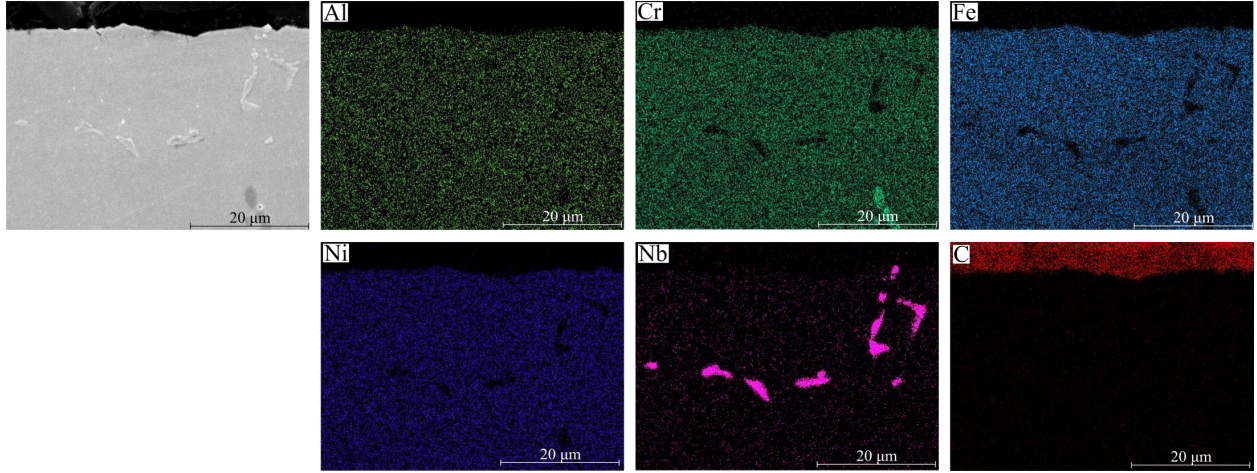


Figure 2.11: EDS mapping cross-section of as-cast microstructure of AFA-3.8 alloy.

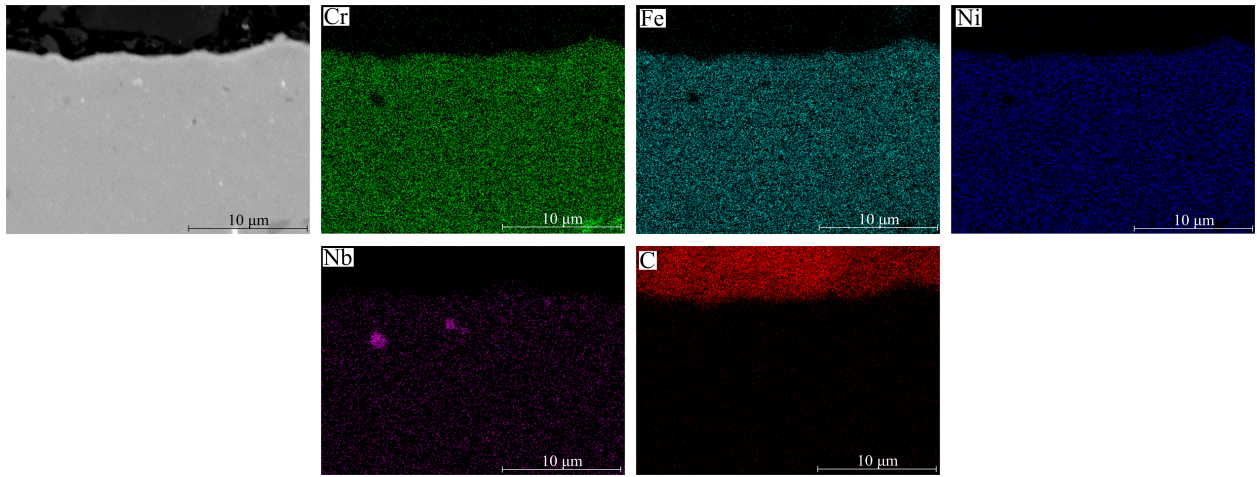


Figure 2.12: EDS mapping cross-section of as-cast microstructure of HP alloy.

2.3.3 Microstructural analysis of oxidized alloys

Digital images of some of the alloys after preoxidation are shown in Figure 2.13. Alloys showed a change in color after exposure to steam environment, which is related to the oxide formation at the surface.

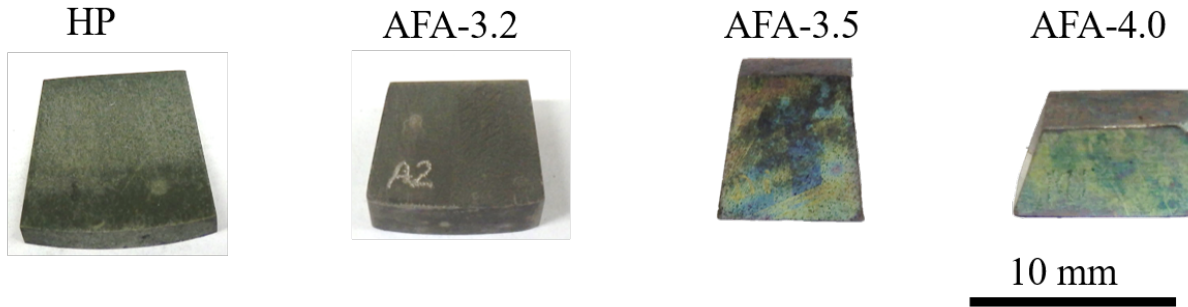


Figure 2.13: Digital images of some alloys after preoxidation

SEM cross-sectional images after preoxidation are shown in Figure 2.14. The developed oxide layer consisted of a very thin layer of aluminum oxide in the case of the AFA alloys (less than 1 micron) and a thin, discontinuous chromium oxide layer in the case of the HP alloys (~ 2 microns). Oxide layer thickness is consistent with the change in mass shown in Figure 2.8, indicating that a higher gain in mass yields to a thicker oxide scale.

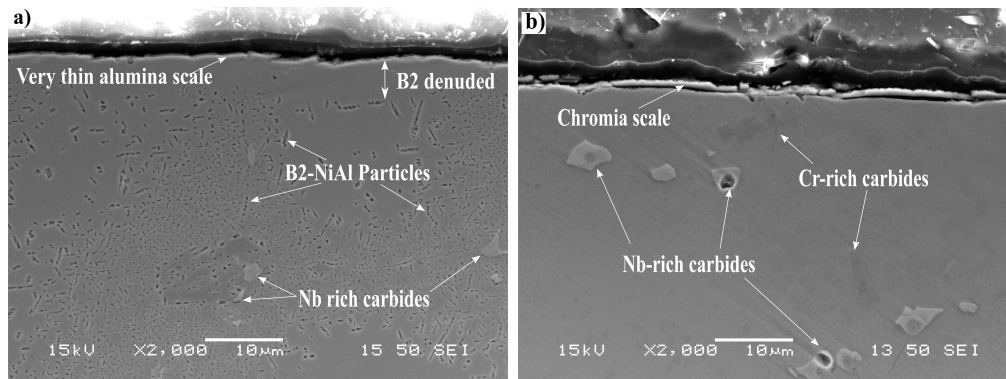


Figure 2.14: SEM cross-section of samples after preoxidation for a) AFA-3.8 alloy and b) HP alloy.

In Figure 2.14a, the AFA alloy shows the precipitation of B2-NiAl particles, and presence of the primary coarse NbC observed in the as-cast microstructure as shown in Figure 2.10. These results are consistent with other investigations where oxidation of AFA alloy, at temperatures between 600°C and 900°C, resulted in the formation of micron size B2-NiAl base phase precipitates due to the low solubility of Al and Nb in the austenite matrix.^[20,34] Additionally, it has been shown that these B2-NiAl particles support the formation of the alumina layer in AFAs by acting as an Al reservoir and is consistent with the Al depletion

in the form of the B2-denuded zone.^[35,36] In Figure 2.14b, the HP alloy shows the chromium oxide layer at the surface along with Nb-rich and Cr-rich carbides in the matrix. No major microstructural changes in the base metal compared to the as-cast state were observed under SEM after being preoxidized. Additionally, EDS analysis indicated that only Al and O were present in the oxide scale in the case of the AFA alloy, and only Cr and O in the case of the HP alloy as shown in Figure 2.15 and Figure 2.16).

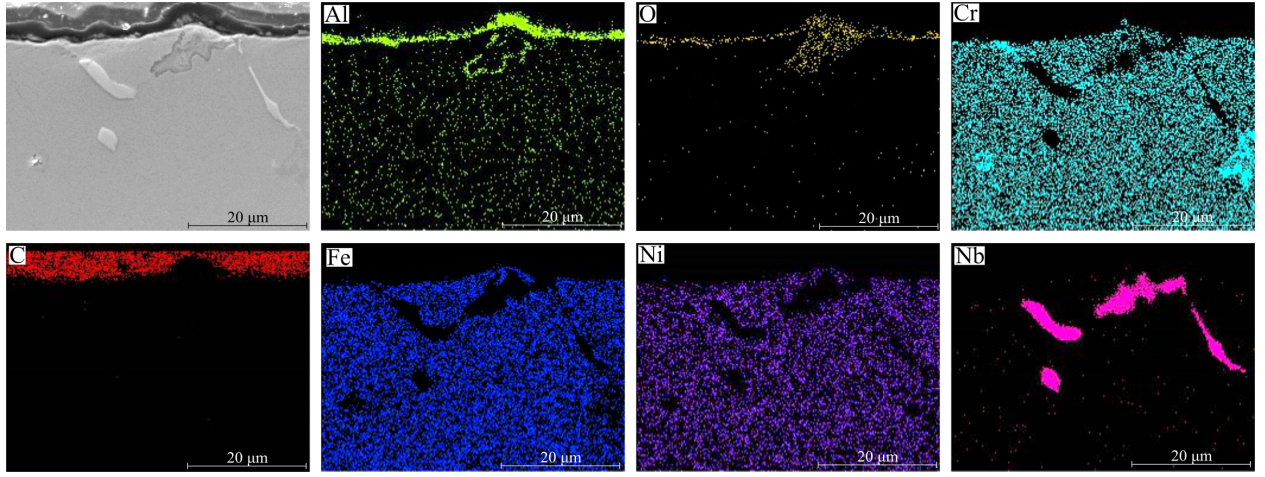


Figure 2.15: EDS mapping cross-section after preoxidation for AFA-3.8 alloy.

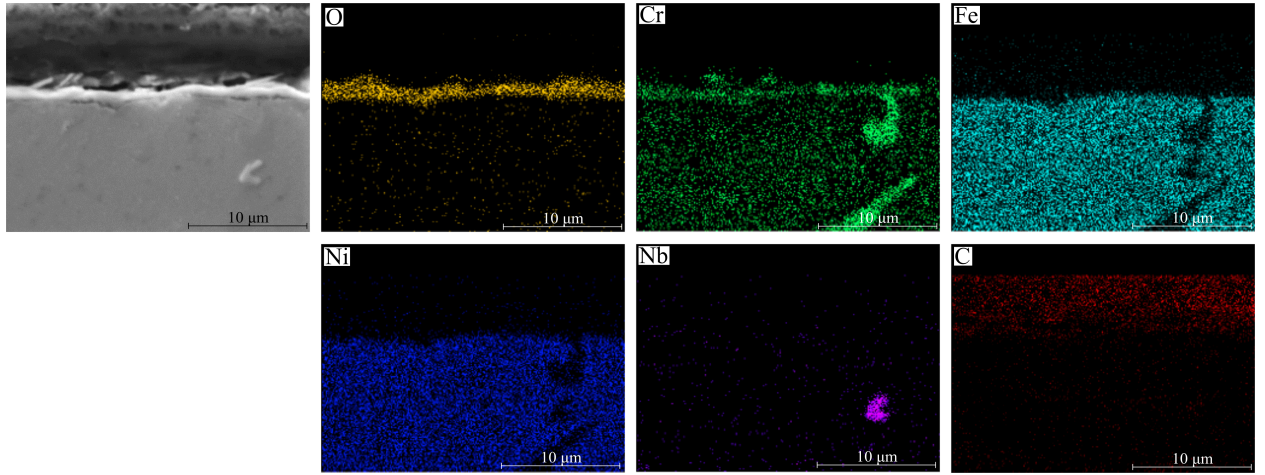


Figure 2.16: EDS mapping cross-section after preoxidation for HP alloy.

XRD analysis for both AFA and HP surface alloys are shown in Figure 2.17. After the preoxidation treatment, XRD analysis for the AFA alloy does not show major peaks for

alumina ($\alpha\text{-Al}_2\text{O}_3$) because the oxide scale is very thin (less than 1 micron). Additionally, the B2-NiAl phase observed in cross-sectional SEM was not detected by XRD. Investigations on the microstructural evolution of AFA alloy have shown that, after 3000 hours of aging, the peaks of B2-NiAl phase in the XRD pattern start to become prominent^[37]. Therefore, after 12 hours of oxidation, and 240 hours of combined coking-decoking cycles, it is expected to not detect the B2-NiAl phase by XRD.

XRD analysis for the HP alloy after the preoxidation treatment shows correspondent peaks that indicate presence of chromium oxide (Cr_2O_3) on the surface. Overall, no major changes in microstructure for both AFA and HP alloys after the preoxidation are seen from XRD when comparing to the as-cast microstructure.

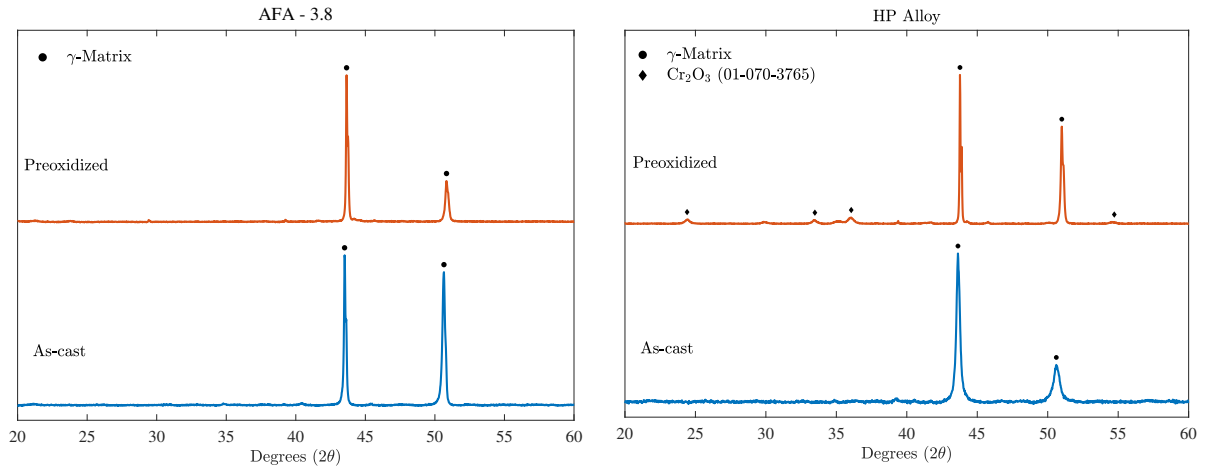


Figure 2.17: XRD analysis for the AFA-3.8 and the HP alloy after preoxidation. Each pattern has been normalized between 0 and 1. JCPDS number is shown next to its compound name. γ -Matrix has been associated to the as-cast microstructure.

2.4 Summary

Samples of alumina-forming alloys and chromia-forming alloys were preoxidized in a 100% steam environment at 850°C for 12 h, followed by 1 h at 915 °C. The intent of the preoxidation step was to develop an oxide layer at the surface, same as encountered in the petrochemical thermal cracking operations when new tube furnaces are placed into service.

From the change of mass data, the majority of the AFA alloys had a smaller weight gain during preoxidation compared to the HP alloy. This correlates to the microstructural analysis where the developed oxide scale of the AFA alloy was thinner than the oxide scale of the HP alloy.

Additionally, no major microstructural changes were observed from optical microscopy, SEM, and XRD analysis. SEM showed the presence of the B2-NiAl phases in the AFA alloy that promotes formation of the oxide scale. XRD detected chromium oxide in the HP alloy, but the very thin oxide scale developed in the AFA alloys was not detectable by the XRD. However, EDS analysis showed the presence of the oxide scale in both alloys.

Chapter 3

Coking kinetics

The aim of this chapter is to present the rate of coke formation and the effect of long-term exposure to an ethane-hydrogen atmosphere of alumina-forming alloys against a traditional chromia-forming alloy used in the ethylene thermal cracking process. The alloys were exposed to the coking atmosphere at 900, 950, and 1000 °C for 100 hours at each temperature to determine the kinetic parameters. Additionally, the alloys were exposed to the same coking atmosphere at 950 °C for 1000 hours to study the long-term material performance. Data collected includes change in mass data, and microstructural analysis resulted from exposure to coking. Furthermore, an analysis on the elemental distribution in the alloy with respect to the surface, and its effect on the alloy's coking resistance is explained in this paper.

3.1 Introduction

During thermal cracking of hydrocarbons, the internal surface of the reactors exposed to hydrocarbons results in a coke layer deposited on the inner surface of the cracking coils, resulting in a reduction in the energy efficiency of the plant, in a reduction of the main product's yield and eventually, it leads to an inevitable shutdown of the furnace for coke removal, or decoking process.

During cracking of ethane, a continuous layer of coke is formed on the inner walls of

the tubes reducing the heat transfer across the reactor wall, increasing the reactor tube metal temperature to 1100 - 1200 °C, and increasing the pressure to more than 1.5 atm.^[38] This leads to an inevitable shutdown of the furnace tubes for removing of carbon build-up, or decoking, which increases the operational costs and reduces the energy efficiency of the plant. In addition, the furnace tube material deteriorates with the successive coking-decoking cycles due to corrosion and carburization causing a need for replacement of the reactor coils every 4 to 10 years.^[5] The run length of the reactor usually varies from 10 to 80 days, depending upon the feed stock, type of reactor and severity of operation.^[39] For a ethane cracker normal run lengths are of the order of 20-60 days, depending upon the operating conditions^[40]. Therefore, an understanding of the coke formation is desirable to reduce carbon build-up such that the run length of the furnace tubes increases, which leads to a higher productivity and less operating costs.

Different studies on the rate of coking for thermal cracking operations using different types of feedstock, such as methane, ethane, propane, and other hydrocarbons have been conducted.^[41–44] However, studies that analyze the effect of the furnace tube material on the rate of coking are limited. It is known that the amount of coke produced and deposited on the walls of cracker coils depends mainly on the type of feed used, the operating temperature, and the coil material.^[3,10] Furthermore, there are four known mechanisms proposed by various researchers in the field: pyrolytic coke formation, catalytic coke formation, condensation of high boiling components, and deposition of mechanically transferred coke in downstream equipment^[13]. In ethylene thermal cracking with an ethane feed, coke formation seems to be of mainly pyrolytic and catalytic nature.^[45] Catalytic coke formation, as opposed to pyrolytic coke formation, is associated with the availability of catalytic sites on the metal surface. For instance, the catalytic coking rate is dependent on the material of the reactor tube, especially when the surface is new or in the decoked state, because of the availability of catalytic sites that accelerate the coke formation. As a result, it has been found that the catalytic coke deposited on the metal surface act as promoter to the subsequent pyrolytic coke particles

formed in the gas phase.^[46]

3.2 Theory

In ethane thermal cracking, coke deposits are mainly formed due to catalytic and pyrolytic mechanisms. When the surface of the cracking coil material is new or in the decoked state, catalytic metal particles on the tube surface are available and act as catalytic sites for carbon to deposit^[47]. With time, the deposited catalytic coke promotes subsequent carbon deposition. This mechanism, known as pyrolytic, becomes predominant over long periods of time. Additionally, under typical conditions of a thermal cracking reactor, the contribution of the catalytic mechanism is minimal compared to the pyrolytic mechanism because of the long exposure times that thermal crackers are subjected^[16,48].

Studies on 20Cr-25Ni-Nb-stabilized austenitic steels containing either zero or 0.56 wt.% Si using CO₂/CO/C₂H₄ gas mixture at 550 °C ($102 < a_c < 107$), have shown that carbon filaments are not readily nucleated on chromia layers, in particular for the Si-free steel. By using Si-free and Si-bearing versions of the alloy, neither chromia nor magnetite catalyzed carbon deposition under those test conditions. However, carbon deposits formed in regions covered by iron-rich oxides provided there was gas access to catalytic sites within the alloy substrate. Authors postulated that these were regions of metallic nickel formed (see Figure 3.1) as a result of the selective oxidation of chromium and iron by the depositing gas.^[31]

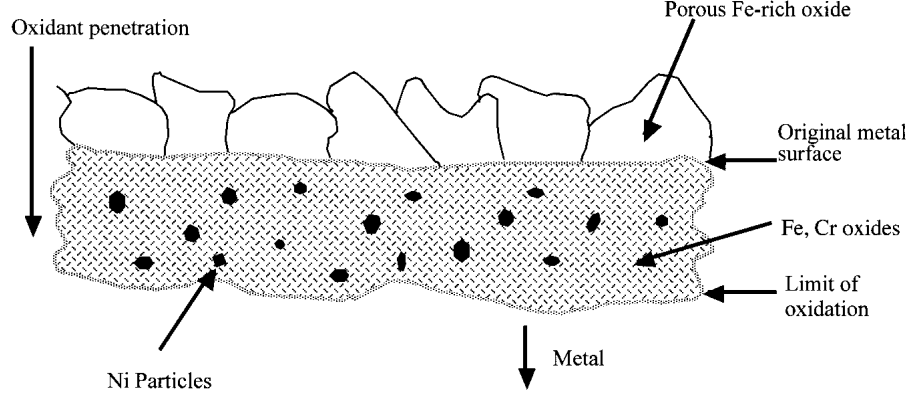


Figure 3.1: Schematic depth profile illustrating a suggested mode of formation of nanoparticles of Ni that can act as potential catalytic agents for producing carbon filaments.^[31]

Because the coke deposition can be of catalytic and pyrolytic nature, the kinetics rate equation involves the surface reactions and subsequent formation of the carbon filaments. In ethane thermal cracking, based on Froment’s molecular scheme, both ethane and ethylene can be used as coke precursors as described by the following chemical reactions^[11,40,49–51]:



Previous studies have focused on the mechanism of carbon deposition based on different atmospheres often seen in ethylene and propylene thermal cracking environments. While there are still discussions about the chemical reactions that describe the coking phenomenon, studies that use ethane feedstock in coking experiments have found that ethane gives an adequate approximation when used as the main coke precursor (see equation 3.1)^[52,53]. In this research, samples were exposed to a 30:1 hydrogen:ethane ratio coking atmosphere, and ethane was assumed as the main coke precursor in the coking rate.

3.2.1 Determination of kinetics coking rate

Coke deposits can be quantified based on the change of mass recorded during each test. The accumulation of carbon deposits, or coking rate, can be described by:

$$r_C = \frac{dm}{S dt} \quad (3.3)$$

Where r_C is the coking rate in $[\text{mg}\cdot\text{cm}^{-2}\cdot\text{h}^{-1}]$, S is the surface are of the alloy, m is the change of mass after exposure, and t is the exposure time.

The amount of coke deposited during coking experiments is determined by the effect of both catalytic and pyrolytic coking rates. The experimental kinetics curves (specific change of mass vs. time) usually show two stages: initial and asymptotic coking rates. While the initial rate is associated with the catalytic coking rate, the asymptotic, or pyrolytic coking rate, is the one that, in practice, determines the amount of coke deposited in industrial cracking coils^[54,55]. In addition, the amount of coke deposited is affected by the temperature at which the cracking reaction occurs. To establish the coking rate kinetics based on experimental observations, equation 3.3 can also be expressed as:

$$\frac{\Delta m}{S} = kt^n \quad (3.4)$$

Where $\frac{\Delta m}{S}$ is the weight gain per unit area at time t , k is the temperature dependent rate constant, and n is the time exponent of the rate law. The kinetic parameters (k and n) are obtained from the rate equation 3.4 using the collected data of mass for each test. Furthermore, the rate constant k follows an Arrhenius relation given by:

$$k = A \exp\left(\frac{-E_a}{RT}\right) \quad (3.5)$$

Where A is the pre-exponential factor, R is the ideal gas constant ($8.314 \text{ J}\cdot\text{mol}^{-1}\cdot\text{K}^{-1}$), T is the absolute temperature [K], and E_a is the activation energy. The importance of the calculation of the activation energy is that this parameter can be used as the metric for coke formation and relative indication of performance, and is usually associated with

the gas-phase formation of pyrolytic carbon being the rate-controlling step in the coking deposition^[56]. Table 3.1 shows reported activation energies of similar alloys, mostly chromia-forming alloys, in other thermal cracking environments. These values are used as a reference for comparison of the activation energies obtained in this dissertation.

Table 3.1: Activation Energy reported by other authors in similar cracking environments.

Reference	Coking Environment	Temperature range [°C]	Alloys studied	Activation energy [kJ·mol ⁻¹]
[52]	Ethane - Nitrogen	825 -875	Cr, Fe, Stainless Steel	63, 73, 91 respectively
[57]	Hydrogen - Propylene	900 - 1000	HP-type	95 – 220
[58]	Ethane - Naphta	825 – 850	Incoloy 800HT, 15Mo3	86 – 150
[59]	CH ₄ /H ₂ /CO	870 – 980	Incoloy 800HT	130 – 189

In this document, coking kinetic parameters were evaluated at 900, 950, and 1000 °C, in a hydrogen-ethane atmosphere. Calculations presented in the results section illustrate the effect of temperature and time on the coking rate, rather than the effect of the gas composition. Related works have demonstrated that the effect of temperature on the coking rate is stronger than that of the gas composition^[55].

3.2.2 Carburization attack

The purpose of the preoxidation step is to develop an oxide layer at the surface of the alloy, so it can prevent carbon diffusion into the metal due to the coke deposited on the surface. However, when the oxide layer is partially reduced or fails, carbon diffuses into the matrix allowing the formation of a carburized layer in the alloy^[44,60]. The carburized layer is associated with the formation of M₂₃C₆ and M₇C₃ carbides^[25]. The presence of these carbides, more specifically the M₇C₃ carbides, is undesirable because it causes surface hardening negatively affecting the mechanical properties of the material^[55]. These types of

carbides tend to be chromium rich, indicating that in the case of chromia-forming alloys, Cr is tied up with the carbides, so it is less available in the matrix to form the protective chromium oxide scale^[61]. In contrast to the chromia-forming alloys, the presence of these carbides likely does not affect the availability of aluminium for the formation of the main oxidation product, alumina, in the alumina-forming alloy.

Moreover, the coking kinetics rate can be correlated with the carburization attack in the alloy. In general, a kinetics rate that follows a parabolic function ($n=0.5$) indicates a diffusion controlled mechanism^[56,62–64]. Then, it is possible to assume that the diffusion of carbon derived from the coke layer at the surface controls the formation of the carburized layer in the alloy^[65–67]. In this paper, in order to measure the carbon diffusion in the alloys, the apparent carbon diffusion coefficient (D_{app}) was estimated using the carbon profiles obtained by EDS analysis. Depending on the shape of the carbon profiles, as shown in Figure 3.2, two models were analysed: Fick's second law, and Boltzmann-Matano analysis. One of the main differences between these models is related to whether the diffusion coefficient is assumed to be constant or not.

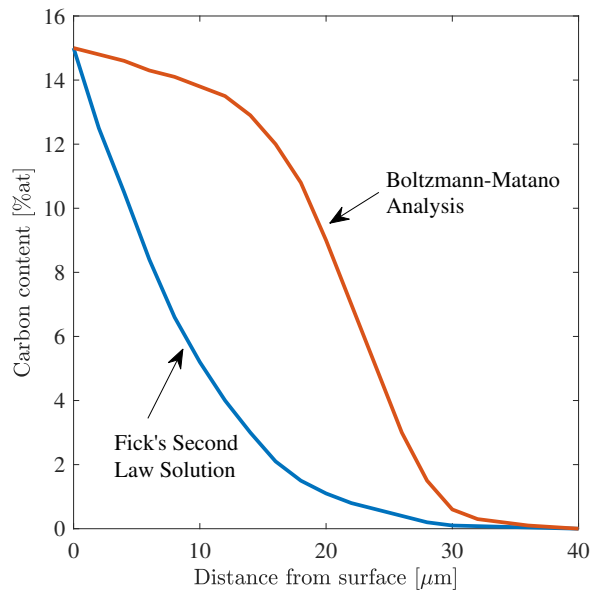


Figure 3.2: Example of carbon concentration profile based on a standard Fick's second law solution, and a Boltzmann-Matano analysis.

If the diffusion coefficient is assumed to be constant, the solution of Fick's second law combined with the least square method, can be used to estimate the carbon diffusion coefficient. The evolution of the carbon concentration as a function of depth, x , and time, t , is given by the following expression:

$$\frac{C_{x,t} - C_0}{C_S - C_0} = \operatorname{erfc} \left(\frac{x}{2\sqrt{D_{app}t}} \right) \quad (3.6)$$

With C_0 , the initial concentration, and C_S , the carbon concentration at the metallic surface. This diffusion model assumes: the carbon diffusion coefficient is constant and independent of concentration, no precipitation occurs, and carbon diffuses into a semi-infinite media with a constant surface concentration C_S .

If the diffusion coefficient is not assumed to be constant, then a Boltzmann-Matano analysis can be used to determine the carbon diffusion coefficient in the alloys^[68,69]. This model considers the diffusion of interstitial carbon from a gas phase providing a constant carbon activity into a stationary metal matrix. Also, assuming that the Matano plane (x_M) coincides with that of the alloy surface ($x_M=0$), and neglecting the effect of the carbon-induced lattice expansion on the concentration, then the diffusivity can be expressed as:

$$D_{app} = - \frac{1}{2t} \frac{dx}{dC} \bigg|_{C_x} \int_0^{C_x} x(C) dC \quad (3.7)$$

Where t is the total carburization time, C_x refers to the carbon concentration at distance x from surface, and x is the distance from surface. Equation 3.7 can be used to determine the diffusion coefficient of carbon as a function of carbon concentration, or as a function of distance from surface.

The use of Fick's solution model or Boltzmann-Matano analysis to calculate the diffusion coefficient depends on the shape of the carbon profile obtained for each alloy. An estimation of the apparent carbon diffusion coefficient in the matrix of both AFA and HP alloys was obtained, and results were compared to the reference data provided in Table 3.2. Reference

data of diffusivity were calculated based on equations provided by the references, obtained by studying the carbon diffusivity in Fe - C austenite alloys in temperatures between 800 – 1000 °C.

Table 3.2: Reported carbon diffusion coefficient at temperatures of interest. Units are given in $\text{cm}^2 \cdot \text{s}^{-1}$.

Reference	Alloy studied	Temperature [°C]		
		900	950	1000
[70]	Fe – C Austenite	6.88×10^{-8}	1.27×10^{-7}	2.24×10^{-7}
[71]	Fe – 0.31Ni-0.004C Austenite	3.30×10^{-8}	5.57×10^{-8}	9.04×10^{-8}
[72]	Fe – C Austenite	6.31×10^{-8}	1.15×10^{-7}	1.99×10^{-7}

3.3 Methodology

3.3.1 Test materials and specimen preparation

Samples of alumina-forming alloys (AFA) and chromia-forming alloys (HP), produced via centrifugal casting by a foundry engaged in the commercial production of ethylene reactor tubes, were tested^[73]. The nominal composition for each alloy is described in Table 3.3 with elements related to mechanical strengthening (Nb, Mo, C, etc.) omitted due to the proprietary nature.

Table 3.3: Nominal compositions of the alloy samples in wt.%. Other alloying additions (Nb, Mo, C, etc.) complete 100%.

Material	Al	Cr	Fe	Ni
HP	0	26	35	34
AFA - 3.2	3.2	28	27	38
AFA - 3.5	3.5	28	25	38
AFA - 4.0	4	23	33	37

Samples were prepared from as-cast pipe sections, cut with an abrasive saw, ground to 1200-grit SiC abrasive paper on all sides to ensure a similar surface roughness, cleaned with deionized water, and dried with compressed air. For reproducibility and better assessment of the data, three samples per material were prepared for each test.

3.3.2 Experimental conditions

The coking test was designed to mirror exposure to coking conditions often seen in ethylene thermal cracking but with consideration to laboratory limitations. Coking tests were carried out in a Lindberg/Blue M tube furnace, with an alumina tube (51 mm OD, 45 mm ID, 1000 mm length). The atmosphere consisted of a mixture of 30:1 hydrogen:ethane. Hydrogen (99.999% UHP) and ethane (99.9%) flow rates were 500 mL.min⁻¹, and 17 mL.min⁻¹, respectively, and were controlled using thermal mass flow controllers (Aalborg GFC-17 models). Hydrogen was used as a diluent to lower the hydrocarbon partial pressure to suppress the formation of coke on the samples. Argon was used to pre-purge the system for 1 hour at 200 mL.min⁻¹ at room temperature, and during heating and cooling portions of the test. Once the setpoint temperature was reached, the input gas was switched from argon to the hydrogen-ethane mixture. The coking process was carried out at the temperature of interest

for 100 hours. Details of the flow rates, times, and temperatures can be found in Table 3.4. Additionally, heating and cooling ramp rates were $10\text{ }^{\circ}\text{C}\cdot\text{min}^{-1}$, and argon gas (99.999%; Ultra-High Purity grade) was flowed during those ramp periods.

Table 3.4: Test conditions.

Parameter	Set value
Temperature [$^{\circ}\text{C}$]	900, 950, 1000
Time [h]	100
99.99% C_2H_6 [$\text{mL}\cdot\text{min}^{-1}$]	17
99.999 H_2 [mL min]	500

3.3.3 Characterization

Change of mass

Mass measurements were made with a 0.01 mg resolution analytical balance every 10 h. This allowed for the determination of the amount of mass gained after exposure to the coking atmosphere, and further calculation of the coking kinetic parameters of the alloys.

Microstructural analysis

Samples for surface analysis and optical microscopy were prepared using common metallographic techniques. X-ray diffraction (XRD) on the surface of the sample was performed using a Bruker D8 Discover with $\text{Cu K}\alpha$ radiation, scanning the samples from two-theta of 20° to 60° at $0.1^{\circ}\cdot\text{min}^{-1}$. XRD analysis was used to identify oxides, carbides, and any other phases present in the material.

Samples for optical microscopy were etched following standard procedure for determina-

tion of carburized layer using a mixture of 20 wt% of nitric acid and 4 wt% hydrofluoric acid in distilled water^[74]. Optical microscopy analysis of the cross-sectional surface was done to identify the presence of carbides and carburized layer, if any.

Scanning electron microscopy (SEM) and energy dispersive x-ray spectrometry (EDS) were conducted with a JSM-6460 LV operating at an accelerating voltage of 15 keV, and a working distance of 13 mm. High magnification images of the cross-sectional surface were taken using SEM technique to determine the continuity of the oxide layer, presence and location of carbides, or indications of internal damage. For the elemental composition, etched samples were analysed using EDS composition spectrum technique. All EDS scans were taken at a magnification of 1000x, 13 mm working distance, 35% deadtime, and a process time of 240 seconds per scan. Samples were scanned from the inner diameter (ID) surface to a depth of at least 700 μm . Each EDS area scan, with a size of 200 μm x 10 μm , tracked elemental data for the elements C, Fe, Cr, Ni, and Al, as this allowed for interpretation of the elemental distribution of the elements with respect to distance from the surface at each stage.

3.4 Results and Discussion

Three samples of each alumina-forming alloy and chromia-forming alloy were exposed to a 30:1 hydrogen-ethane coking atmosphere at 900, 950, and 1000 °C for 100 h to determine the kinetics parameters of the coking rate under this coking atmosphere. Data collected and summarized in this section include change of mass analysis, kinetics analysis, microstructural changes resulted from exposure, and an estimation of the carbon diffusion coefficient in the alloys.

3.4.1 Determination of coking kinetics rate

Mass measurements were recorded to track carbon deposition on each alloy. The specific change of mass with respect to the initial mass of the alloy after 100 hours of exposure to each coking test is shown in Figure 3.3. A trend in the change of mass can be seen for each temperature, where the higher the aluminum content, the less mass gained after exposure to coking. For example, the AFA-4.0 alloy had $\sim 95\%$, 93% and 81% less mass gained than that of the HP alloy after 100 h of exposure at 900, 950, and 1000 °C, respectively, as shown in Table 3.5. The gain in mass was the result of coking and carburization. Additionally, cooling the samples to room temperature, for weighing purposes, can induce structural deformations including the spalling of coke or oxide layers. However, no spallation was observed in the samples throughout the testing.

Table 3.5: Mass of gained respect to the HP Alloy

Alloy	900 °C	950 °C	1000 °C
AFA - 3.2	-79%	-63%	-58%
AFA - 3.5	-91%	-71%	-77%
AFA - 4.0	-95%	-93%	-81%

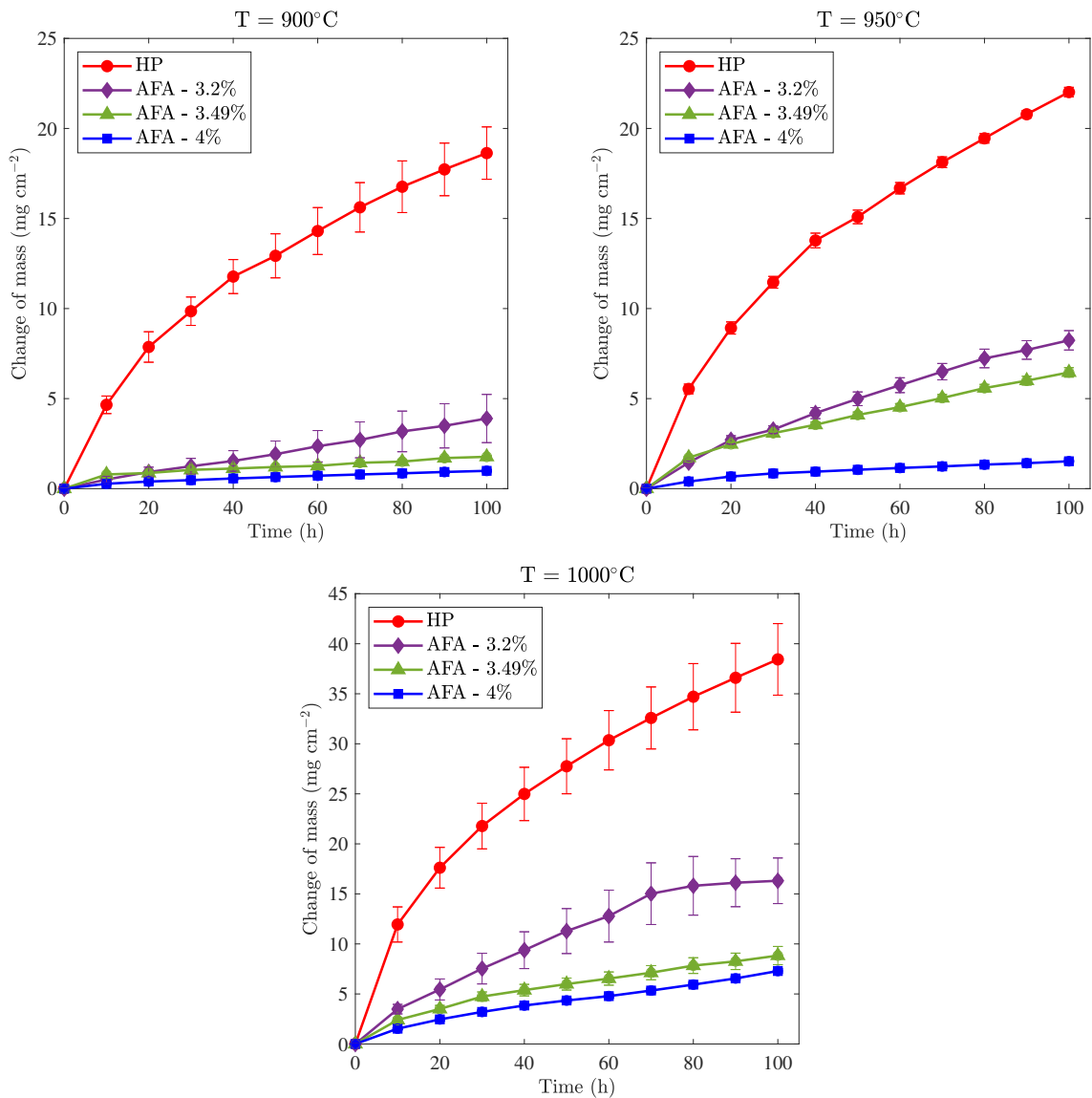


Figure 3.3: Specific change of mass after exposure to coking conditions. Reported values correspond to the average of 3 samples per material. Error bars correspond to the standard error.

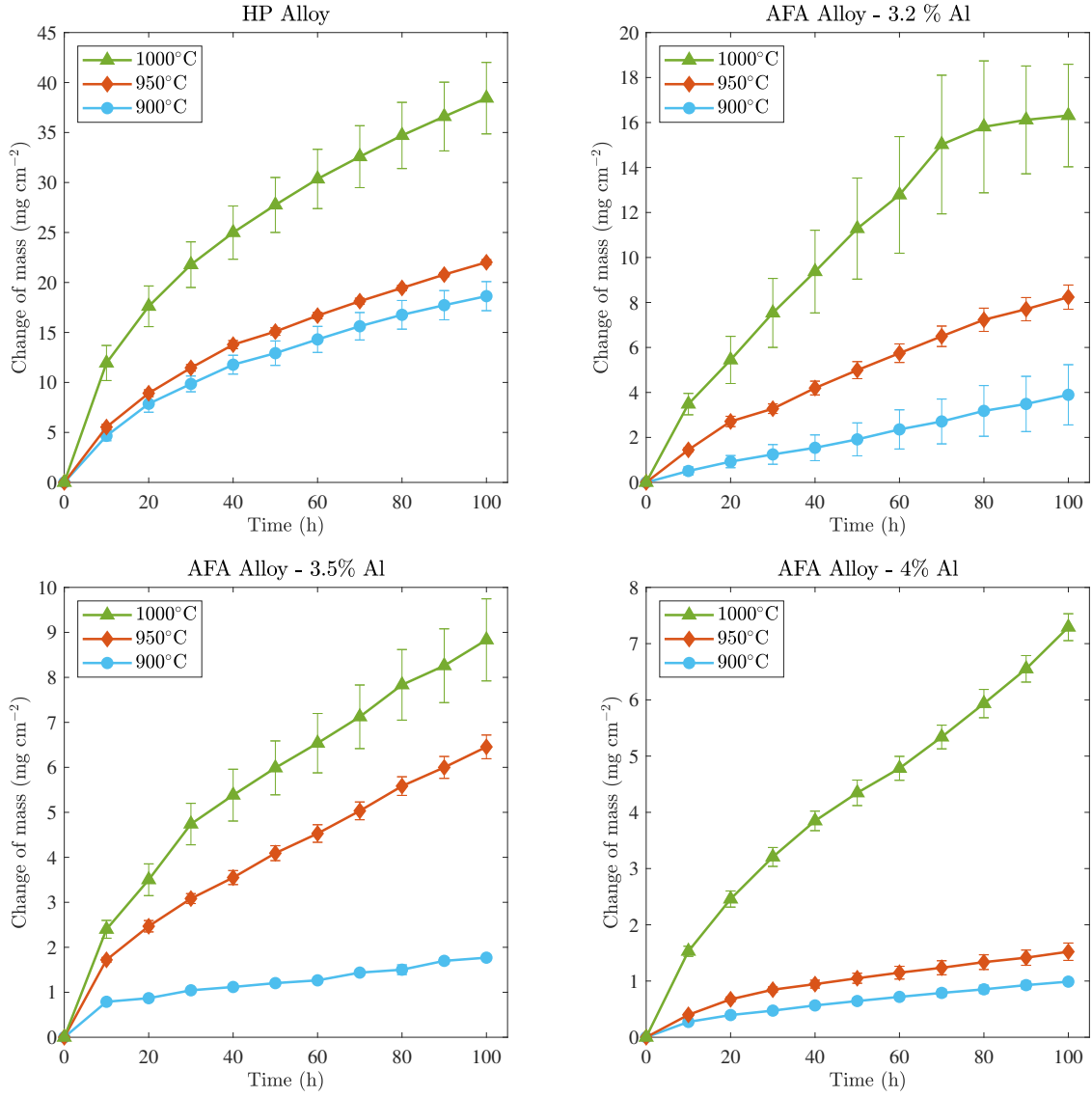


Figure 3.4: Specific change of mass per area for each AFA and HP alloys. Reported values correspond to the average of 3 samples per material. Error bars correspond to the standard error.

To determine the coking kinetic parameters (k and n), a linearization of equation 3.4 must be done, resulting in:

$$\ln\left(\frac{\Delta m}{S}\right) = n\ln(t) + \ln(k) \quad (3.8)$$

Where the time exponent of the rate law (n) corresponds to the slope, and the temperature dependent rate constant (k) can be calculated from the intercept $\ln(k)$ of the equation 3.8. Plots of $\ln(\Delta m/S)$ vs. $\ln(t)$ based on the regression data are shown in Figure 3.5. With the specific change of mass data, the kinetic parameters (k and n) were obtained from the linearization of the rate equation 3.4 (see equation 3.8). Calculated values are shown in Table 3.6.

Table 3.6: Rate constant (k) and time exponent of the rate law (n) for all tests.

Alloy	900 °C		950 °C		1000°C	
	n	k^a	n	k^a	n	k^a
HP	0.59	1.29	0.59	1.51	0.5	3.87
AFA – 3.2	0.88	0.06	0.75	0.27	0.71	0.67
AFA – 3.5	0.36	0.31	0.57	0.44	0.56	0.67
AFA – 4.0	0.56	0.07	0.55	0.12	0.66	0.33

^a The units of the rate constant will change according to the time exponent of the rate law. Units are $\text{mg}\cdot\text{cm}^{-2}\cdot\text{h}^{-n}$.

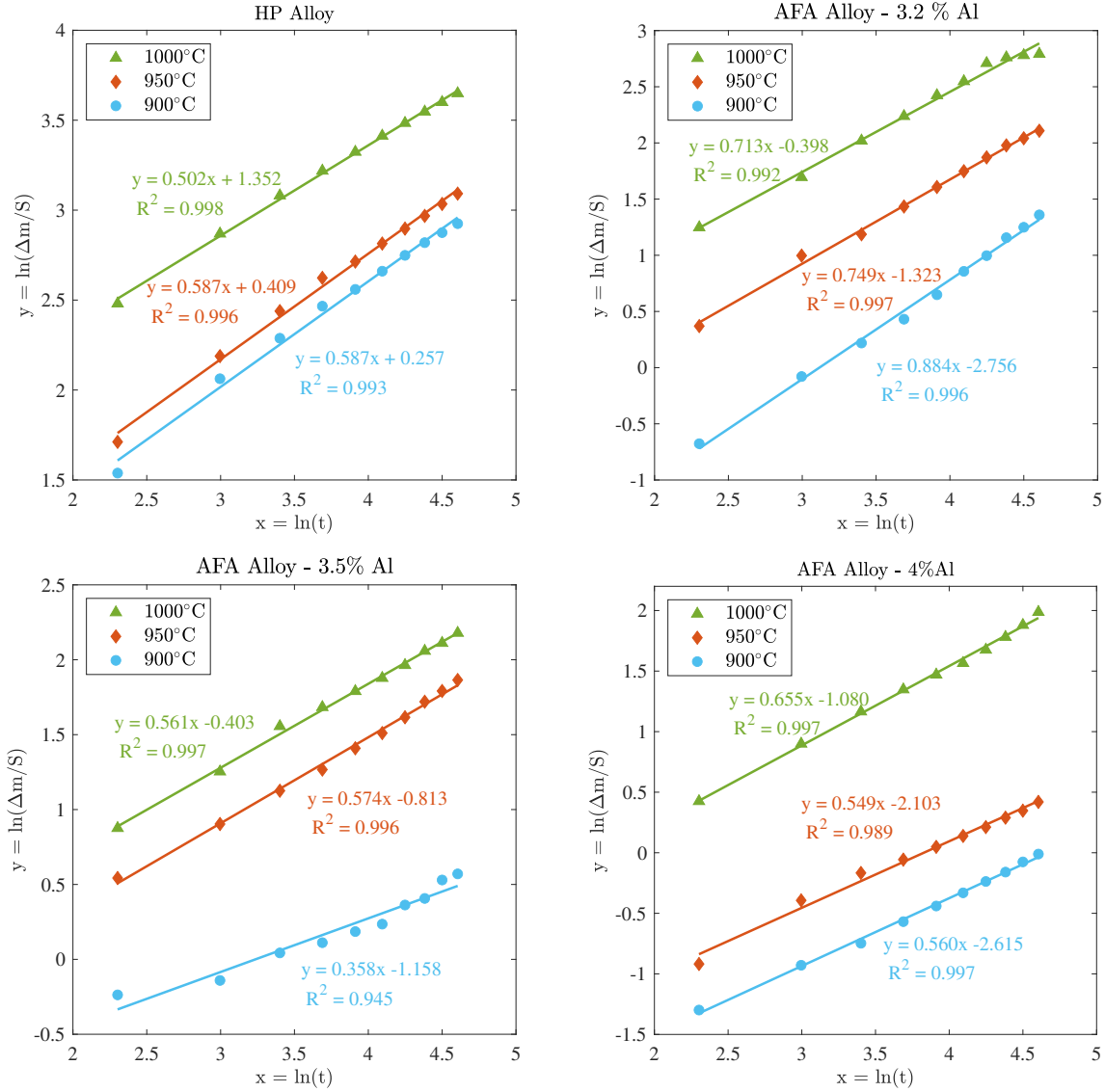


Figure 3.5: Regression data for each alloy exposed to coking conditions at three different temperatures for 100 h. Units are given in $\text{mg}\cdot\text{cm}^{-2}$ for $\Delta m/S$, and in hours for t .

The coking kinetics rate depends on the temperature, and on the type of alloy, because of the relation of temperature to oxide stability and possible carbon diffusion in the matrix. This is correlated with the time exponent of the rate law that shows a function intermediate between linear ($n=1$) and parabolic ($n=0.5$) type behaviour for the majority of the data.

Additionally, with the experimental data obtained at three different temperatures, equation 5 can be used to calculate the activation energy by obtaining the slope of the $\ln(k)$ vs. $1/T$ curve described by

$$\ln(k) = \ln(A) - \frac{E_a}{RT} \quad (3.9)$$

Furthermore, Table 3.6 shows that the units of the rate constant k are not consistent for plotting $\ln(k)$ vs. $1/T$ as described by equation 3.9. Related studies on kinetics that use methane, ethane, and propane as feedstock for coking, have found that the coking kinetics rate tends to follow linear or parabolic functions^[57,75–78]. To determine the activation energy, the time exponent (n) was assumed to be 0.5 for the calculation of the rate constant (k) parameter for each temperature. Plots of $\ln(k)$ vs. $1/T$ are shown in Figure 3.6, and the calculated coking kinetic parameters are tabulated in Table 3.7.

The activation energy values found in this investigation are in agreement with the literature (see Table 3.1). In addition, a higher activation energy can be associated with higher coking resistance. On average, the AFA alloys had an activation energy of $211 \pm 19 \text{ kJ}\cdot\text{mol}^{-1}$. Then, the activation energy for the AFA alloys being ~ 2.3 times the activation energy of the HP alloy indicates a better coking resistance for the AFA materials.

Table 3.7: Calculated Activation Energy and pre-exponential factor.

Alloy	Activation Energy	Pre-exponential factor A
	[kJ·mol ⁻¹]	[mg·cm ⁻² ·h ^{-0.5}]
HP	91.7	2.08 x 10 ⁴
AFA – 3.2	201.5	3.03 x 10 ⁸
AFA – 3.4	194.4	1.36 x 10 ⁸
AFA – 4.0	238.2	3.21 x 10 ⁹

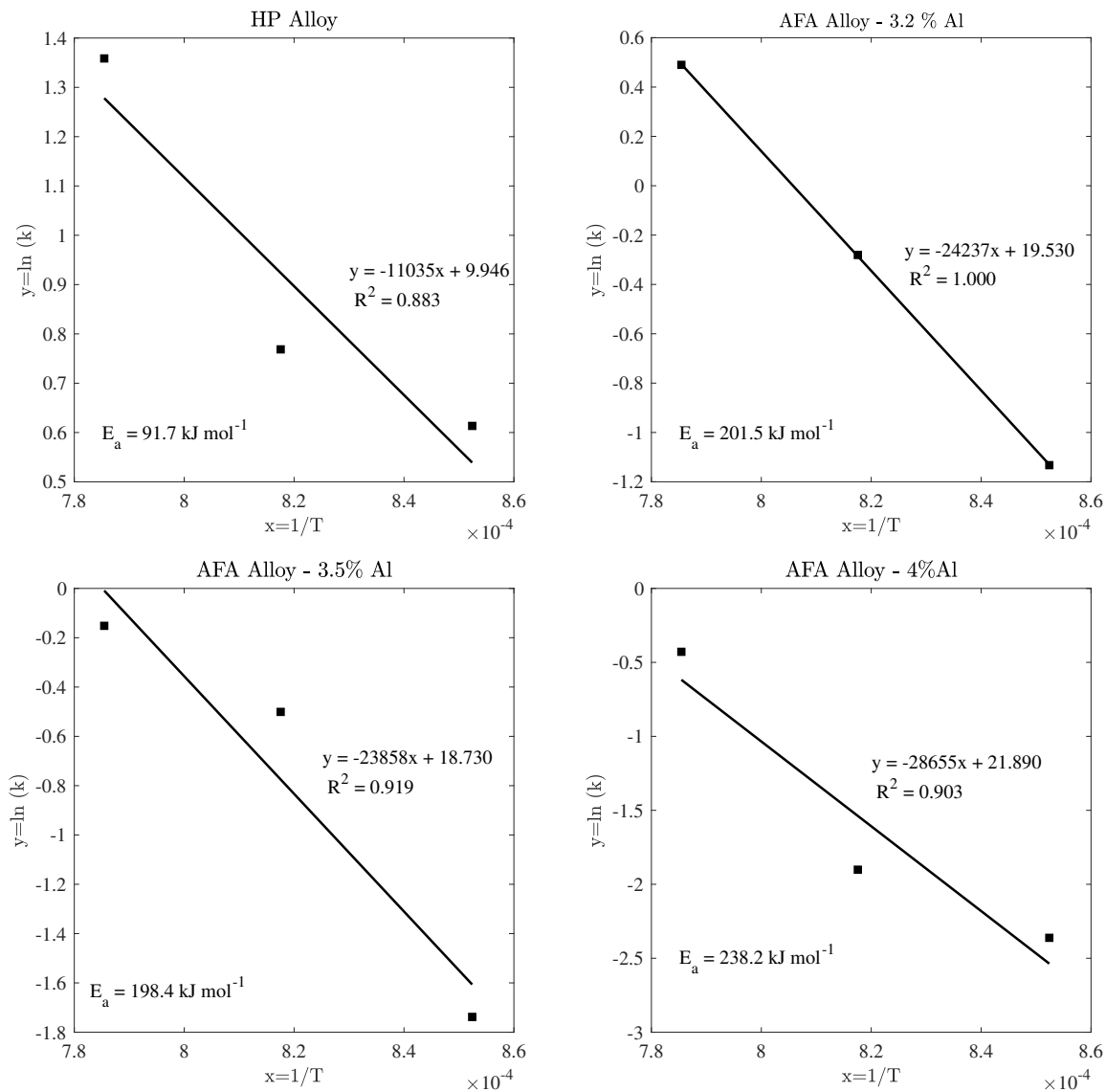


Figure 3.6: Arrhenius plots for each alloy for determination of coking kinetic parameters. The time exponent has been assumed to be 0.5 to maintain consistency of units. Units are given in $\text{mg} \cdot \text{cm}^{-2} \cdot \text{s}^{-0.5}$ for k , and in K^{-1} for T .

3.4.2 Microstructural Analysis

Digital images of samples after exposure to 950 °C for 100 h are shown in Figure 3.7. Carbon was deposited uniformly on all sides of each sample.

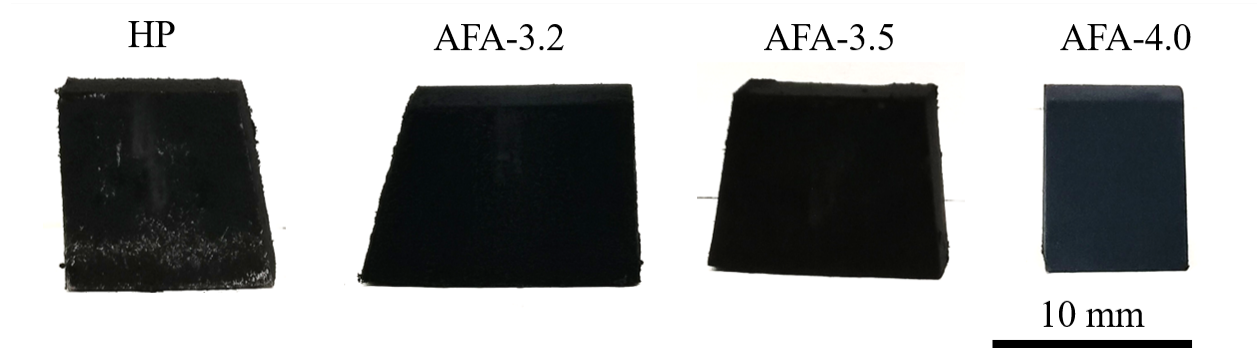


Figure 3.7: Digital images of alloys after exposure to coking conditions for 100 h.

XRD Analysis

XRD analysis for the AFA and HP alloys after exposure to 30:1 hydrogen-ethane coking atmosphere for 100 h at three different temperatures is shown in Figure 3.8. After coking, XRD patterns showed the presence of carbon (graphite) for both alloys with a higher intensity peak for the HP alloy at all three temperatures when compared to the AFA alloy results. Higher intensity correlates with higher amount of coke deposited on the surface of the HP alloy.

In the case of the AFA alloys, peaks of α -Al₂O₃ were identified at all three temperatures with the exception of AFA-3.2 at 900°C. This indicates that the oxide layer for the AFA alloys at the surface was detectable via XRD. However, a chromium oxide layer was not detected on the HP alloy by the XRD. The presence of chromium-rich carbide peaks, both M₂₃C₆ and M₇C₃ types, are present in all alloys. The HP alloy showed that the intensity of the M₇C₃ carbide peaks relative to the matrix was high for all three temperatures, indicating a major microstructural change where the chromia layer was partially reduced, allowing for carburization to occur. In contrast, for the AFA alloys, the intensity of carbide peaks relative to the matrix did not change significantly as a function of temperature.

In addition, for the HP alloy, the intensity of the carbon peak relative to the matrix becomes predominant at 1000 °C. For the AFA alloys, the carbon peak increases in intensity for the AFA-3.2 and AFA-3.5 at 1000 °C. However, the carbon peak for the AFA-4.0 alloy at 1000 °C was not predominant in the XRD pattern.

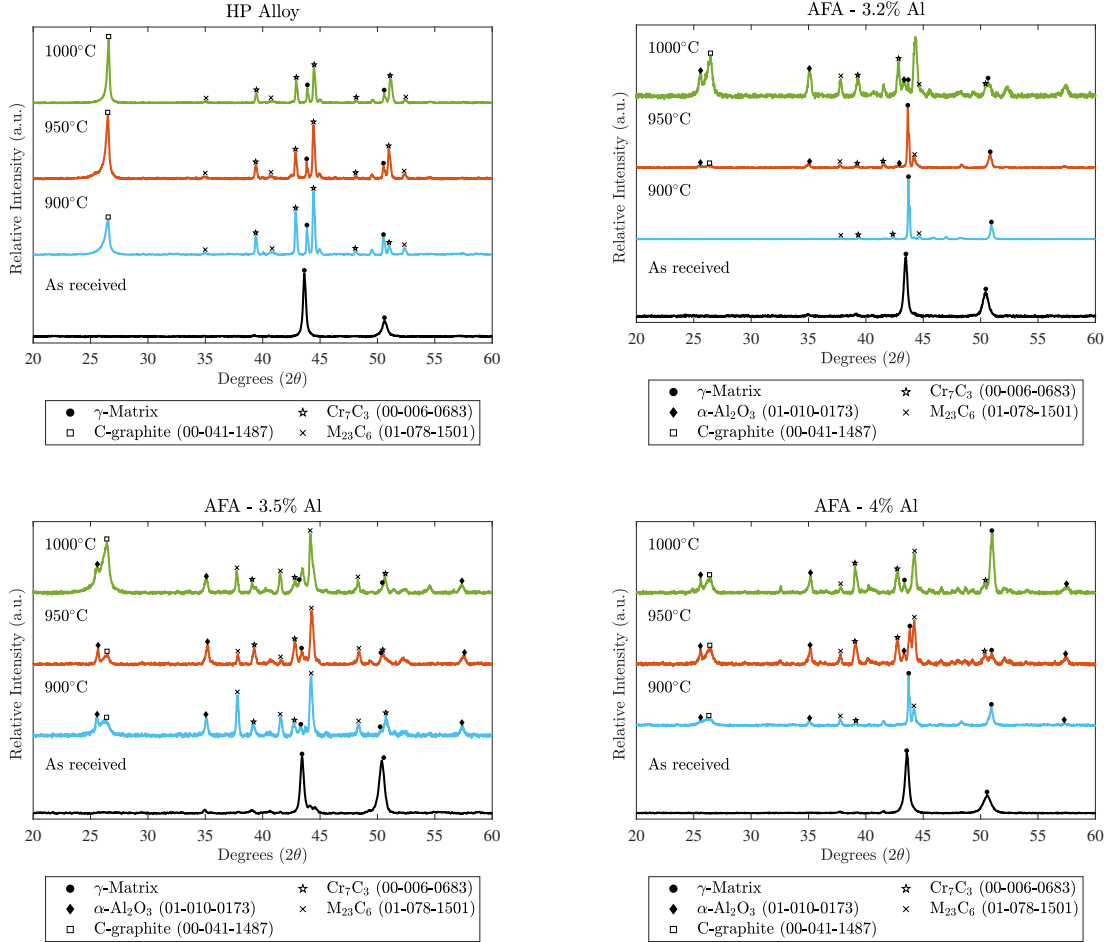


Figure 3.8: XRD analysis for the AFA and the HP alloy after exposure to 900, 950, and 1000 °C for 100 h at each temperature. Each pattern has been normalized between 0 and 1. The JCPDS number of each pattern is shown next to its compound name. The γ -matrix has been associated to the as-cast microstructure.

Optical Microscopy

Optical microscopy images of the AFA and HP alloys are shown in Figure 3.9. Overall, a carburized layer was developed in the HP alloy at all temperatures, whereas localized

carburization attack in the AFA alloy is seen after exposure at 950°C. The carburization attack was more severe for samples exposed at 1000 °C, resulting in a carburization depth of $\sim 250 \mu\text{m}$ and $830 \mu\text{m}$ for the AFAs and the HP alloy, respectively. This can be correlated with the higher gain in mass seen for the HP alloys when compared to the AFA alloys.

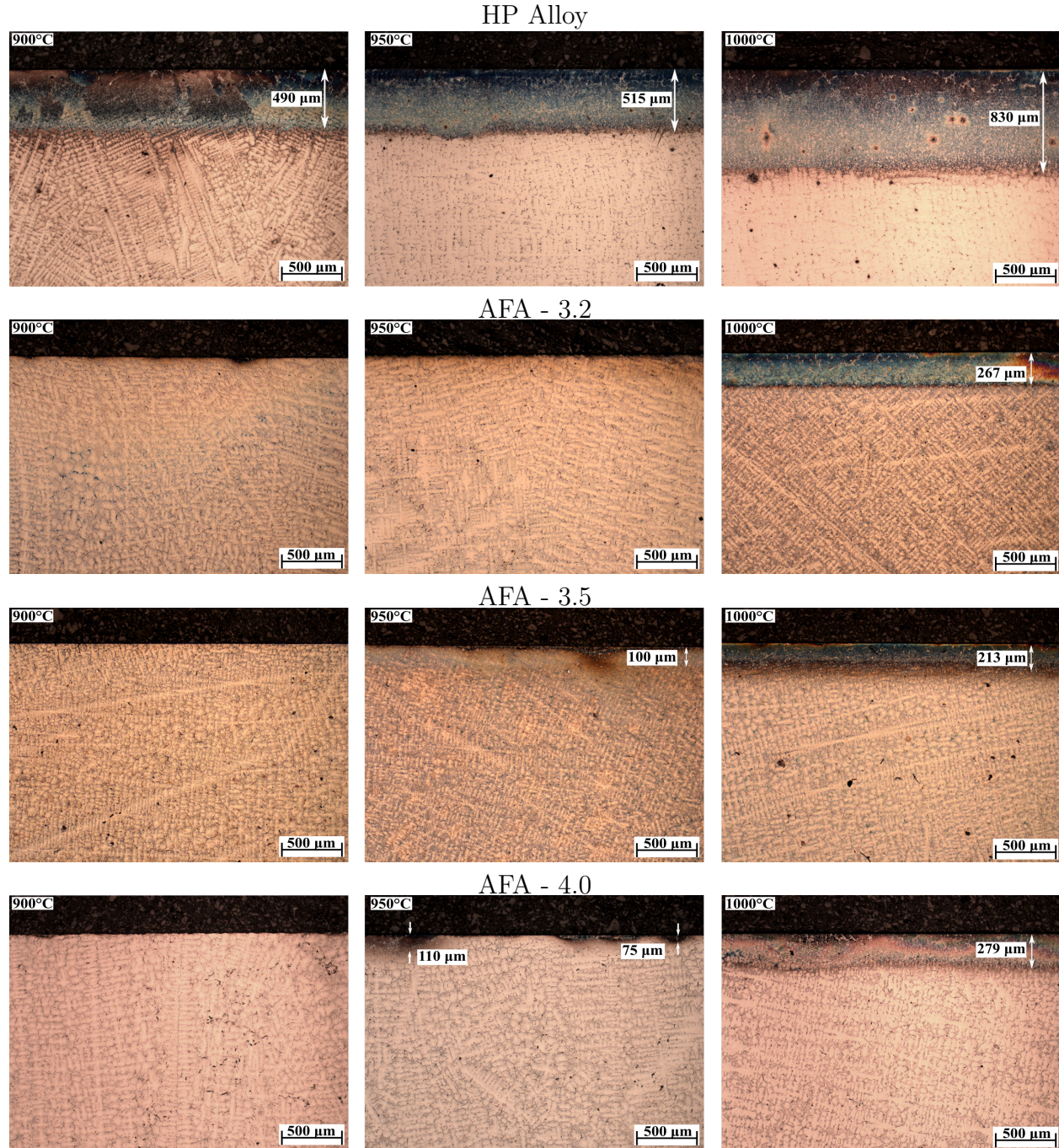


Figure 3.9: Optical microscopy images for the HP, AFA-3.2, AFA-3.5, and AFA-4.0 alloys after 100 h of exposure at 900, 950, and 1000 °C.

SEM/EDS Analysis

SEM cross-sectional images of the AFA and HP alloys are shown in Figures 3.10, 3.11, 3.12, and 3.13. The intent of the images is to show the microstructural changes in the alloys after exposure to coking conditions. The images were taken where the carburized layer was uniform in the alloys, with the intent to show the microstructural changes up to a distance of $\sim 700\ \mu\text{m}$ from surface. In general, SEM microstructure for the HP alloys shows higher amounts of precipitates, especially at a higher temperature. These chromium-rich precipitates are associated with M_7C_3 and M_{23}C_6 carbides, whose formation indicates that the alloys are being carburized. However, the SEM technique cannot differentiate M_7C_3 from M_{23}C_6 because of the similar electronic densities of the compounds^[79].

EDS results for C, Al, Cr, Ni, and Fe for the AFA and HP alloys are shown in Figure 3.14. Samples were analyzed by an EDS spectrum in areas of $10\ \mu\text{m}$ thick as depicted in Figure 3.15. The intent of the spectrum analysis was to get an average composition for the elements C, Fe, Ni, and Al, at different distances from surface. A more typical line-scan process would inevitably include data from discrete secondary phases that locally alter the measured compositions. It is also important to note that EDS does not provide an accurate determination of carbon content, and consequently the EDS results are considered as approximate. Therefore, the carbon distribution was treated as an apparent carbon content with a focus on relative differences instead of the absolute values. The purpose of the EDS analysis was to determine the distance at which carbon concentration changes with respect to temperature, and exposure time, rather than measure an accurate composition.

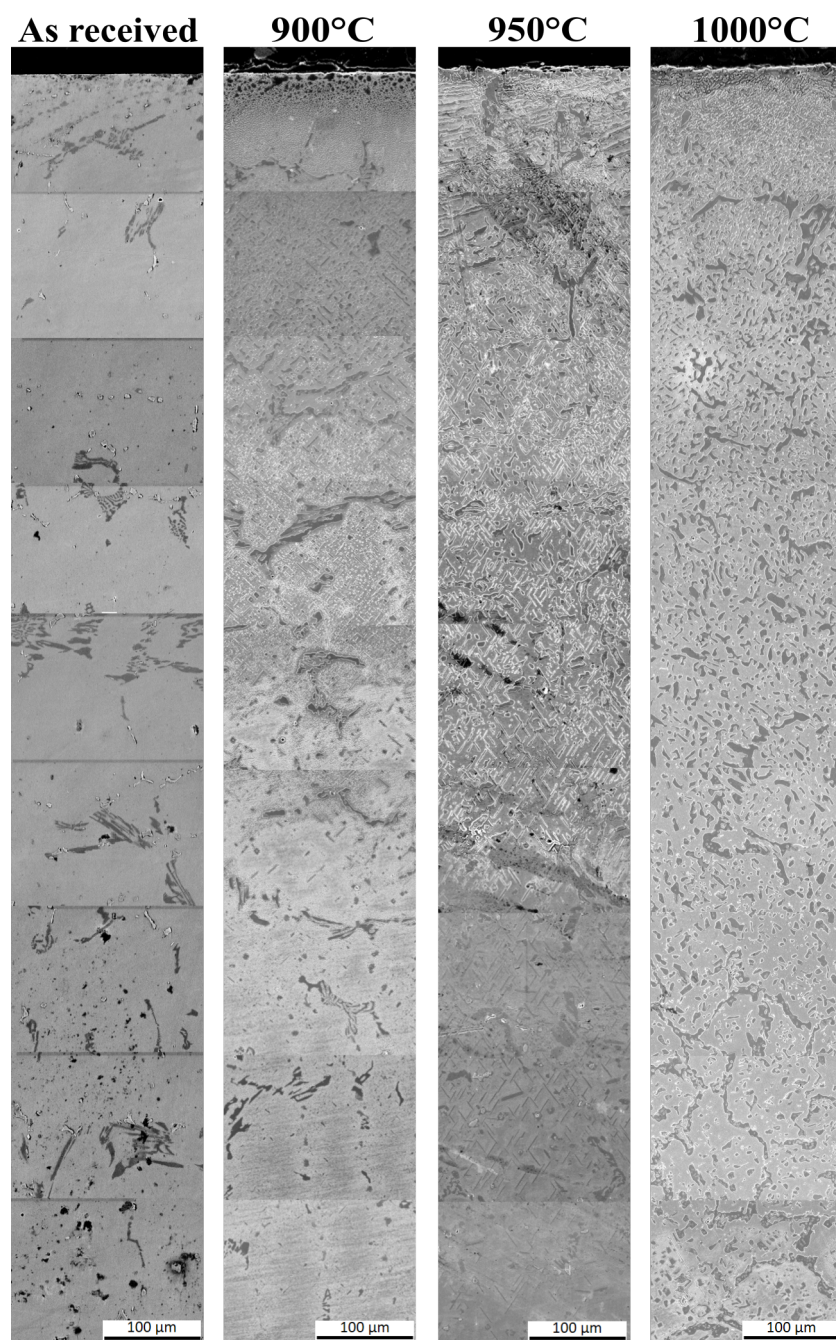


Figure 3.10: SEM cross-sectional images of the HP alloy after 100 h of coking.

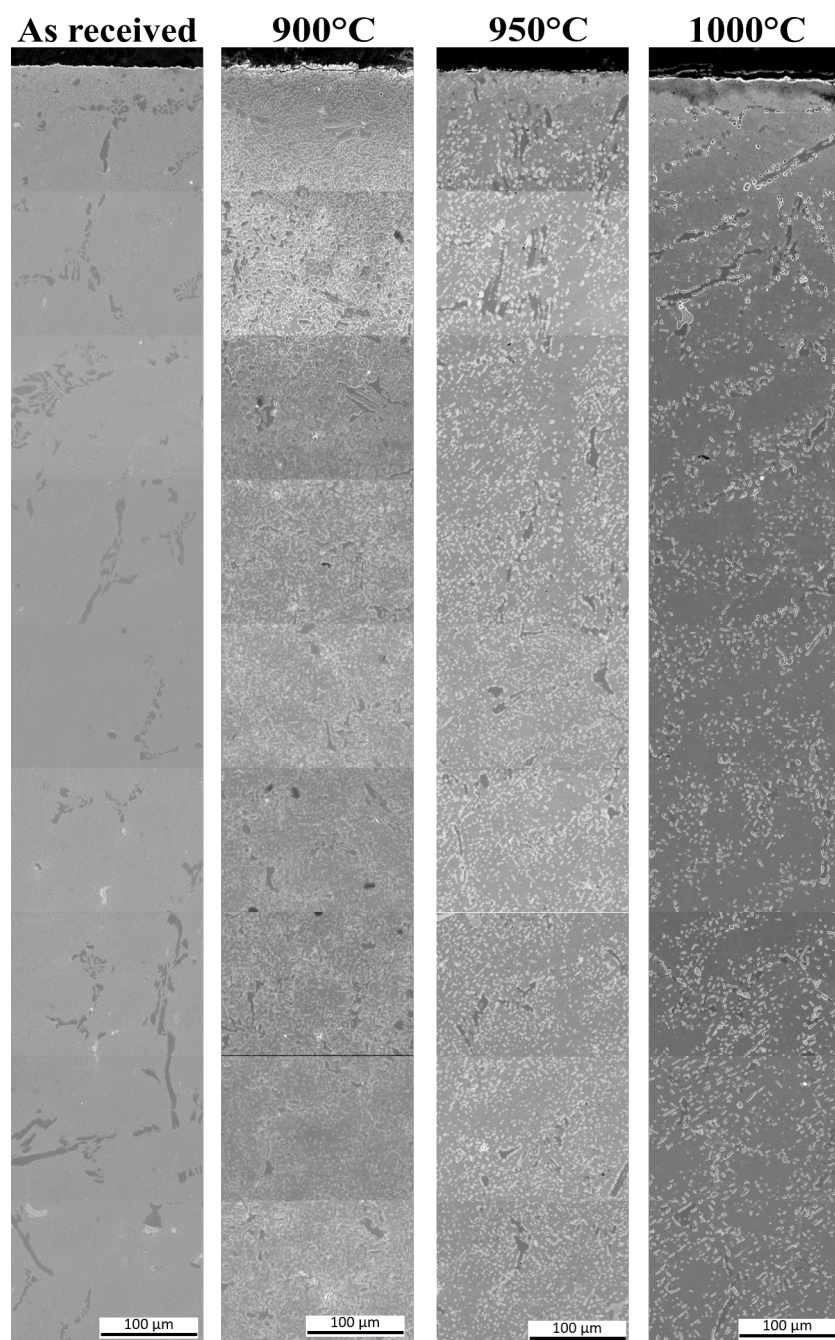


Figure 3.11: SEM cross-sectional images of the AFA-3.2 alloy after 100 h of coking.

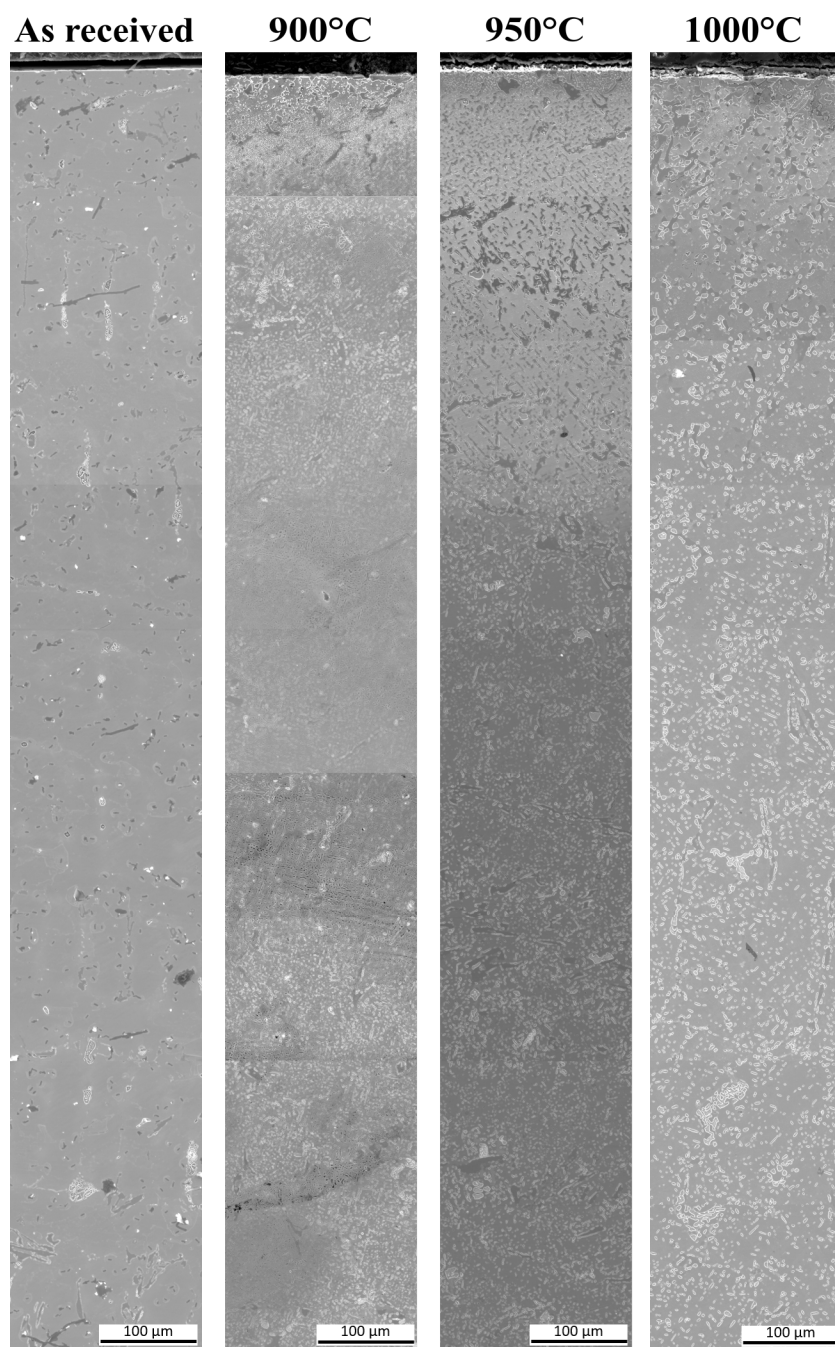


Figure 3.12: SEM cross-sectional images of the AFA-3.5 alloy after 100 h of coking.

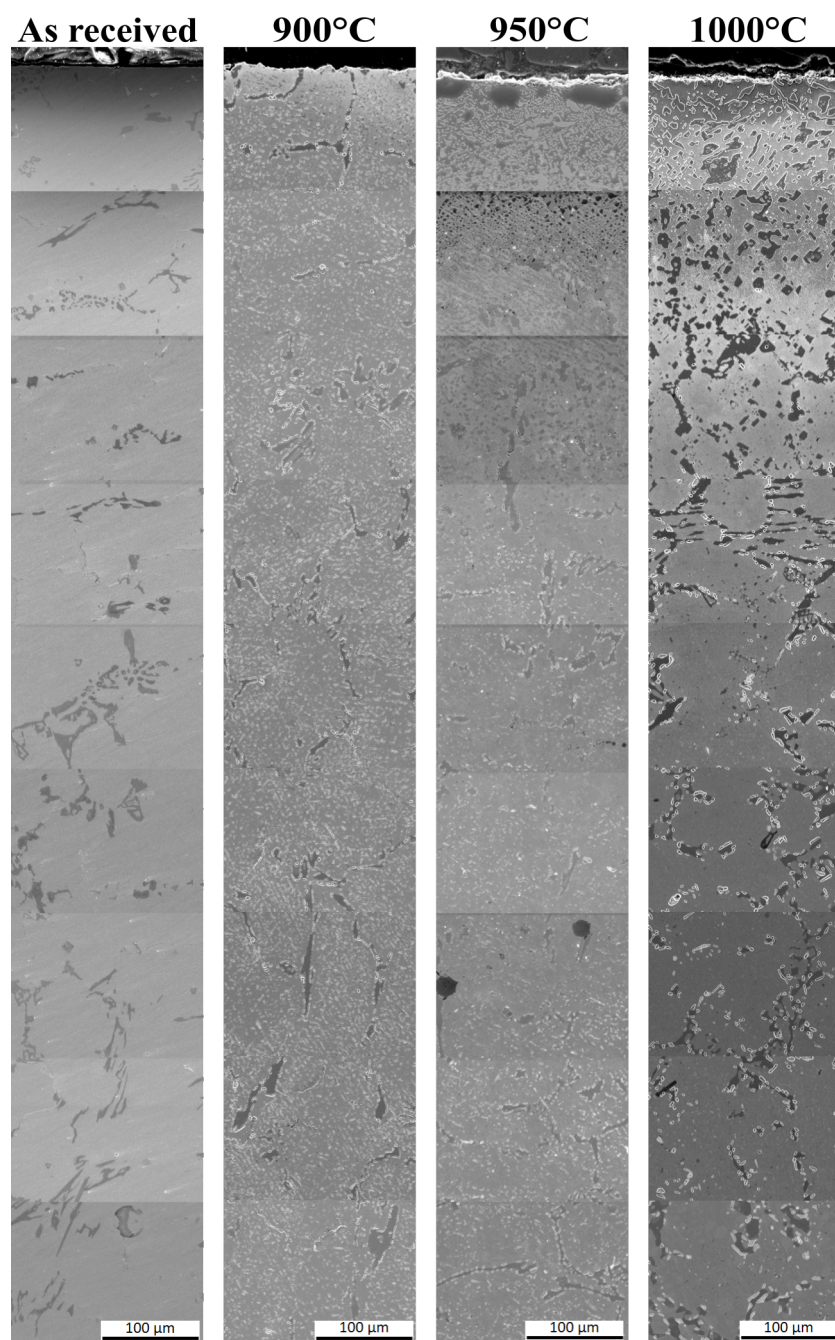


Figure 3.13: SEM cross-sectional images of the AFA-4.0 alloy after 100 h of coking.

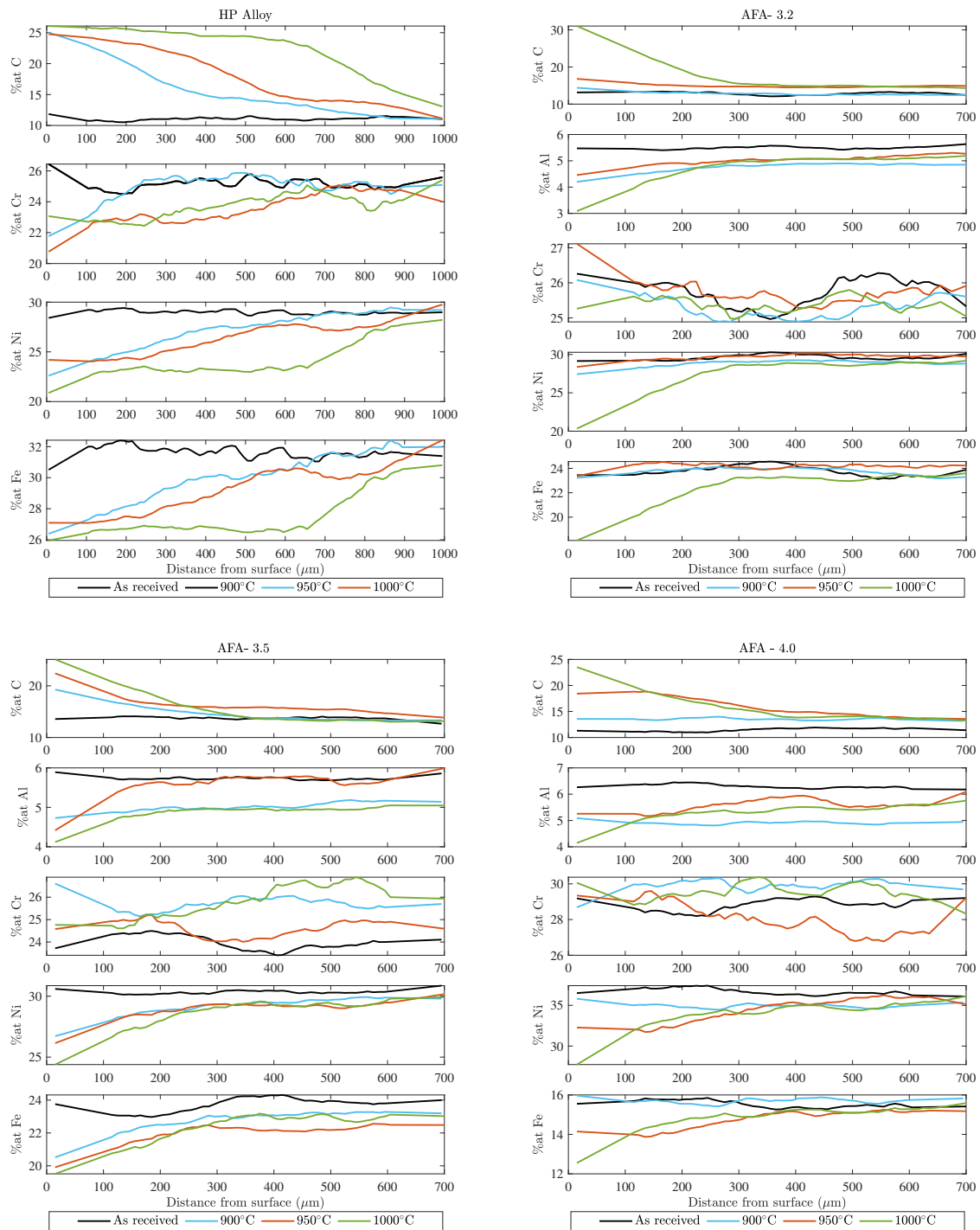


Figure 3.14: Profiles obtained from EDS analysis at three different temperatures for 100 h of coking for each alloy. Data was smoothed using a Savitzky-Golay filter (window=25, order=1).

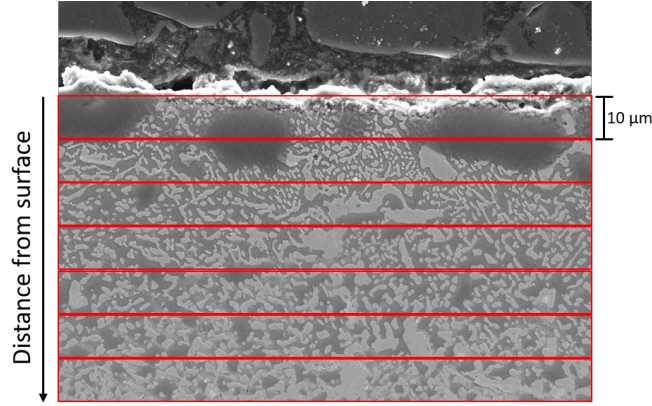


Figure 3.15: Example of EDS area spectrum performed on each sample. SEM image corresponds to the AFA-4.0 alloy exposed after 100 h at 950 °C.

The carbon elemental distributions are shown in 3.16. In the as-received state, the average apparent carbon content was between 10 and 14 at.% for all of the alloys. EDS results showed an increase in the carbon content after exposure to the coking atmosphere.

For the AFA-3.2 and AFA-4.0 alloys, results at 900 °C showed a stable carbon profile, with a slight increase in the carbon content as measured by EDS. This can be correlated with the change of mass data being the lowest for this temperature, and with no carburized layer seen in optical microscopy. This indicates the possibility of carbon diffusion in the matrix but not to the extent to form carbide precipitates. All samples exposed to 1000 °C, showed an increase in the carbon content near the surface with higher carbon values near the surface, when compared to 950 °C data.

For the HP alloy, a clear trend in the carbon profiles with respect to temperature can be seen. Near the surface, EDS results for samples exposed at 900, 950, and 1000 °C showed approximately the same carbon content. However, the 1000 °C sample showed a more distinct plateau at this higher carbon content that extended roughly 700 μm from the surface followed by a decrease to similar values as the as-received sample at 1000 μm .

Additionally, the shape of the carbon profiles, especially for the HP alloy, shows two regions based on the change of slope of the curves. For instance, these regions can be differentiated before and after 300, 600, and 700 μm for the 900, 950, and 1000 °C samples,

respectively. Investigation on the carburization kinetics of heat-resistant steels have found that the carburized layer consist of two zones: an outer zone consisting mainly of M_7C_3 carbides, and an inner zone consisting of mainly $M_{23}C_6$ carbides^[65]. The change of slope in the carbon profiles can be attributed to the type of precipitates formed in the alloy near the surface.

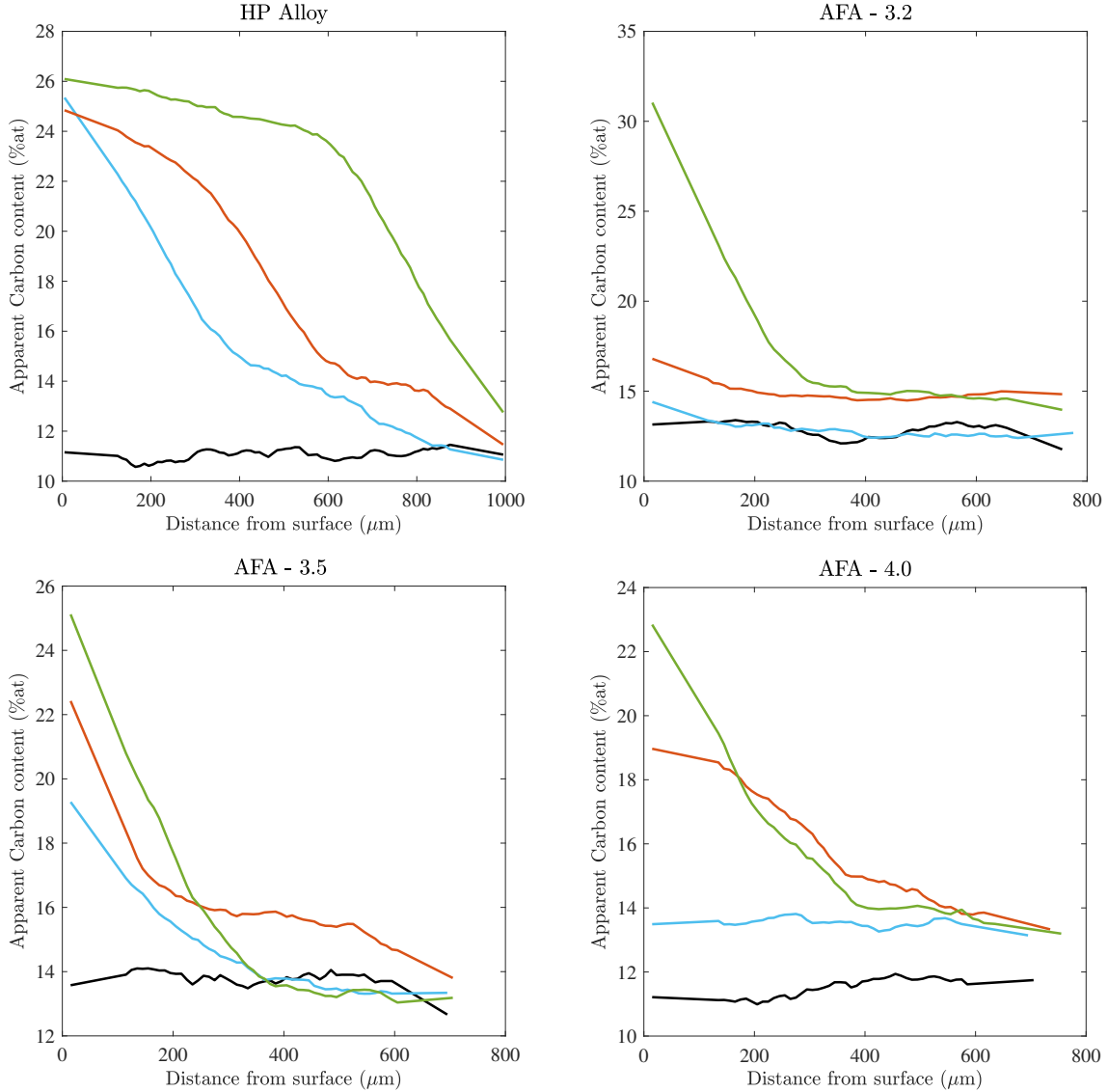


Figure 3.16: Carbon profiles obtained from EDS analysis at three different temperatures for 100 h of coking. Data was smoothed using a Savitzky-Golay filter (window=25, order=1).

3.4.3 Estimation of Apparent Carbon Diffusion Coefficient

The assessment of the carbon diffusion coefficient was carried out by analyzing the diffusion profiles shown in Figure 3.16. Depending on the carbon profile obtained, Fick's second law solution and/or Boltzmann-Matano analysis models were fitted for each alloy.

Fick's second law solution

The initial carbon concentration C_0 , was taken as the average measured value obtained for the as-received state alloys. The carbon concentration at the surface, was defined as the value measured near the surface by the EDS, and time was equal to 100 h. Then, reorganizing equation 3.6 as a linear function as shown in Equation 3.10, and obtaining the slope, the apparent carbon diffusion coefficient can be calculated.

$$\operatorname{inverfc}\left(\frac{C_{x,t} - C_0}{C_s - C_0}\right) = \frac{1}{2\sqrt{D_{app}t}}x \quad (3.10)$$

Data fitted to Fick's second law solution obtained from EDS data for the AFA and HP alloys is shown in Figure 3.17. For the AFA-3.2 and AFA-3.5 alloys, data at 900 °C had a steady carbon value measured as a function of depth, therefore a calculation of the diffusion coefficient was not done since the carbon profile did not fit the shape required for the model. Data at 950 and 1000 °C was fitted according to Fick's second law solution. A change in the slope is seen for at a distance 400 - 500 μm , which corresponds to the start of plateau seen in the carbon profiles (see Figure 3.16). Fick's model assumes that the diffusivity is constant and independent of concentration across the material, and does not consider formation of precipitates. However, the carbon that diffused into the alloy formed chromium precipitates near the surface as described by XRD and SEM results. Then, two carbon diffusion coefficients were calculated: across the sample (for all x), and far from the surface ($x > 400 \mu\text{m}$). The calculated diffusivities for the AFA alloy are shown in Table 3.8.

Table 3.8: Calculated D_{app} using Fick's solution for the AFA alloys. Units are given in $\text{cm}^2\cdot\text{s}^{-1}$.

Alloy	Criteria	900 °C	950 °C	1000 °C
AFA - 3.2	All surface	N/A	1.10×10^{-8}	1.78×10^{-9}
			$R^2 = 0.842$	$R^2 = 0.944$
	x >400 μm	N/A	5.24×10^{-8}	3.42×10^{-8}
			$R^2 = 1.000$	$R^2 = 0.844$
AFA - 3.5	All surface	1.43×10^{-9}	2.47×10^{-9}	9.42×10^{-10}
		$R^2 = 0.980$	$R^2 = 0.957$	$R^2 = 0.983$
	x >500 μm	1.53×10^{-8}	1.65×10^{-9}	1.11×10^{-8}
		$R^2 = 0.843$	$R^2 = 0.975$	$R^2 = 0.923$
AFA - 4.0	All surface	N/A	5.67×10^{-9}	2.95×10^{-9}
			$R^2 = 0.987$	$R^2 = 0.969$
	x >400 μm	N/A	1.09×10^{-8}	3.46×10^{-8}
			$R^2 = 0.992$	$R^2 = 0.990$

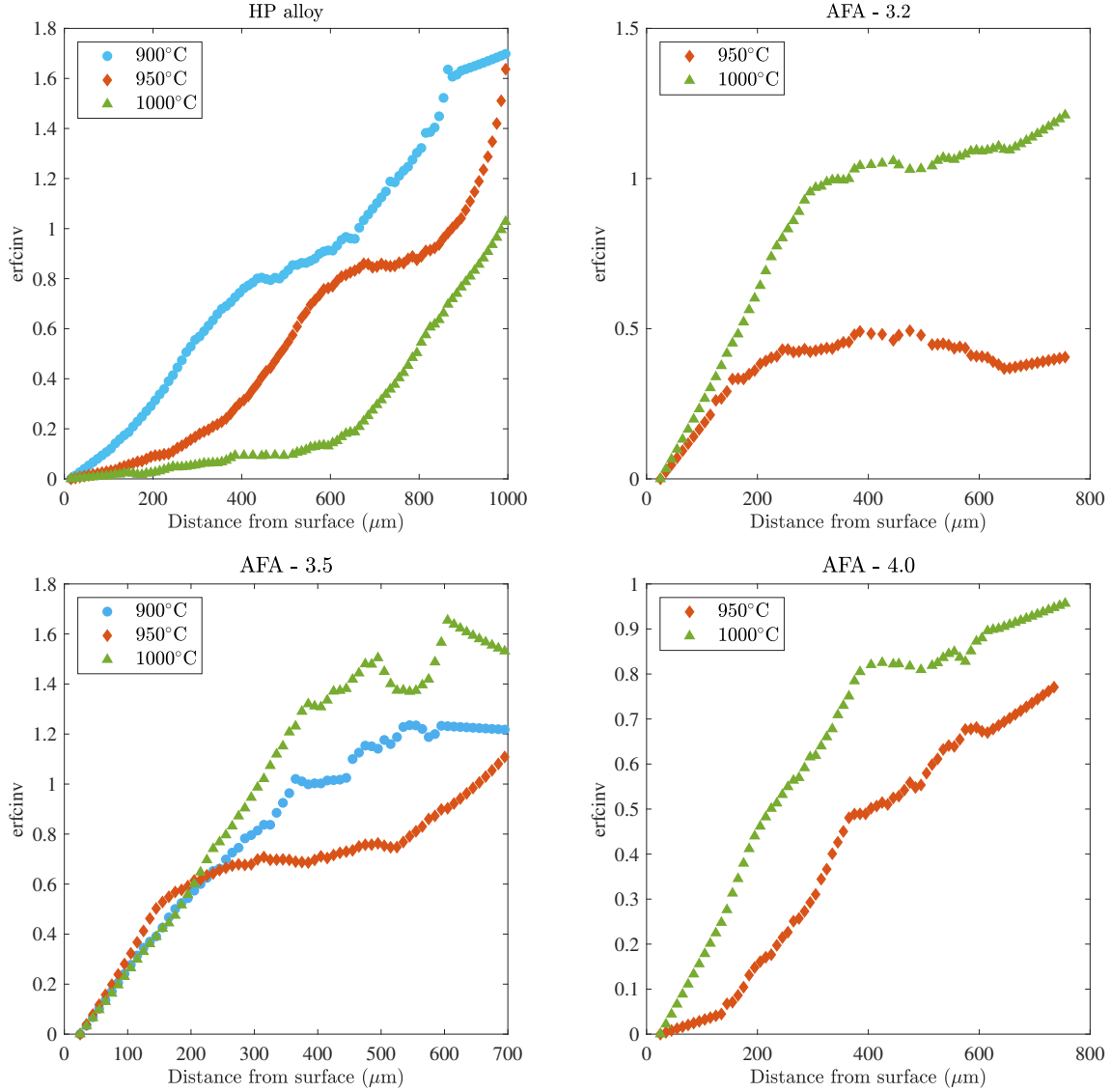


Figure 3.17: Fitted curves to Fick's second law solution model according to equation 3.10.

For the HP alloy, the carbon profiles at 900 and 950 °C tend to fit the shape of Fick's solution model. However, at 1000 °C, the shape does not correlate with the model. A change in the slope for the 1000 °C sample is seen, which is correlated to the presence of chromium precipitates in the alloy. The apparent carbon diffusion coefficients were calculated from the slope of the curves obtained at each temperature using all dataset, and at distances far from the surface ($x > 700 \mu\text{m}$). Data calculated for the HP alloy is shown in Table 3.9.

Table 3.9: Calculated D_{app} using Fick's solution for the HP alloy. Units are given in $\text{cm}^2\cdot\text{s}^{-1}$.

Criteria	900 °C	950 °C	1000 °C
Across all surface	2.40×10^{-9}	4.82×10^{-9}	1.93×10^{-10}
	$R^2 = 0.959$	$R^2 = 0.976$	$R^2 = 0.815$
x > 700 um	1.11×10^{-9}	1.43×10^{-9}	1.21×10^{-9}
	$R^2 = 0.990$	$R^2 = 0.974$	$R^2 = 0.993$

Boltzmann-Matano analysis

To calculate the carbon diffusion coefficient using the Boltzmann-Matano analysis, data obtained at each temperature was corrected by subtracting the average initial composition, obtained from the as-received state alloy. Then, by solving equation 3.7 using finite discrete differences, the apparent carbon diffusion coefficients were calculated as a function of carbon concentration, and distance. Results using this method are presented only for the HP alloy and are being shown in Figure 3.18. The AFA alloy, due to the nature of the carbon profiles shape, did not fit appropriately for Boltzmann-Matano analysis calculations.

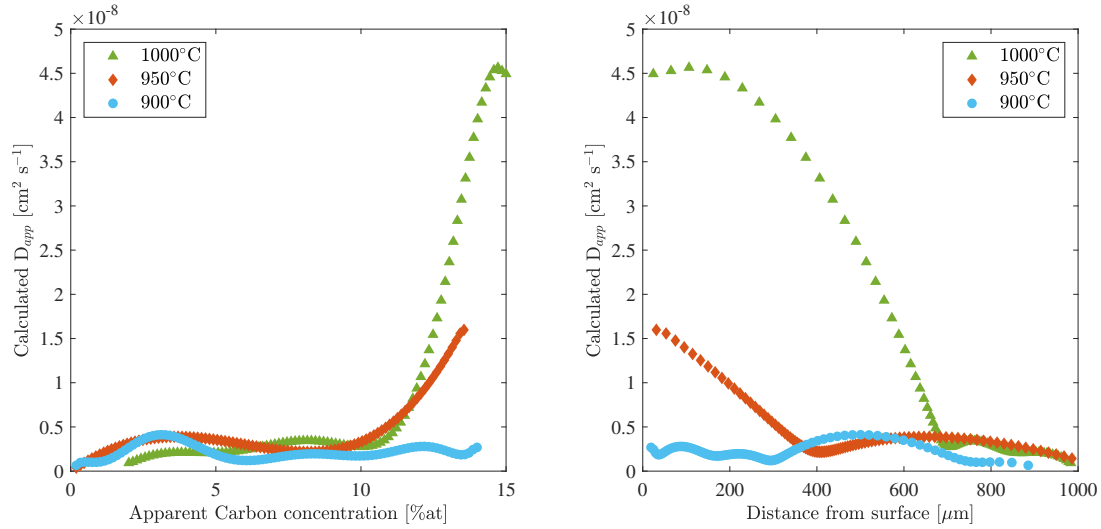


Figure 3.18: Apparent carbon diffusion coefficients as a function of carbon concentration, and distance, using Boltzmann-Matano analysis for the HP alloy.

Based on Figure 3.18, for the HP alloy, the carbon diffusion coefficient is dependent on carbon concentration. Additionally, as carbon concentration decreases with respect to distance from surface, the diffusivity decreases. The correlation between the diffusion coefficient and carbon concentration is related to the carbon interstitials and the formation of precipitates. Near the surface, the alloy is more prominent to form carbon precipitates and increase the carbon interstitials present in the matrix. With respect to temperature, the higher the temperature the higher the diffusion coefficient near the surface. However, at a distance higher than 700 μm , the curves present similar values. These carbon diffusion coefficients correspond to the carbon diffusion in the matrix, where there is no formation of carbides or other precipitates yet.

Discussion of estimation of Apparent Carbon diffusion coefficients

Studies on the carbon diffusion on oxide layers have demonstrated that, in monocrystalline and polycrystalline oxides, there is no detectable solubility of carbon in oxides such as Cr_2O_3 and Al_2O_3 . Then, the carbon diffusion in the oxide is not possible through perfect, dense oxide layers. If carbon diffusion is observed in an alloy that has a preformed oxide layer,

indicates that the layer must have pores, microchannels, or fissures, that allows carbon to ingress into the metal.^[80] Then, the oxide layers formed in both AFA and HP alloys, did not provide a barrier against carbon ingress. The presence of pores, poor scale adherence, and non uniform scale, allowed for carbon diffusion into the matrix, causing chromium depletion due to formation of carbides. This was confirmed by EDS and XRD analysis. However, it is known that in Fe-C alloys, diffusion of carbon is lower through preformed Al_2O_3 than through Cr_2O_3 scales.^[81] Therefore, the mass flux of carbon in AFA alloys is less than that of the HP alloys, resulting in less carburization depth in the AFA alloys because of the presence of the aluminum oxide layer.

The apparent carbon diffusion coefficient for the AFA and HP alloys were obtained at three different temperatures. Two models were used to calculate the coefficients. Fick's second law solution assumes that the diffusivity is constant and independent of concentration. Boltzmann-Matano analysis allows for the calculation of diffusivity as a function of carbon concentration, and therefore, distance. Some aspects that these models do not consider and affect the results are:

- Presence of the coke layer at the surface, was assumed to be a layer that provided constant carbon activity into a stationary metal matrix.
- Carbon is diffusing into the matrix and reacting with other elements (Cr, Fe, Ni).
- Presence of an oxide layer at the surface, which limits the carbon diffusion into the matrix.

The apparent carbon diffusion coefficients as a function of temperature are given in Table 3.10, and correspond to the calculated values far away from the surface. At this depth, the presence of carbides is minimal in the alloys, and then the carbon diffusion coefficient would correspond to the carbon diffusion into the matrix. In the case of the Boltzmann-Matano analysis, the values reported correspond to the average of the coefficients obtained after 700 μm for the HP alloy.

Table 3.10: Apparent Carbon diffusion coefficients for the AFA and the HP alloys obtained from each model. Units are given in $\text{cm}^2 \cdot \text{s}^{-1}$.

Alloy	900	950	1000
HP	6.45×10^{-10}	5.98×10^{-9}	1.00×10^{-9}
HP, BMI	2.49×10^{-9}	3.18×10^{-9}	2.03×10^{-9}
AFA – 3.2	N/A	5.24×10^{-8}	3.42×10^{-8}
AFA – 3.5	1.53×10^{-8}	1.65×10^{-9}	1.11×10^{-8}
AFA – 4.0	N/A	1.09×10^{-8}	3.46×10^{-8}

Most of the reported values in literature are for austenite alloys containing only Fe and less than 0.1%C (see Table 3.2). The discrepancy between the experimental results and the reported values in literature can be attributed to several factors: (1) the AFA and HP alloy contains several alloying elements that will influence the carbon diffusion, (2) presence of oxide layer at the surface lowers the carbon diffusion into the alloy, (3) formation of precipitates as carbon diffuses into the alloy. Therefore, it is expected to have lower carbon diffusion coefficients than those of the Fe-C alloys reported in literature. Additionally, diffusion coefficients were calculated from EDS results, which does not provide an accurate determination of the absolute carbon content, and consequently, results are considered as approximate.

3.4.4 Discussion of Coking Mechanism

As mentioned in Section 3.2, coke deposits are mainly formed due to catalytic and pyrolytic mechanisms. Therefore, the obtained coking kinetics parameters involve surface reactions, subsequent formation of the carbon filaments, and carburization of the alloy because of carbon diffusion. Then, based on literature combined with the obtained results, a mechanism for the coking phenomenon, is proposed as:^[25,29,65,75]

- i Transfer of carbon into the metal phase, by surface reactions and inward carbon diffusion, which leads to oversaturation of the metal

Surface reaction:

- ii Growth of cementite as a layer or particles at the surface, which act as barrier for further carbon ingress
- iii Thereby a high carbon activity is established at the surface, locally graphite nucleates and the carbon activity is reduced to $a_c = 1$, then cementite becomes unstable and,
- iv Cementite decomposes according to $M_3C \rightarrow 3M + C$. The carbon atoms are attached to the graphite and the metal atoms diffuse through the graphite and agglomerate to small particles at its surface
- v These small particles act as catalysts for further carbon deposition according to reaction $C_2H_6 = 3H_2 + 2C$ and vast coke growth results.
 - Metal particles are rich in both iron and nickel, that result of the dissociation of metastable carbides
 - These metal particles are involved in the formation of carbon deposits
- vi Presence of oxide layer act as a barrier for carbon ingress. Diffusion of carbon through Alumina is less than through Chromia.
 - The low oxygen potential in the environment results in a slow formation of an oxide layer, which results in higher ingress of carbon because of a thin, or reduced, oxide layer

Carbon dissolution:

- vii Carbon has dissolved in the metal and diffused inward.
- viii Carbon diffusivity into the alloy is influenced by the presence of other atoms, such as Cr, Fe, Ni, etc.

- Formation of NbC precipitates reduce carbon diffusion in the alloy, acting as a barrier
- Aluminum does not form a very stable carbide. However, it forms a stable oxide.
- Carbides of chromium are very much more stable than those of iron or nickel.

ix Once carbon diffuses into the alloy, there is formation of Cr-rich carbides, M_7C_3 and $M_{23}C_6$.

- M_7C_3 develops as an internal precipitates immediately beneath the alloy surface,
- and $M_{23}C_6$ as precipitate in a zone beneath the M_7C_3

x The metal matrix surrounding the precipitates has been depleted of the carbide-forming elements and consists essentially of iron and nickel

3.5 Summary

Samples of alumina-forming alloys and chromia-forming alloys were exposed to a hydrogen-ethane coking atmosphere at 900, 950, and 1000 °C for 100 h. An analysis of the coking kinetics, microstructural changes, and estimation of the carbon diffusion coefficient was done.

Based on the change of mass data, for all test conditions, the AFA alloy had less mass gained than that of the HP alloy. The change in mass in the alloys was attributed to coking and carburization. Additionally, a trend with respect to the aluminum content was seen for the AFA alloys, where alloys with higher Al wt.% had less mass gained for each temperature.

The coking kinetics was found to follow a parabolic function ($n=0.5$) for both alloys. In addition, the coking kinetic parameters were calculated, obtaining an activation energy of 211 ± 19 and $91.6 \text{ kJ}\cdot\text{mol}^{-1}$ for the AFA alloys and the HP alloy, respectively.

XRD analysis showed the presence of aluminum oxide in the AFA alloys. However, chromium oxide was not detected by XRD for the HP alloy. Peaks for M_7C_3 and $M_{23}C_6$

chromium-rich carbides were observed for both alloys.

Optical images showed that the higher the coking temperature, the more severe was the carburization attack. Additionally, the HP alloy had a uniform carburized layer after exposure to all three temperatures, whereas the AFA alloys, had localized carburization areas at 900 °C and 950 °C.

An estimation of the carbon profiles for the samples was achieved by EDS analysis. The apparent carbon content in the alloy with respect to the surface increased with higher temperatures. The apparent carbon profiles were associated with carburization attack and the formation of carbide precipitates. While the AFA alloy had similar apparent carbon content for all tests, the HP alloy showed a significant increase in the carbon for samples exposed at 1000 °C.

Based on the carbon profiles obtained by EDS, the apparent carbon diffusion coefficients were calculated for each alloy, using Fick's second law solution and Boltzmann-Matano analysis methods. The results gave a good approximation and discrepancies to literature can be attributed to complexity of the matrix, oxide and coke layer present, and formation of precipitates. The calculated carbon diffusion coefficients in the matrix at 950°C are 3.18×10^{-9} and 1.09×10^{-8} for the HP and AFA-4.0 alloys, respectively. The smaller carbon diffusion coefficient in the HP alloy was attributed to a thicker carburized layer, that act as a diffusion barrier of carbon in the matrix.

Overall, based on the kinetics data, microstructural analysis, and estimated carbon profiles, the AFA alloys showed a superior performance to coking compared to the HP alloy.

Chapter 4

Coking Long-term Performance

The aim of this chapter is to present the results obtained for the AFA and HP alloys after 1000 h of exposure to a 30:1 hydrogen-ethane atmosphere, at 950 °C. An analysis of the long-term material performance of the AFA alloys against the HP alloy is discussed based on change of mass, carburization depth, microstructural analysis, carbon profiles and integrity of the oxide layer.

4.1 Introduction

In the refinery and petrochemical industries, austenitic and ferritic alloys are usually used for tubes in fired furnaces where environments are combustion product gases and hydrocarbon gases with low oxygen potentials and high carbon potentials. Usually, the temperature range for exposure of austenitic alloys is 800-1100 °C, and for ferritic alloys 500-700 °C. These processes involve carbon deposition (coking) on the inner diameter, carbon absorption at the metal surface, diffusion of carbon inside the alloy, and precipitation and transformation of carbides to a depth increasing with service.^[14,38]

During thermal and steam cracking operation, carbon is deposited in the form of coke on the internal surfaces of the tubes. The efficiency of heat transfer is reduced and the metal skin temperature increased to maintain the process temperature. The presence of coke eventually

leads to carburization of the tubes when it is periodically removed by oxidation in water vapor and air (de-coking). In addition, the furnace tube material deteriorates with the successive coking-decoking cycles due to corrosion and carburization causing a need for replacement of the reactor coils every 4 to 10 years.^[5] The run length of the reactor before is subjected to decoking, usually varies from 10 to 80 days, depending upon the feed stock, type of reactor and severity of operation.^[39] For a ethane cracker normal run lengths are of the order of 20-60 days, depending upon the operating conditions^[40]. Therefore, an understanding of the long-term material's performance respect to its coking resistance is desirable to reduce the carbon build-up, increase the run length, and then, decrease the operational costs.

In addition, researches have compared the morphological differences in the carbon deposition occurred in austenitic and ferritic alloys exposed for a long time in environments with carbon activity over one in many cases concluding:^[14]

- In a sample of a ferritic alloy Fe-9Cr-1Mo extracted from a tube closed to the outlet of the radiation zone, exposed for 102000 hours at 600 °C showed the evident bulk carburization through all the cross section along the inside diameter. Although this alloy had an oxide layer over the internal surface, the carburization was homogeneous along the internal diameter.
- A tube alloy of austenitic Fe-Ni-Cr (HP40) extracted from a coil of the radiation zone of the furnace exposed for 88000 hours over 900 °C, carburization only occurred along the austenitic grain boundary. A pre-existing oxide scale over the internal surface in this alloy, formed in air before exposure to the carburization environment, reduced or inhibited carburization. Internal carburization was present only in areas where the oxide film was absent.

4.2 Methodology

The methodology followed for the long-term evaluation was described in Section 3.3 with the following differentiation:

- Samples were exposed for a total of 1000 h at 950 °C.
- Mass measurements were taken every 10 h during the first 100 h, and then, every 100 h until the completion of 1000 h of exposure.
- Ten samples per material were evaluated under these conditions, removing one sample of each material every 100 h for characterization.

4.3 Results and Discussion

Samples of each alumina-forming alloy and chromia-forming alloy were exposed for a total of 1000 h at 950 °C to a 30:1 hydrogen-ethane coking atmosphere for evaluation of the long-term coking performance. Alloys were preoxidized before exposure to coking atmosphere. Data collected and summarized in this section include change of mass analysis, kinetics analysis, microstructural changes resulted from exposure, and an analysis on the elemental distribution of the elements with respect to distance from surface.

4.3.1 Determination of coking kinetics rate

To evaluate the amount of coke deposited from a long-term exposure, the specific change of mass with respect to the initial mass of the alloy after 1000 hours of coking is shown in Figure 4.1. Data indicates that after 1000 h of exposure, the AFA alloys had 56% (AFA-3.2), 67% (AFA-3.5), and 96% (AFA-4.0) less mass gained than that of the HP alloy.

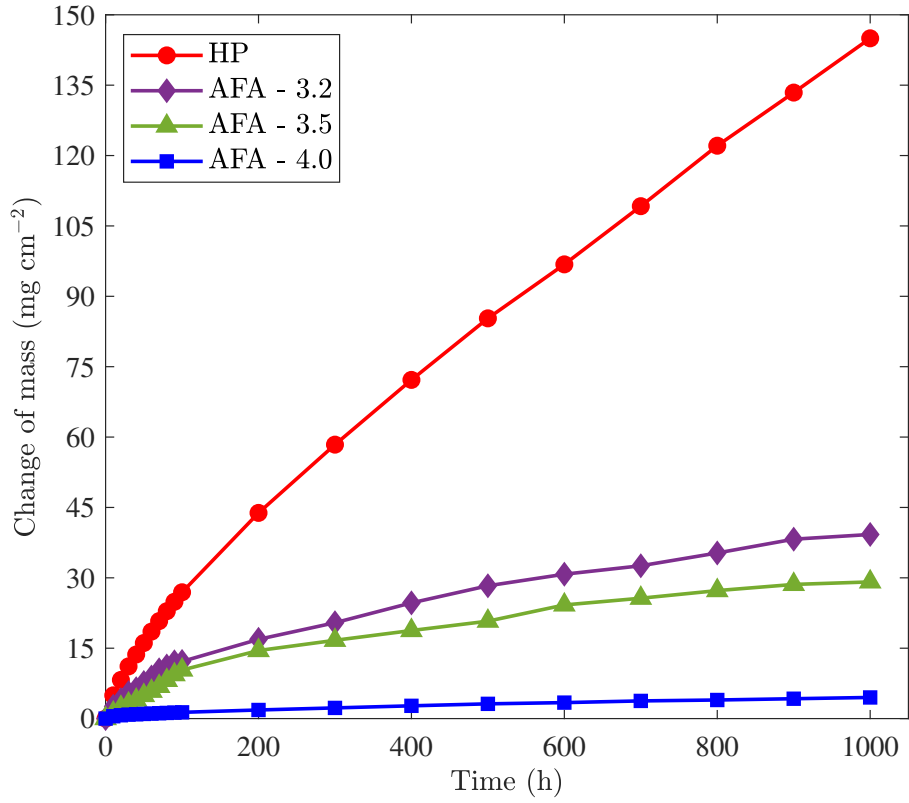


Figure 4.1: Specific change of mass per surface area for alloys exposed to 950 °C for a total of 1000 h. Reported values correspond to 1 sample per material.

With the linearization of the specific change of mass data as shown in Figure 4.2, the kinetic parameters (k and n) were calculated and are shown in Table 4.1. It can be seen that the time exponent of the rate law for a long-term exposure, follows a parabolic behaviour.

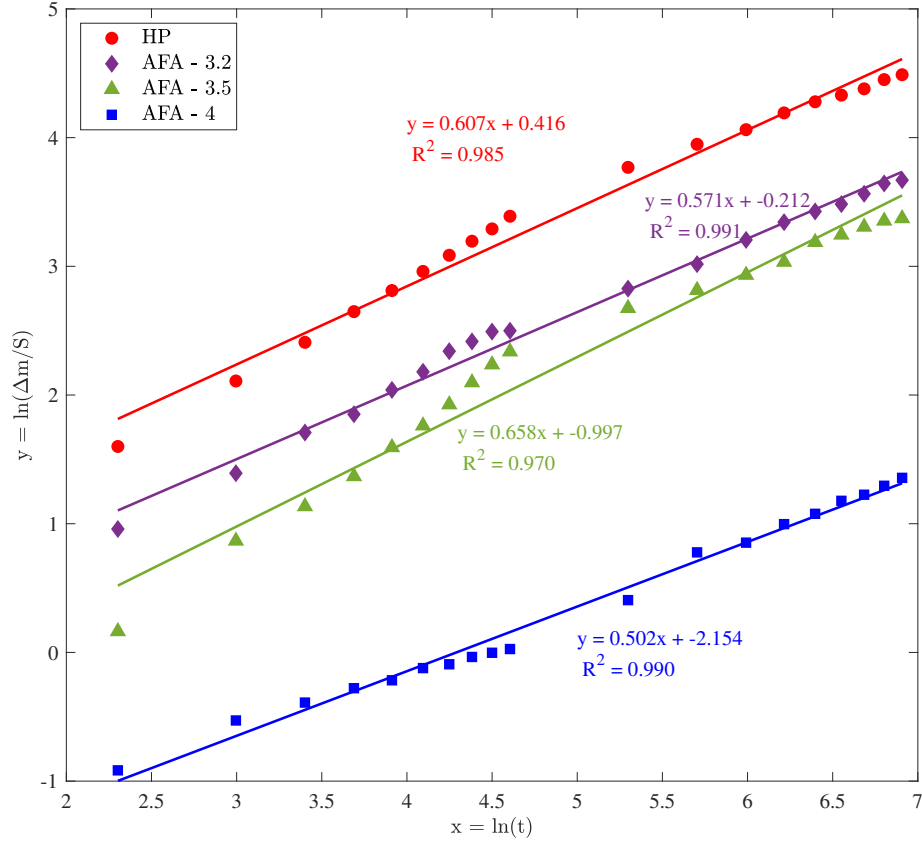


Figure 4.2: Regression data for AFA and HP alloys exposed to the coking atmosphere at 950 °C for 1000 h. Units are given in $\text{mg}\cdot\text{cm}^{-2}$ for $\Delta m/S$, and in hours for t .

Table 4.1: Rate constant (k) and time exponent of the rate law (n) for long-term test. The units of the rate constant are $\text{mg}\cdot\text{cm}^{-2}\cdot\text{h}^{-n}$, and will change according to the time exponent of the rate law.

Alloy	n	k
HP	0.607	1.516
AFA - 3.2	0.571	0.809
AFA - 3.5	0.658	0.369
AFA - 4.0	0.502	0.112

4.3.2 Microstructural Analysis

Digital images of the alloys after exposure to coking conditions for 1000 h are shown in Figure 4.3. The carbon deposited was uniform on all sides. However, after 1000 h of exposure, the HP alloy started to show visible spallation.

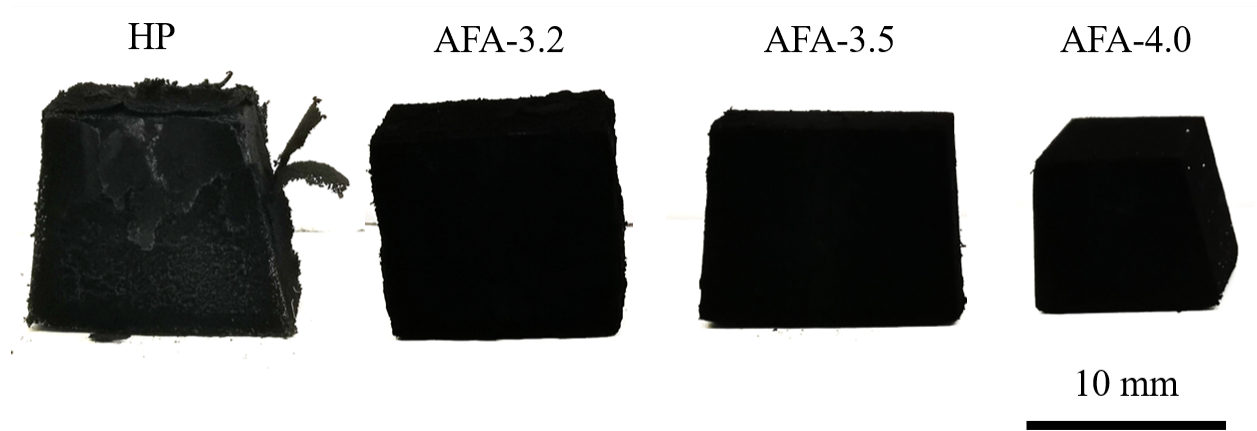


Figure 4.3: Digital images of alloys after 1000 h of exposure to coking conditions

XRD Analysis

XRD analysis after exposure is shown in Figure 4.4. For the HP alloy, the intensity of the carbon peak relative to the matrix becomes predominant after 100 h of exposure. For the AFA alloy, the carbon peak is detectable after 100 h of exposure and continues to increase in intensity with increasing exposure time. Taking a relative intensity (intensity of the main carbon peak divided by the highest peak from a matrix or oxide phase), the carbon peak for AFA at 1000 h has a similar relative intensity as the carbon peak from the HP sample after 100 h. In addition, XRD data for the AFA alloys shows the presence of the alumina layer at all the characterized times. However, same as seen in the coking kinetics tests (see Chapter 3), the chromia layer in the HP alloy was not detected, indicating that it has been partially reduced, or possibly removed by spallation. The presence of both $M_{23}C_6$ and M_7C_3 type carbides can be seen in both alloys. However, at times greater than 300 h, besides carbon, undesirable M_7C_3 carbides are prevalent in the HP alloy, which promote surface hardening.

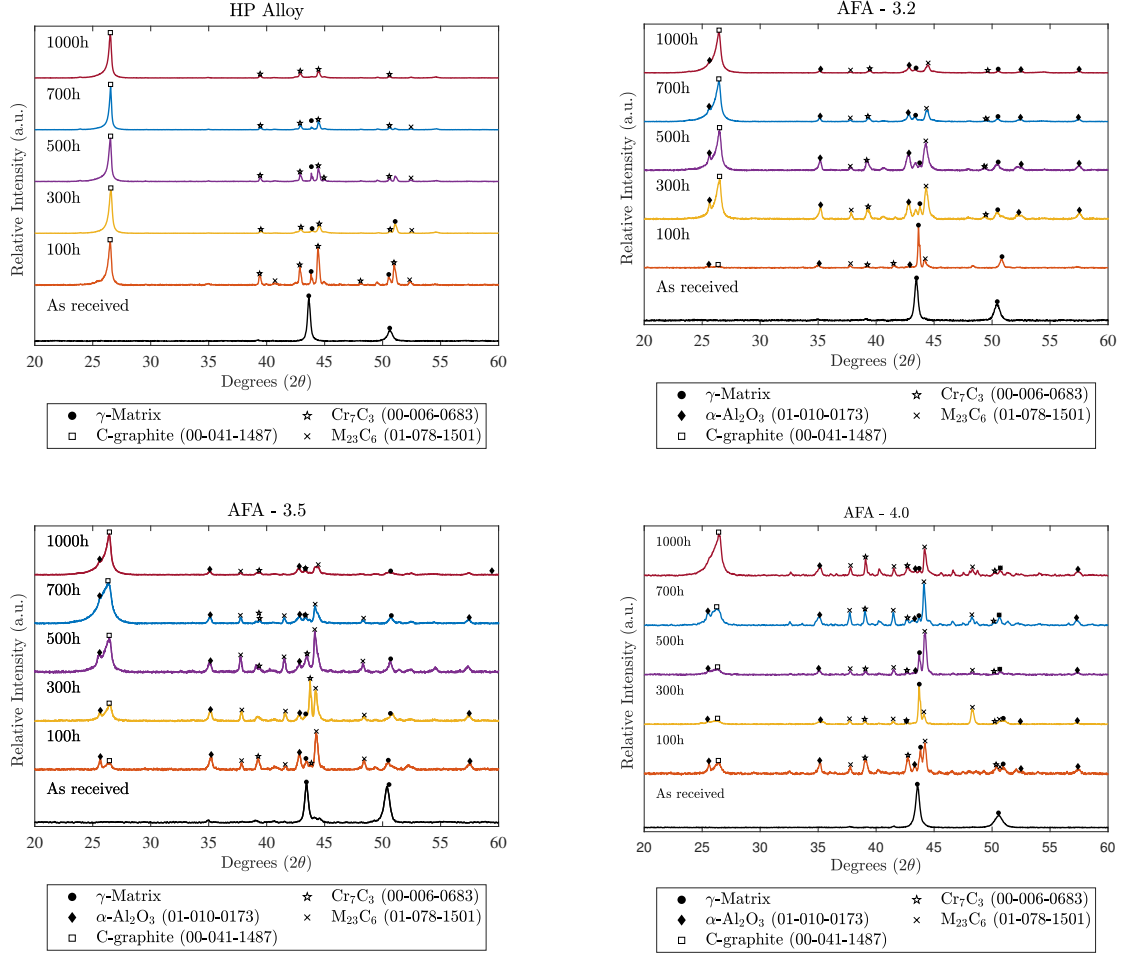


Figure 4.4: XRD analysis for the AFA and the HP alloy after exposure to 950 °C for a total of 1000 h. Each pattern has been normalized between 0 and 1. The JCPDS number of each pattern is shown next to its compound name. The γ -matrix has been associated to the as-cast microstructure.

Optical Microscopy

Optical images of the AFA and HP alloys are shown in Figures 4.6 to 4.5. After 100 h, the AFA alloys showed localized areas of carburization at the surface. However, at times of 300 h or more, a uniform carburized layer was developed for all of the AFA alloys. The AFA-4.0 had the best performance in terms of thickness of carburized layer, reaching 431 μm . In contrast, the HP alloy had a carburization depth of 515 μm after 100 h of exposure, and it continuously increased reaching 2000 μm in carburization depth after 1000 h. A

comparison of the carburization depths is shown in Figure 4.9. After 1000 h of exposure, the carburization depth for the AFA alloy is on average $\sim 77\%$ less than that of the HP alloy.

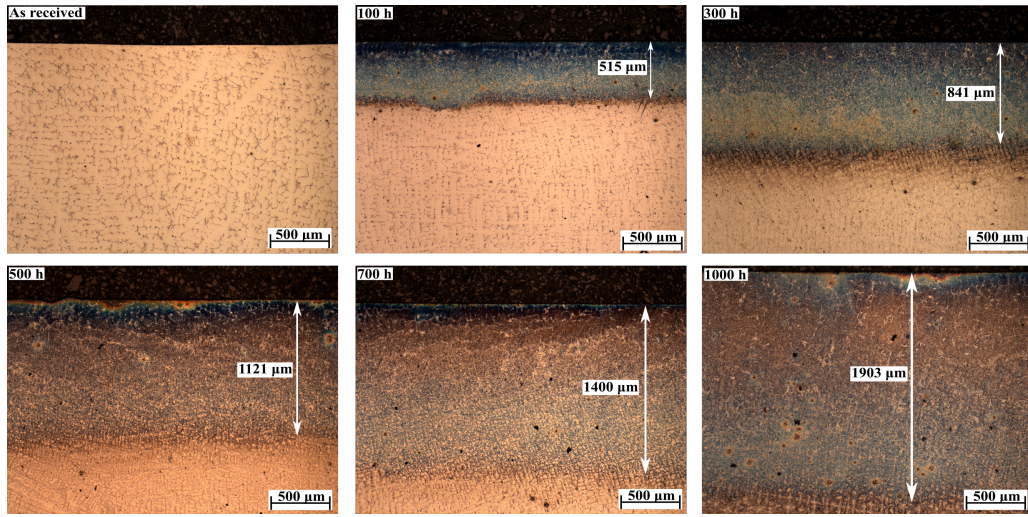


Figure 4.5: Optical microscopy images for the HP alloy after long-term exposure to coking atmosphere.

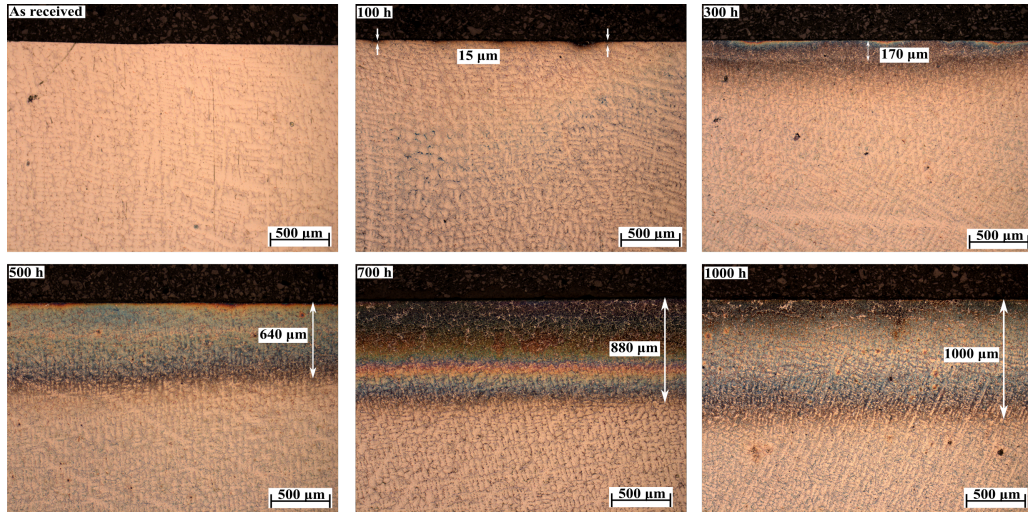


Figure 4.6: Optical microscopy images for the AFA-3.2 alloy after long-term exposure to coking atmosphere.

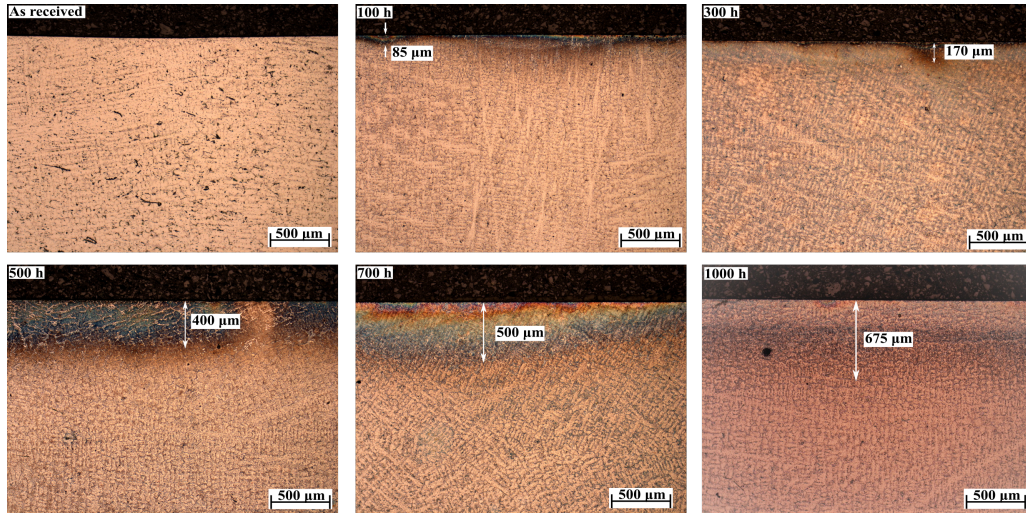


Figure 4.7: Optical microscopy images for the AFA-3.5 after long-term exposure to coking atmosphere.

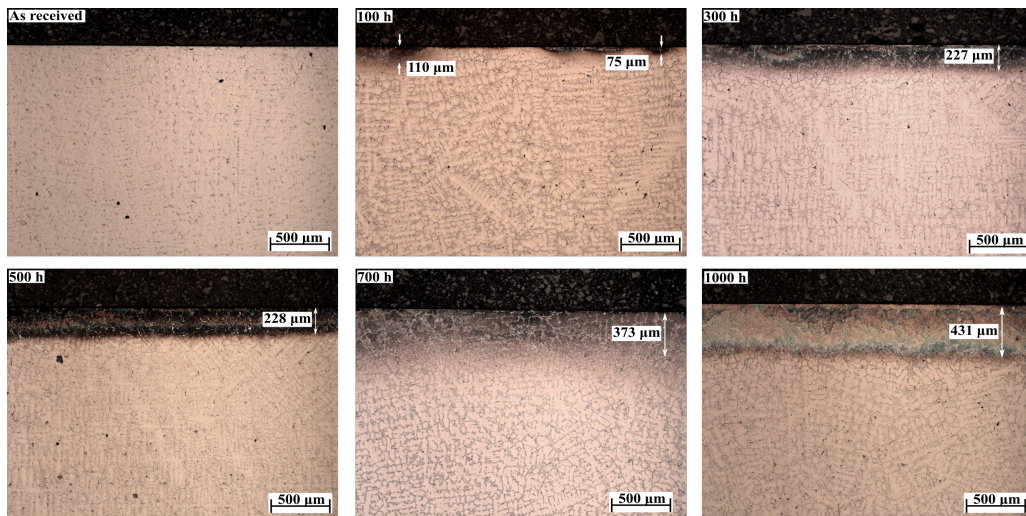


Figure 4.8: Optical microscopy images for the AFA-4.0 alloy after long-term exposure to coking atmosphere.

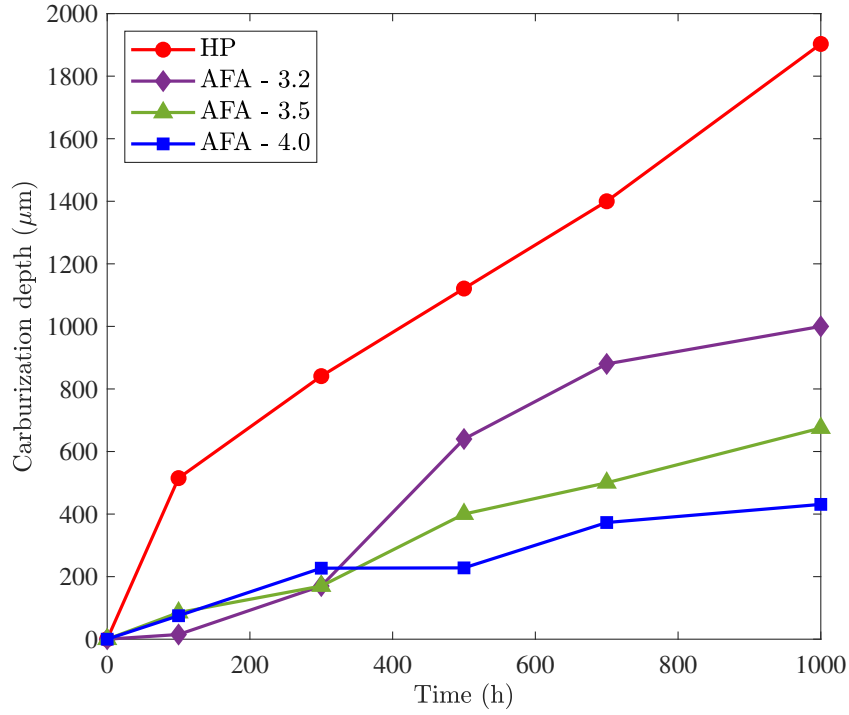


Figure 4.9: Carburization depth measured by optical microscopy for the AFA and HP alloys.

SEM/EDS Analysis

SEM cross-sectional images of alloys after exposure at 950°C for a total of 1000 h are shown in Figures 4.10 to 4.13. The intent of the images is to show the microstructural changes in the alloys with respect to time. In general, the majority of the samples started to show a significant change in microstructure after exposure of 500 hours. From the AFA alloys, the AFA-3.2 alloy had the highest amount of precipitates. However, from all the alloys, the HP alloy shows the highest amount of precipitates, especially at times longer than 500 h. These chromium-rich precipitates are associated with M_7C_3 and $M_{23}C_6$ carbides, whose formation indicates that the alloys are being carburized.

In addition to SEM, samples were analyzed by an EDS spectrum and all element profiles are shown in Figure 4.14. All the analysis were done up to at least 700 μm distance from surface. In the case of the HP alloy, EDS analysis was done at a higher depth, and it was found that the carbon concentration did not reach concentrations close to the initial values

because the whole sample had been carburized. This can be seen that, for the 1000 h sample, EDS was done reaching $\sim 2000\ \mu\text{m}$ and still EDS measured higher carbon concentration.

When analyzing the carbon profiles as a function of time, as shown in Figure 4.15, it can be inferred that the higher the exposure time, the higher the amount of carbon content was measured by the EDS. In the case of the HP alloy, a similar trend was seen for 100 h and 300 h samples. However, after 500+ hours of exposure, the carbon content in the alloy increased significantly. In contrast, the AFA material had only a gradual increase in carbon content with increasing exposure times.

Moreover, from the element profiles, it can be seen that for the majority of the samples, higher amount of chromium was detected after exposure, especially after 1000 h. Likewise, depletion of Ni and Fe were detected, specially in the HP alloy. This could indicate metal depletion due to formation of Fe oxides, spinel oxide formation, and metal evaporation.

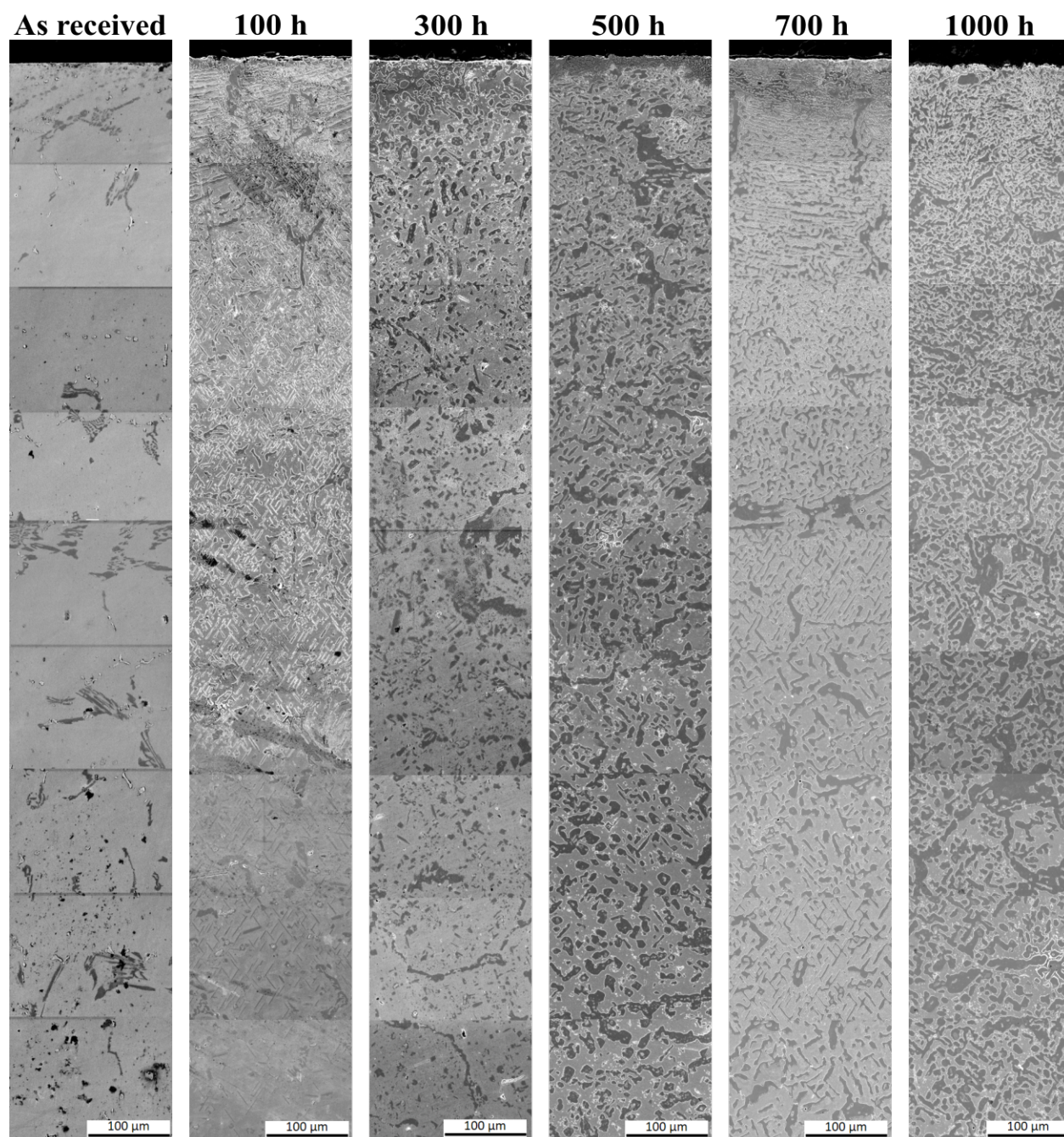


Figure 4.10: SEM cross-sectional images of the HP alloy after 1000 h of coking.

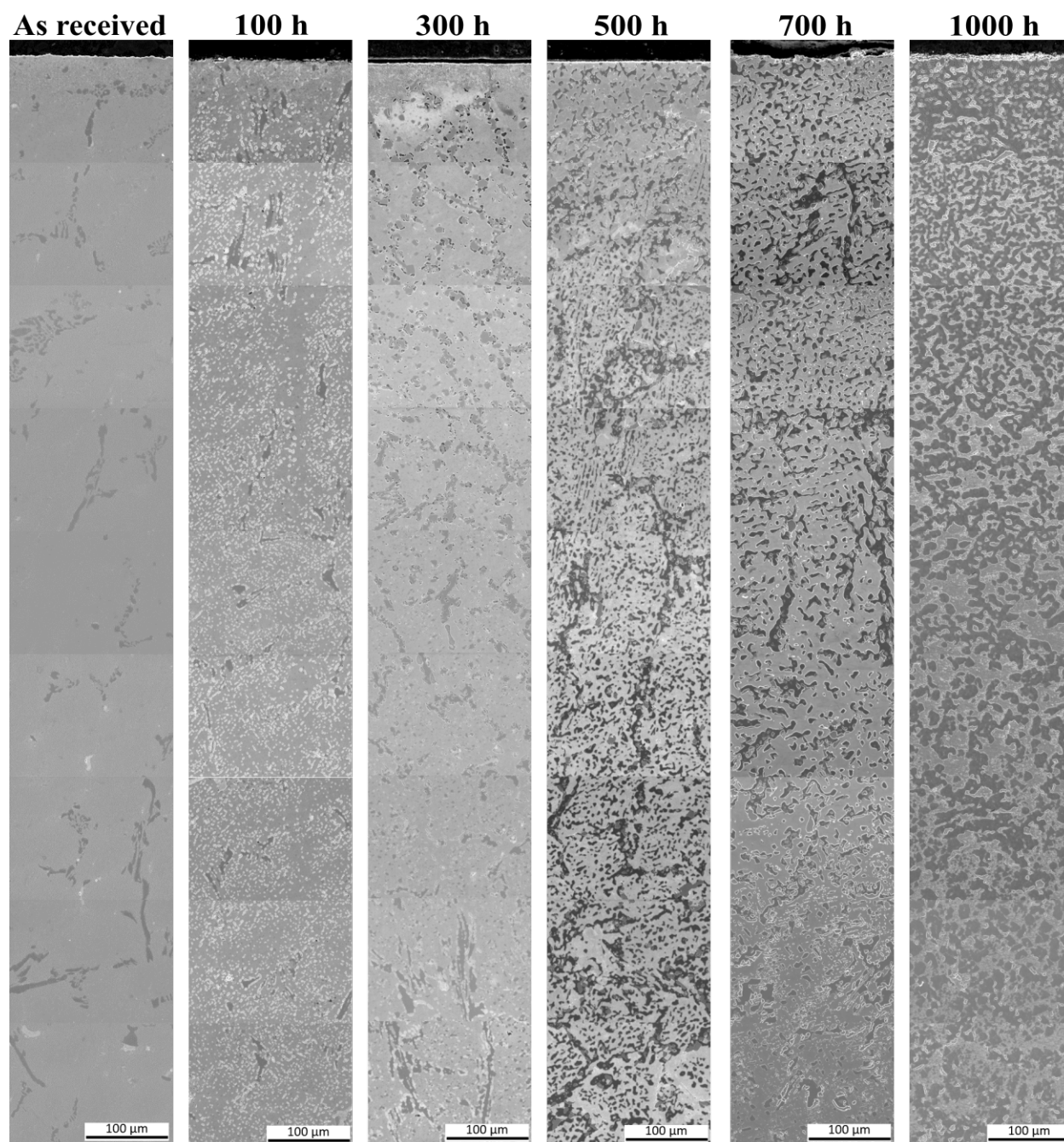


Figure 4.11: SEM cross-sectional images of the AFA-3.2 alloy after 1000 h of coking.

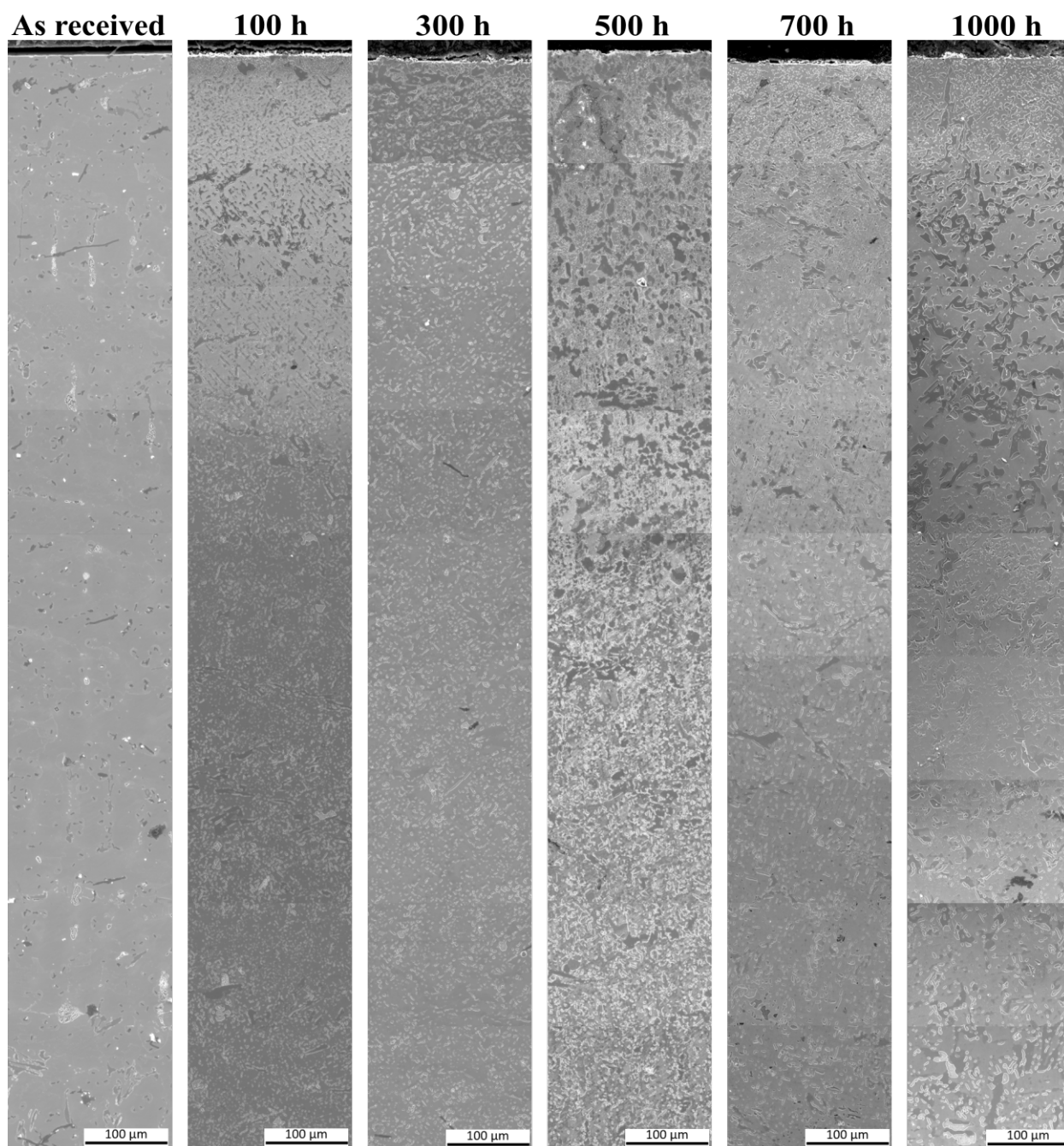


Figure 4.12: SEM cross-sectional images of the AFA-3.5 alloy after 1000 h of coking.

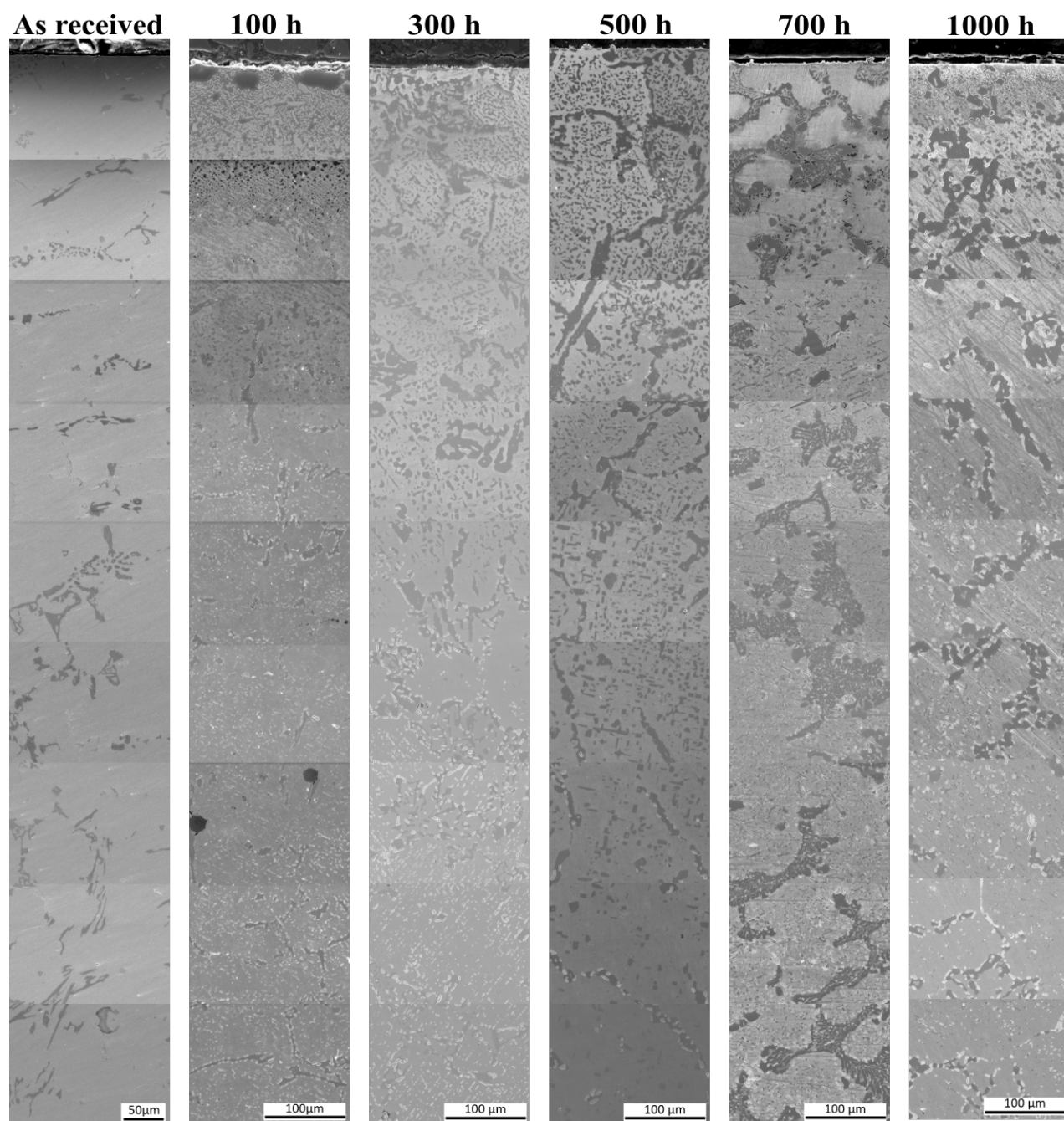


Figure 4.13: SEM cross-sectional images of the AFA-4.0 alloy after 1000 h of coking.

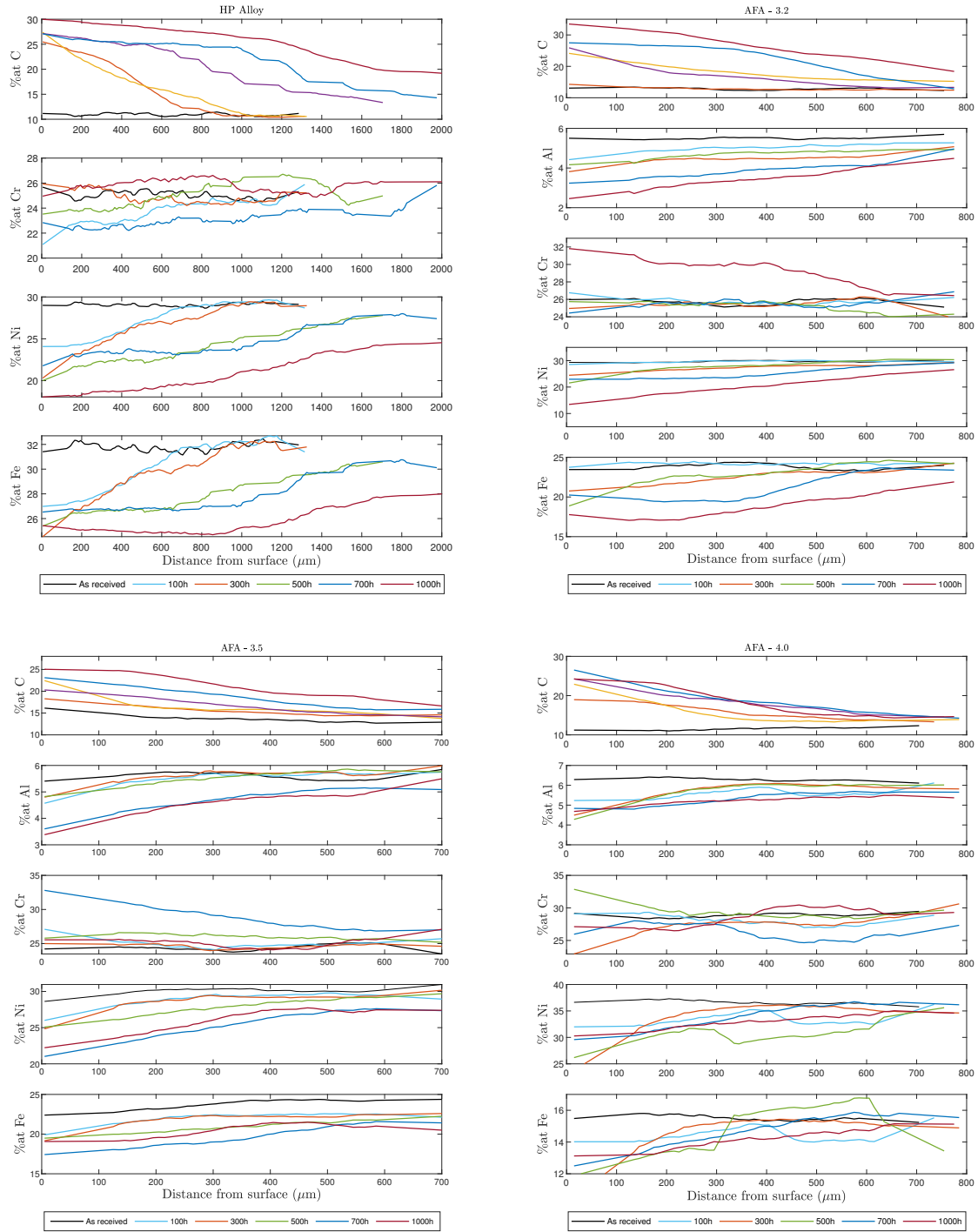


Figure 4.14: Profiles obtained from EDS analysis after 1000 h of coking at 950 °C. Data was smoothed using a Savitzky-Golay filter (window=25, order=1).

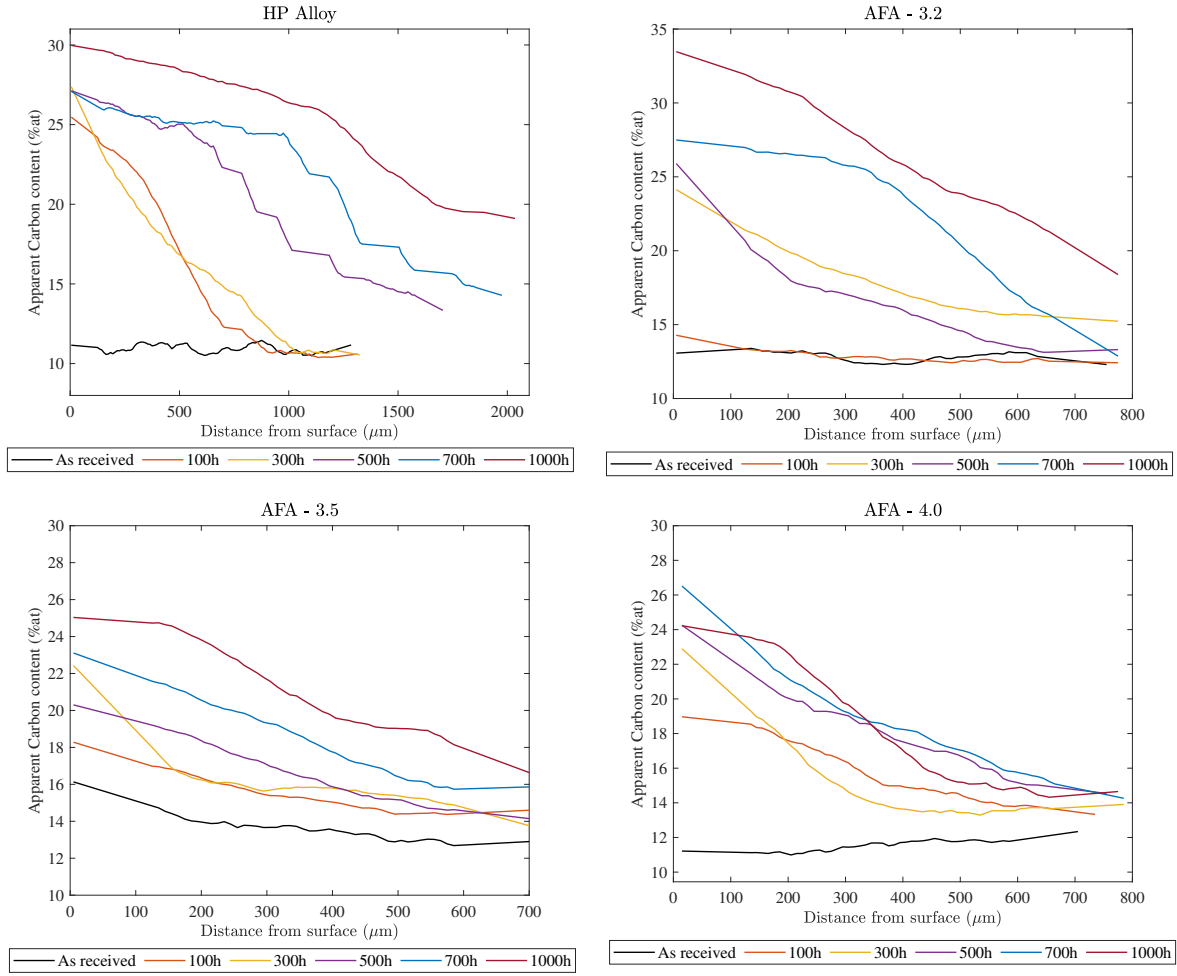


Figure 4.15: Carbon profiles obtained from EDS analysis after 1000 h of exposure. Data was smoothed using a Savitzky-Golay filter (window=25, order=1).

4.4 Integrity of the oxide layer

The integrity of the oxide layer can be described by high magnification SEM images of the cross sectional samples as shown in Figure 4.16. It can be seen that there is no presence of chromium oxide layer in the HP alloy, while a uniform alumina layer is visible in all AFA alloys. In addition, the HP alloy and the AFA-3.5 alloys had high carbide precipitation near the surface, with bigger precipitates formed in the HP alloy. The AFA-3.2 alloy had presence of carbides but not to the same extent as the AFA-3.5 alloy. In contrast, the AFA-4.0 alloy did not show precipitates near the surface.

As previously discussed in Section 3.4.3, the presence of a uniform and a dense oxide layer will limit the carbon diffusion into the alloy, resulting in less formation of carbide precipitates. The SEM image for the AFA-4.0 alloy, showed a uniform oxide layer of 1.26 μm in thickness. While the other two AFA alloys had thicker alumina scales, the density and adherence was not as good as of the scale developed for the AFA-4.0 alloy. Then, the less amount of precipitates seen near the surface for this particular alloy, can be attributed to a better alumina scale developed at the surface.

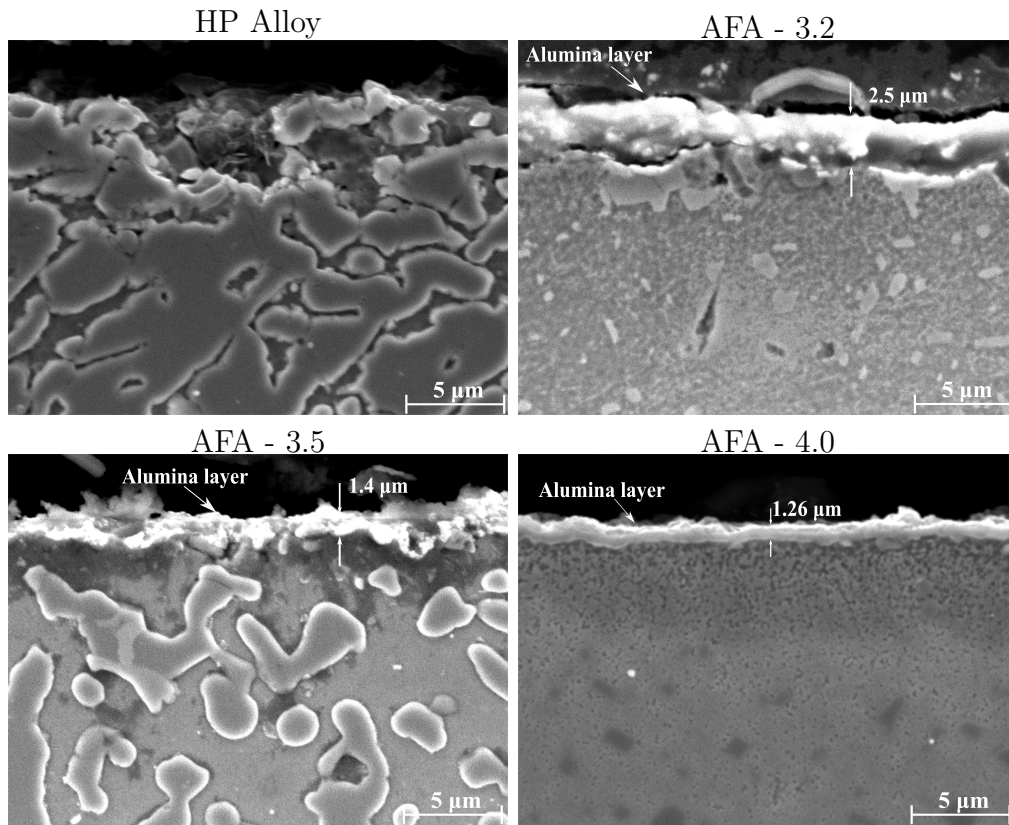


Figure 4.16: High magnification SEM cross-sectional images of samples after exposure to coking conditions for 1000 h (5000x, working distance of 13 mm)

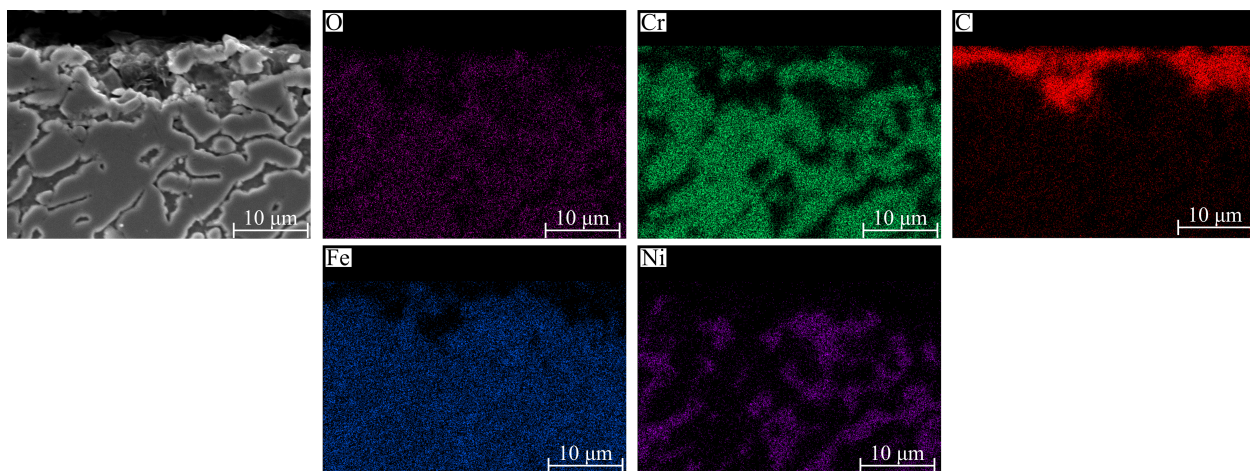


Figure 4.17: EDS analysis of the HP alloy after 1000 h of exposure to coking conditions.

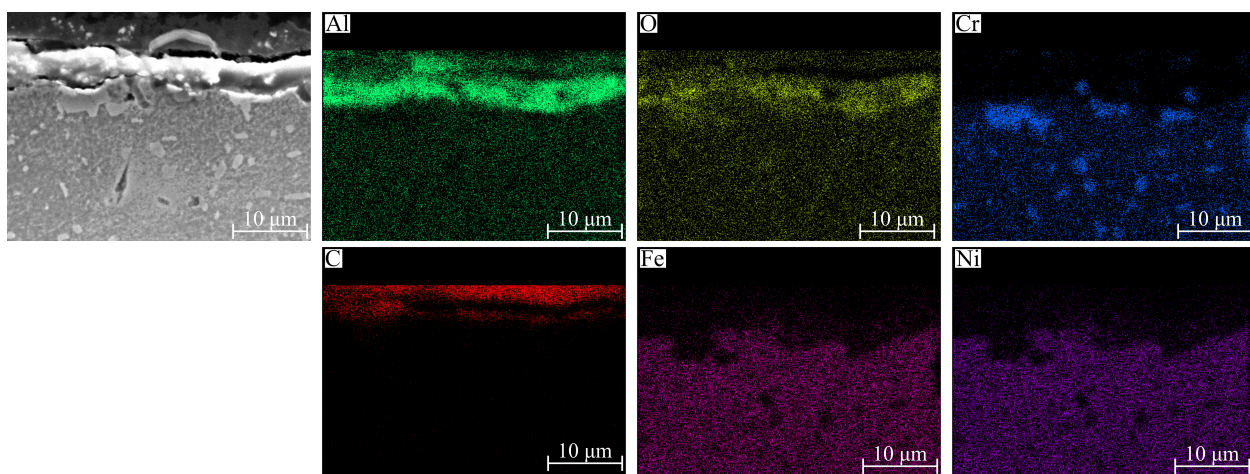


Figure 4.18: EDS analysis of the AFA-3.2 alloy after 1000 h of exposure to coking conditions.

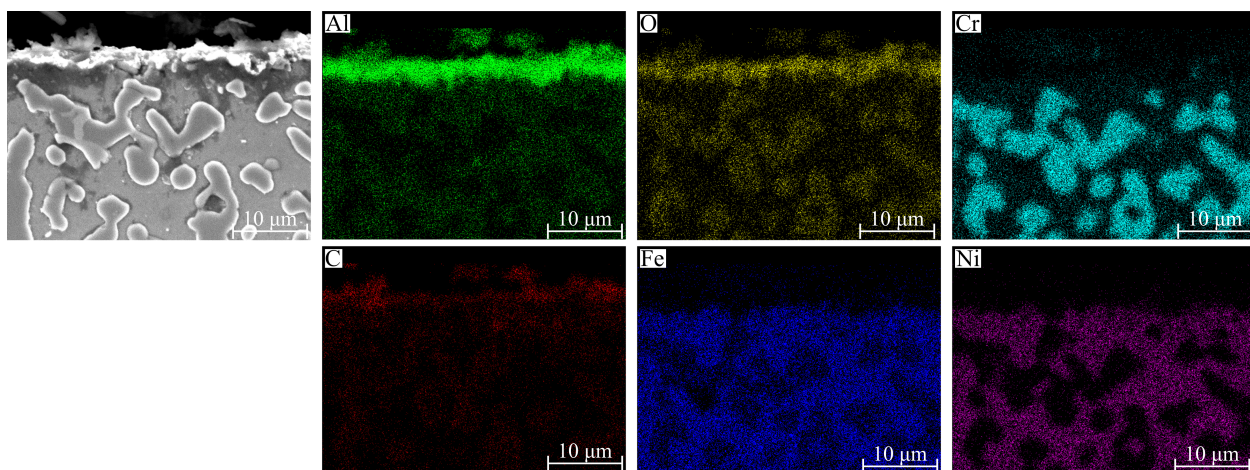


Figure 4.19: EDS analysis of the AFA-3.5 alloy after 1000 h of exposure to coking conditions.

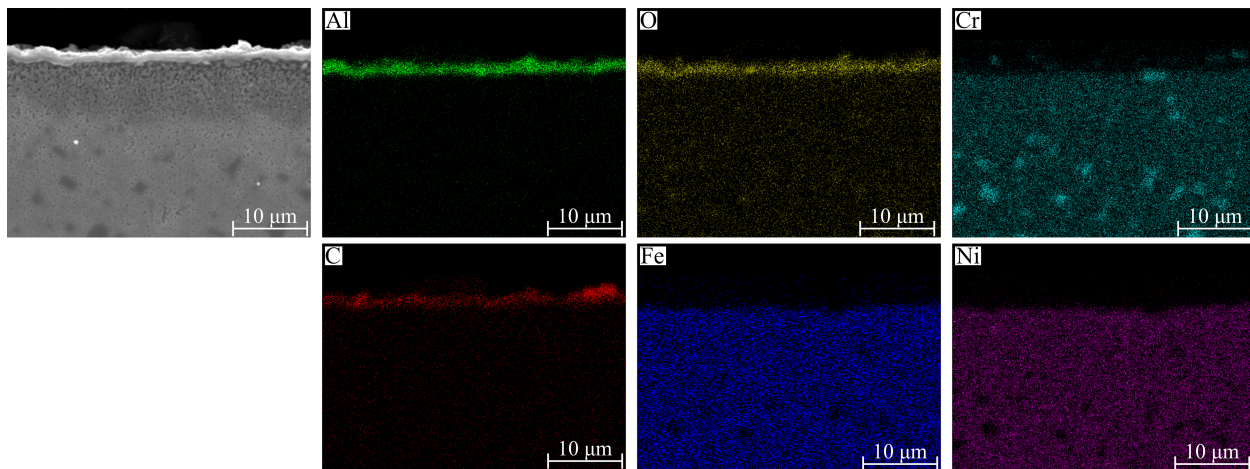


Figure 4.20: EDS analysis of the AFA-4.0 alloy after 1000 h of exposure to coking conditions.

4.5 Summary

Data of samples of alumina-forming alloys and chromia-forming alloys that were exposed to a hydrogen-ethane coking atmosphere at 950 °C for 1000 h was presented. An analysis of the long-term coking kinetic parameters, microstructural changes, and element profiles were done.

Based on change of mass data, the AFA-4.0 alloy had $\sim 91\%$ less mass gained than that of the HP alloy after exposure. From optical microscopy, the same alloy had 77% less carburization depth than that of the HP alloy. In addition, the coking kinetics was found to follow a parabolic function ($n=0.5$) for all alloys. XRD results showed aluminum oxide peaks for all of the AFA alloys at all times. However, M_7C_3 peaks only after 500+ hours of exposure for the HP alloy. In addition, for the AFA alloys at 700+ h, carbon peaks had a similar relative intensity to that of the HP alloy at 300 h.

An estimation of the carbon profiles for the samples was achieved by EDS analysis. The apparent carbon content in the alloy with respect to the surface increased with longer exposure times. The apparent carbon profiles were associated with carburization attack and the formation of carbide precipitates. While the AFA alloy had similar apparent carbon content for all tests, the HP alloy showed a significant increase in the carbon for samples

exposed at times higher than 500 h.

Overall, in terms of mass data, carburization and EDS profiles, the AFA - 4.0 had superior performance in long-term coking conditions. The HP alloy had the highest amount of carburization and changes in microstructure, making it not as suitable as the AFA alloys for long-term coking exposures.

Chapter 5

Coking-Decoking Cyclic Conditions

The aim of this chapter, is to present results of samples of alumina-forming and chromia-forming alloys that were exposed to 10 coking-decoking cycles, to compare early-stage performance and identify if oxide spallation and change to base metal microstructure would be observed. Alloys were preoxidized as described in section 2, before exposure to cyclic atmospheres. The coking atmosphere consisted of a mixture of hydrogen and ethane at 950 °C, and the decoking atmosphere consisted of 100% steam at 850 °C. Data collected includes a microstructural analysis, change in mass, and mechanical property changes resulted from preoxidation and coking-decoking cyclic processing. By addressing the metallurgical changes as well as any damage from the exposure to cyclic conditions, the durability of the alumina-forming alloys relative to a traditional chromia-forming alloys is described. Data presented in this chapter has been previously published.^[28]

5.1 Introduction

Studies of carbon formation in different cracking atmospheres, coating technologies, and the influence of operating parameters such as temperature, pressure, and gas ratios combined with modifications in the coil geometry have been conducted mostly on chromia-forming alloys in order to understand the process itself and possibly reduce the coke layer forma-

tion^[14,48,54,77,82-84]. Whereas, studies of the effects of thermal cracking atmospheres, with a focus on cyclic conditions, on alumina-forming materials instead of the traditional chromia-forming alloys have yet to be fully investigated. Of all the challenges, the reduction in the number of coking-decoking cycles has been identified as an important issue related to the lifetime of the reactor, operating costs, and loss of ethylene production.

Investigations on HP40Nb alloys previously preoxidized and subsequently exposed to an alternating carburizing/oxidizing/carburizing atmosphere at 1000 °C have concluded that a thick Cr₂O₃ layer formed on surface which partly spalled off during cooling to room temperature, in this way chromium depleted areas resulted at the surface.^[77] Additionally, during second exposures to the carburizing atmosphere, there was more catalytic coke formation compared to the first exposure showing that, the reduction of the oxides promotes the formation of (Fe, Ni)-particles which show strong catalytic activity towards coke formation.^[85] The catalytic coke formation during thermal cracking in hydrogen rich hydrocarbon atmospheres is caused by the presence of a porous (Fe, Ni, Cr-) spinel layer at the metal surface which is formed during the oxidation step. However, severe pre-oxidation of the metallic surface followed by rapid cooling and spalling of the oxide layer causes chromium depletion. Once there is chromium depletion and there is contact with a carburizing atmosphere, formation of rich carbide decreases the chromium concentration of the metallic matrix. Therefore, it has been found that repeated coking operations result in the reduction of the spinel into highly catalytic Fe and Ni particles leading to grow a catalytic surface and therefore an increasing in the coking rate.^[77,86]

5.2 Methodology

5.2.1 Material composition

One alumina-forming alloy (AFA-3.8) and one chromia-forming alloy (HP)^[73], both produced via centrifugal casting, were tested. The nominal composition for each alloy is described in

Table 5.1 with elements related to mechanical strengthening (Nb, Mo, C, etc.) omitted due to the proprietary nature.

Table 5.1: Nominal compositions of the alloy samples

Alloy	Al	Cr	Fe	Ni	Other
AFA-3.8	3.8	23	33	37	+additions
HP	0	26	35	34	+additions

5.2.2 Sample preparation

Samples were prepared from as-cast pipe sections, cut with an abrasive saw, ground to 1200-grit SiC abrasive paper on all sides to avoid surface interactions, cleaned with deionized water, and dried with compressed air. Three samples per material were prepared for cyclic testing. Average surface areas were approximately 1.9 cm², and 3.3 cm² for AFA-3.8 and HP alloys respectively.

5.2.3 Experimental conditions

The cyclic test was constructed to mirror exposure to coking conditions seen in ethylene thermal cracking but with consideration to laboratory limitations. The key features included in the cyclic laboratory test were a) a preoxidation step which relates to the process encountered when new tubes are placed into service, and b) a periodic change between ethylene thermal cracking conditions and steam decoking conditions. The duration of coking and decoking times were shortened relative to production conditions. The overall flow of the laboratory cyclic test is shown in Figure 5.1. For reproducibility and a better assessment of the preoxidation data and cyclic data, three samples per material were exposed under the same tests conditions.

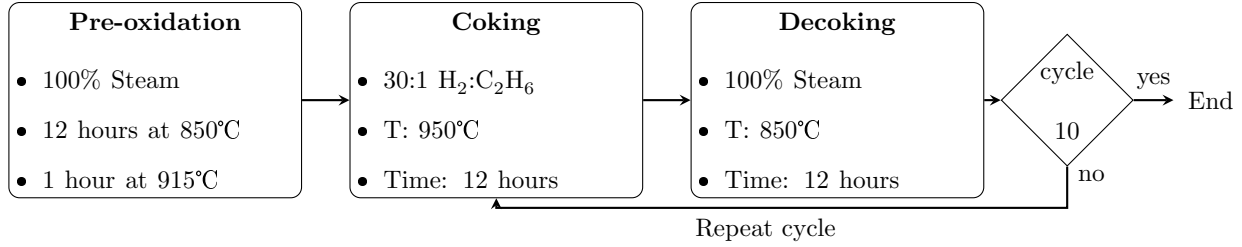


Figure 5.1: Schematic representation of the cyclic coking-decoking experiments

Coking-decoking cycle test

Coking tests were carried out using the apparatus described in Section 3.3.2, with the difference that, coking tests were done at 950 °C for 12 h each.

Decoking tests were carried out in the same tube furnace used for the preoxidation test and used identical parameters to create a steam atmosphere. Decoking was done at 850 °C for 12 hours, achieving a calculated oxygen partial pressure of 10^{-6} atm. Water flow rate was $0.5 \text{ mL}\cdot\text{min}^{-1}$, heating and cooling ramp rates were $10 \text{ }^{\circ}\text{C}\cdot\text{min}^{-1}$. Samples were exposed to the coking atmosphere for 12 hours. Then, they were cooled down to room temperature in the furnace. They were removed from the furnace and the mass was recorded. After each coking test, samples were transferred to the decoking furnace. After 12 hours of decoking exposure, samples were again cooled down to room temperature in the furnace, removed, and weighed. This process was carried out until all samples completed 10 coking-decoking cycles, achieving a total exposure of 120 hours of coking and 120 hours of decoking. Three samples of each alloy were processed simultaneously through all stages of the test.

5.2.4 Characterization

Samples were characterized in the as-cast, preoxidized, coked, and decoked states after 10 cycles for both the alumina-forming alloy (AFA-3.8) and the chromia-forming alloy (HP). Samples for surface analysis, optical microscopy, and microhardness tests were mounted into a black conductive thermosetting resin (Conductotherm 3000) and prepared using common

metallographic techniques.

Change of mass

Mass measurements after each coking and decoking step were made with a 0.01 mg resolution analytical balance. This allowed for the determination of the amount of coke deposited during every coking step as well as the removal of it, if any, during the decoking step. The reported values pertain to an average of three samples per material.

Microstructure analysis

XRD analysis was used to identify oxides, carbides and any other phases present at each stage for each material. Optical images were taken to identify the presence of carbides and width of carburized layer, if any, using a Zeiss Axiovert A1. For optical microscopy examination of the samples, a mixture of 20wt% of nitric acid and 4wt% hydrofluoric acid in distilled water was used as the etching solution^[74].

High magnification images of any developed oxide, intermetallics, and coked layers, were taken using scanning electron microscopy (SEM) to determine the continuity of the oxide layer, coke layer, or internal damage. For the elemental composition, energy dispersive x-ray spectrometry (EDS) mapping technique was performed. Each EDS scan was to track elemental data for the elements Al, O, Cr, C, Fe, Ni, and Nb, as this allowed for interpretation of the distribution of the oxide layer, carbon layer, any elemental mixtures, and the base metal. SEM and EDS were conducted with a JSM-6460 LV operating at an accelerating voltage of 15 keV, a working distance of ~13 mm, and a spotsize of 50.

Microhardness test

Microhardness tests were employed to characterize mechanical strength of the alloys after being exposed to cyclic coking-decoking atmospheres. Vicker hardness tests were performed using a Leco DM-400 Hardness Tester, with a test load of 200 gf. Vicker indentations were

made on cross-sections of the samples from the ID surface to a depth of approximately 1 mm with 0.08 mm intervals. Three indentations were taken at the same depth from the ID surface and averaged. A minimum of 0.2 mm spacing between any two indentations was maintained.

5.3 Results and Discussion

Three samples of each alumina-forming alloy and chromia-forming alloy were exposed to 10 coking-decoking cycles to simulate coking conditions often observed in ethylene thermal cracking operations. Alloys were preoxidized before cyclic testing with the intent of forming an oxide layer at the surface, same as the process encountered when new tubes are placed into service. Data collected and summarized in this section includes the microstructural analysis, change in mass, and mechanical property changes resulted from preoxidation and coking-decoking processing. Digital images of the samples after being preoxidized, coked, and decoked are shown in Figure 5.2.

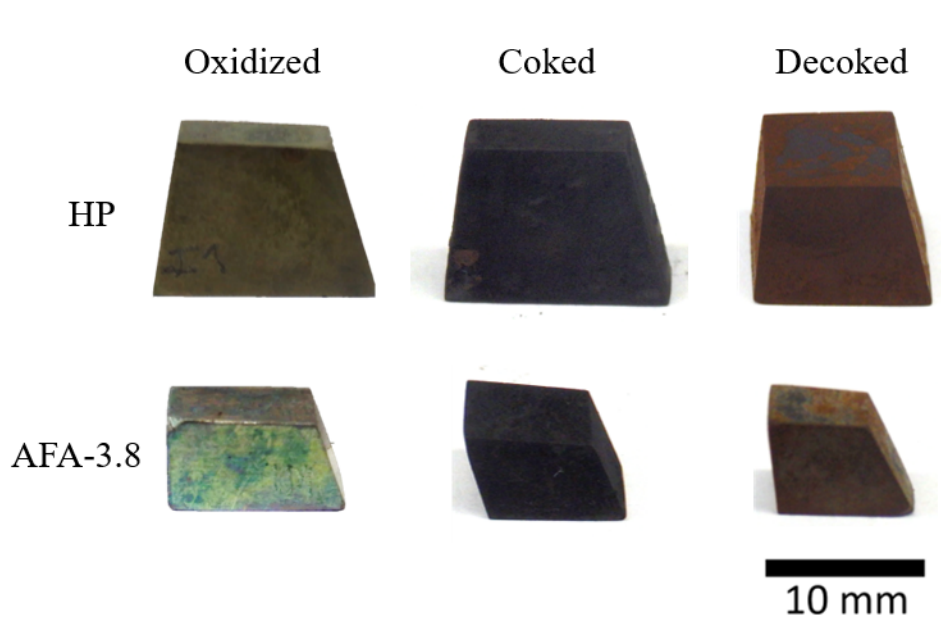


Figure 5.2: Digital images of alloys after each step in a coking-decoking cycle.

Change of mass

Mass measurements after each coking and decoking step were recorded to track the carbon deposition and carbon removal. The specific change in mass with respect to the initial mass of the alloy after preoxidation, is shown in Figure 5.3. On average, after 10 coking-decoking cycles, the alumina-forming alloy had 85% less mass gained than that of the chromia-forming alloy. The gain in mass was the result of 1) coking, 2) carburization, and 3) oxide growth. Some mass loss was observed upon decoking but not to the extent to where mass returned to pre-coked values. This indicates that some carburization may have occurred during the coking stage of the cycle, or some oxidation during the decoking stage. In practice, industrial observations have shown that after a decoking operation the amount of coking increases during the subsequent coking cycle^[10,55]. This phenomenon can be seen for the case of the HP alloy where the amount of coke deposited on the material seems to increase after each decoking procedure. However, this increment in mass is not as high for the AFA-3.8 alloy, where it reached a stable mass after cycle 5. Additionally, cooling samples to room temperature can induce structural deformations including the spalling of coke or oxide layers. No significant spallation was observed in the samples throughout the testing.

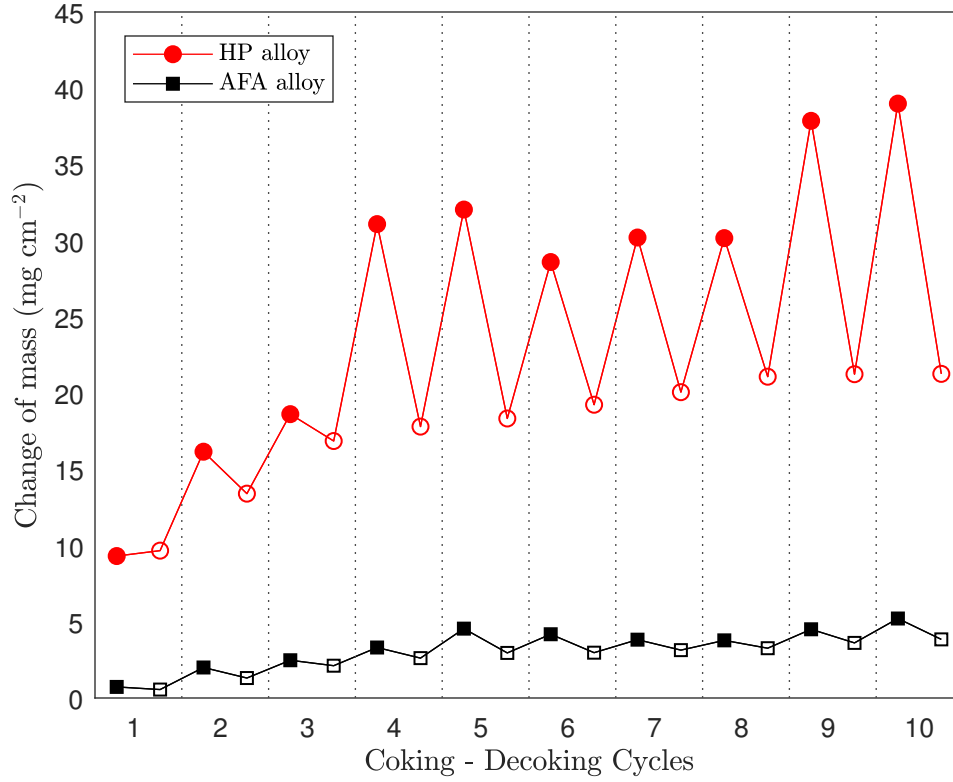


Figure 5.3: Specific change of mass per area for each coking-decoking cycle. Filled markers denote coking and open markers denote decoking step. Reported values correspond to an average of three samples per material and are relative to the initial mass of the alloy after preoxidation.

Microstructure analysis

XRD was performed at stages: as-cast, preoxidized, coking after cycle 10, and decoking after cycle 10. XRD analysis for both AFA-3.8 and HP surface alloys at each stage are shown in Figure 5.4.

After coking, XRD patterns showed the presence of carbon (graphite) for both alloys. The presence of carbon at the surface resulted from pyrolytic and catalytic coke formation from gas feedstock reactions, such as cracking of ethane^[10,13]. Similar investigations have confirmed the presence of coke and other surface alloy phases using XRD after 100 hours exposure to coking conditions^[87,88]. The thickness of the coke layer after 100 h of coking does not distort the XRD analysis to an extent where other phases cannot be detected. Therefore,

the uncertainty in the XRD analysis due to the distortion provided by the presence of coke at the surface is minimal.

In the case of the AFA-3.8 alloy, peaks for α - Al_2O_3 can be seen, indicating that oxidation during cyclic process has occurred and created an oxide layer detectable via XRD. The presence of chromium-rich carbides, both M_{23}C_6 and M_7C_3 type, can be seen in both alloys. Chromium-rich carbides were observed in the as-cast and preoxidized samples under SEM, but not at levels which were detected by XRD analysis. In the case of the HP alloy, no chromium oxide phase in the coked condition was detected by XRD. A change in the microstructure was noticeable for the HP alloy. The intensity of the carbide peaks, both M_{23}C_6 and M_7C_3 type, relative to the matrix was high, indicating that the chromia layer partially reduced during coking conditions and carburization occurred. This indicates that the oxide layer is not dense and protective over the whole surface of the HP alloy.

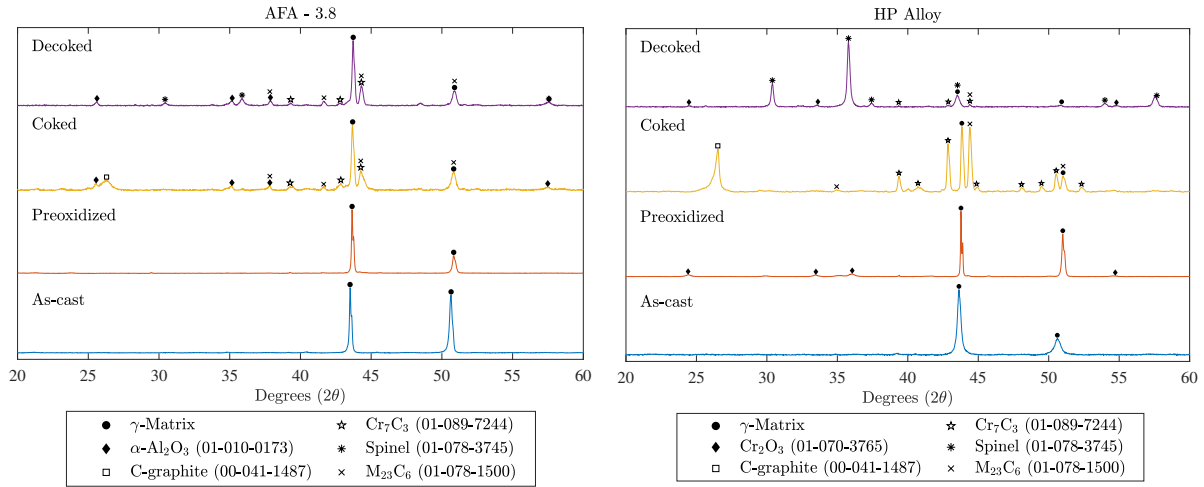


Figure 5.4: XRD analysis at each stage. Each pattern has been normalized between 0 and 1. JCPDS number of each pattern is shown next to its compound name. γ -Matrix has been associated to the as-cast microstructure.

Chromium-rich carbides were seen for both alloys after the final decoking process. XRD analysis of the HP alloy showed that a major change in microstructure occurred after decoking, predominantly peaks of spinel were observed in addition to the chromia. Investigations on HP alloys have shown that formation of spinel prevents the formation of chromia at the

surface, which is prone to spallation, and then carburization with the temperature changes weakening the alloy^[55]. The AFA-3.8 alloy showed no major changes in microstructure after decoking, though spinel was observed with the alumina oxidation product.

The presence of M_7C_3 carbides in the HP alloy is undesirable because it affects mechanical properties of the material. Internal carbide formation also means loss of oxidation resistance since the Cr is tied up with the carbides M_7C_3 and $M_{23}C_6$ and less available in the matrix^[25]. The presence of these phases indicates that the material is carburizing internally. Therefore, microstructural changes are occurring in the alloy, changing its overall performance when being exposed to coking-decoking cycles. In contrast to the HP alloy, the presence of M_7C_3 carbides in the AFA-3.8 alloy does not affect the availability of aluminum in the matrix for the formation of its main oxidation product, alumina.

Optical images for coked and decoked stages after the 10th coking-decoking cycle for both AFA-3.8 and HP alloys are shown in Figure 5.5 and Figure 5.6. After coking, the presence of a uniform carburized layer in the HP alloy was visible, reaching approximately 800 μm from the surface, indicating that carburization of the chromia-forming alloy has occurred. In contrast, the AFA-3.8 alloy does not have a uniform carburized layer. However, the presence of some localized areas where carburization started to occur was seen on the AFA-3.8 sample. These areas did not reach more than 250 μm in depth from the surface. These carburized areas could indicate that the protective oxide layer locally failed and carbon was able to diffuse into the base matrix. As seen in Figure 5.6, after decoking, carburized layer was still present in the HP alloy as well as the carburization areas in the AFA-3.8 alloy.

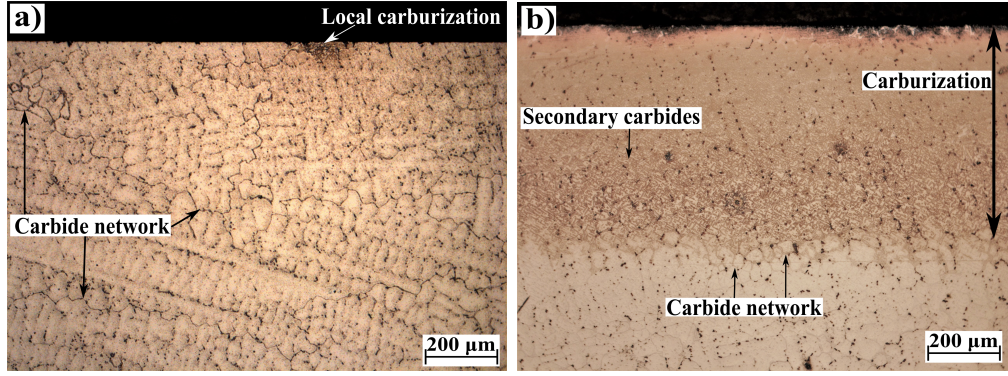


Figure 5.5: Optical microscopy images after coking cycle 10, for a) AFA-3.8-3.8 alloy and b) HP alloy.

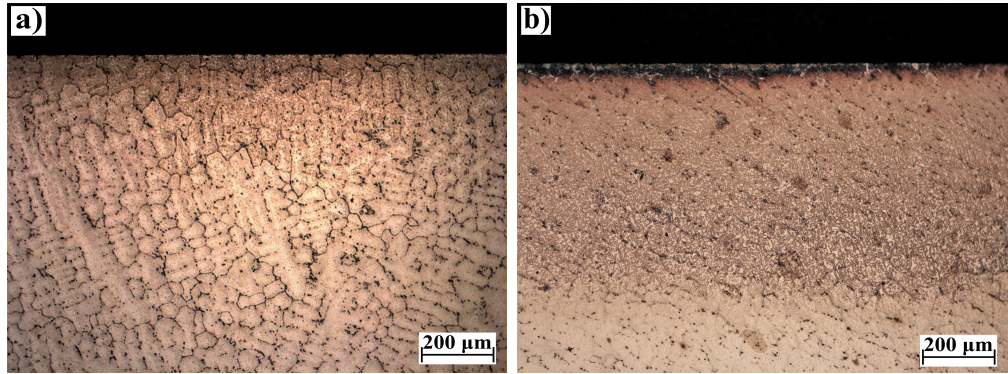


Figure 5.6: Optical microscopy images after decoking cycle 10 for a) AFA-3.8-3.8 alloy and b) HP alloy.

Because of microstructural changes derived from carbon diffusion and exposure to high temperature, a continuous network of chromium carbide can be seen at grain boundaries in both AFA-3.8 and HP alloys. Presence of secondary carbides, as seen in the HP alloy, grew inside the grains. As a result, chromium depletion happens adjacent to carbides and this concentration gradient of chromium drives migration of chromium from the matrix to carbides which makes the carbides coarser. Continuous carbide precipitation deteriorates the mechanical properties of the alloy, such as embrittlement of the alloy^[43].

SEM cross-sectional images of both AFA-3.8 and HP alloys after coking are shown in Figure 5.7. The coke layer at the surface of each alloy is visible, being thicker for the HP alloy. The AFA-3.8 alloy shows presence of the chromium-rich intermetallics or carbides (dark phase in the matrix), as well as Nb-rich carbides (bright phase in the matrix) (see

Figure 5.8). Additionally, some voids at the surface can be seen indicating that paths for carbon diffusion into the matrix formed. The HP alloy shows that the integrity of the oxide layer has been compromised during exposure to the cyclic conditions. The oxide layer in the HP alloy was not uniform and presented some localized damage. Underneath this layer, EDS analysis showed presence of Fe, Ni, Cr, and O, indicating that a spinel layer has developed as a consequence of the steam exposure during decoking steps (see Figure 5.9). This correlates to the presence of spinel in XRD analysis as previously discussed. It should be noted that these layers were not uniform across the entire surface of the HP alloy.

SEM cross-sectional images for each alloy after decoking are shown in Figure 5.10. The AFA-3.8 alloy showed an oxide layer, approximately 1 μm thick, indicating that oxidation occurred during exposure to the cyclic coking-decoking atmospheres. The carbon layer after decoking was visible, confirming that the decoking treatment is not removing all carbon gained from coking. However, the thickness of this carbon layer is larger for HP alloy than for AFA-3.8 alloy. The HP alloy showed that the oxide layer partially reduced or spalled off in local regions, with a thicker coke layer present in these areas. Additionally, the presence of coke and spinel in the surface lead to a highly carburized zone as seen in 5.10b.

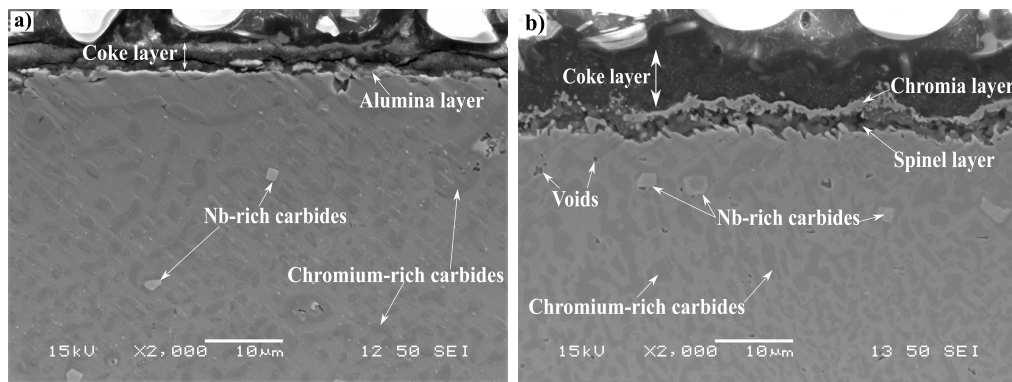


Figure 5.7: SEM cross sections after coking cycle 10, for a) AFA-3.8-3.8 alloy and b) HP alloy.

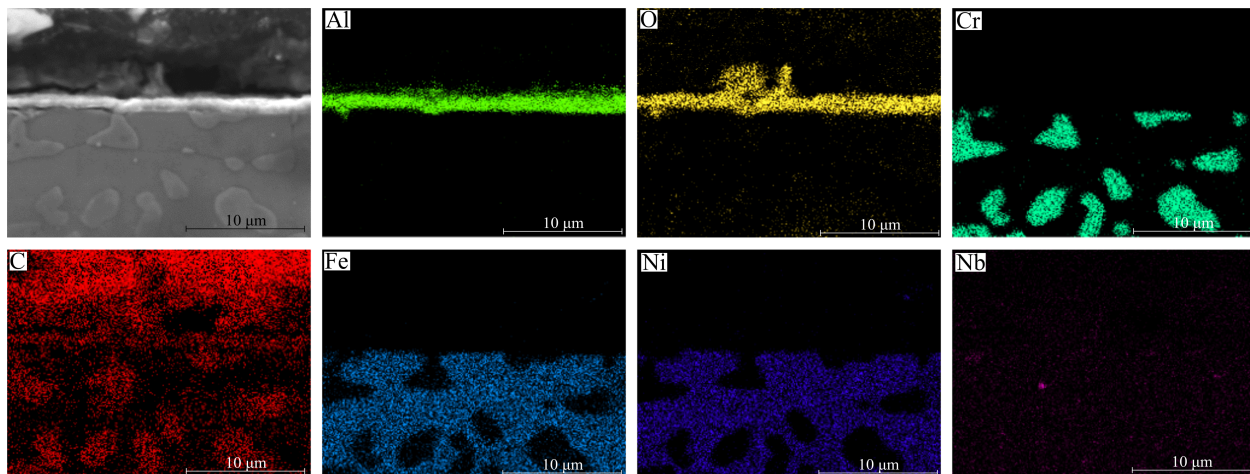


Figure 5.8: EDS mapping cross-section after coking cycle 10 for AFA-3.8 alloy.

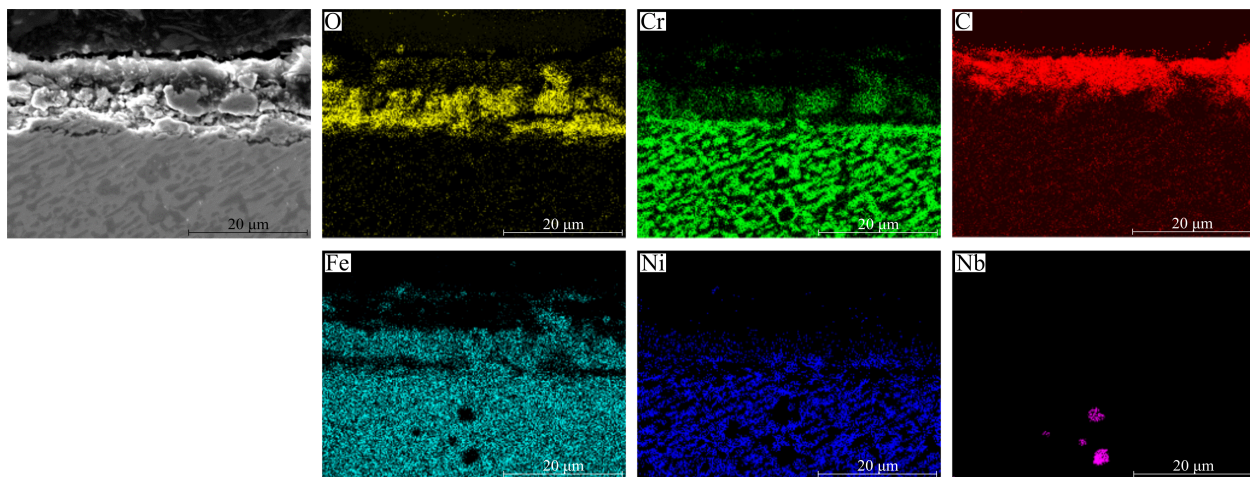


Figure 5.9: EDS mapping cross-section after coking cycle 10 for HP alloy.

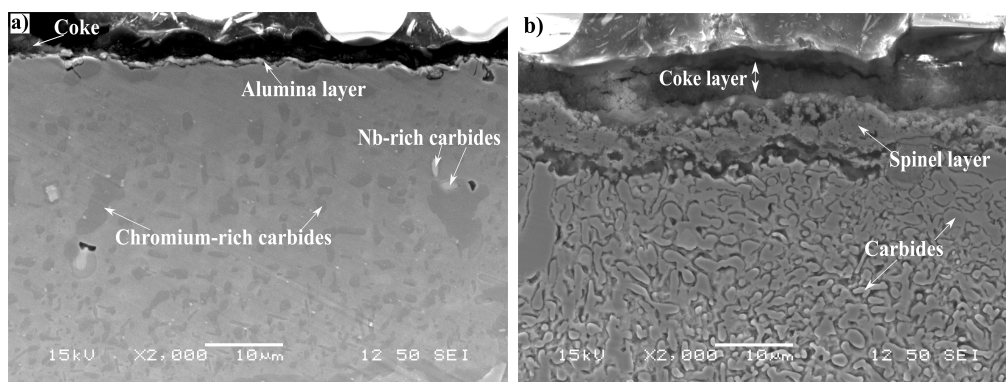


Figure 5.10: SEM cross sections after decoking cycle 10, for a) AFA-3.8 alloy and b) HP alloy.

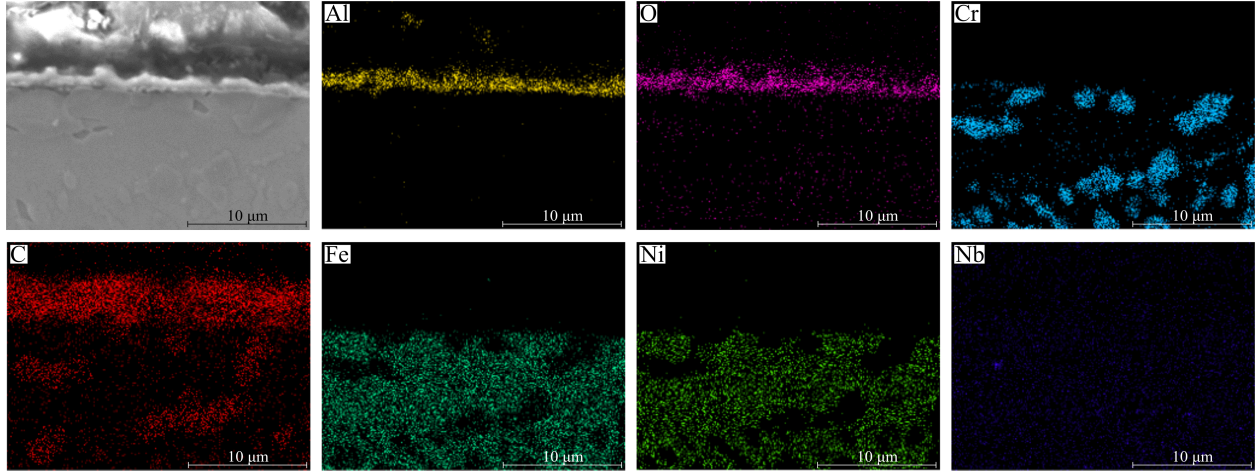


Figure 5.11: EDS mapping cross-section after decoking cycle 10 for AFA-3.8 alloy.

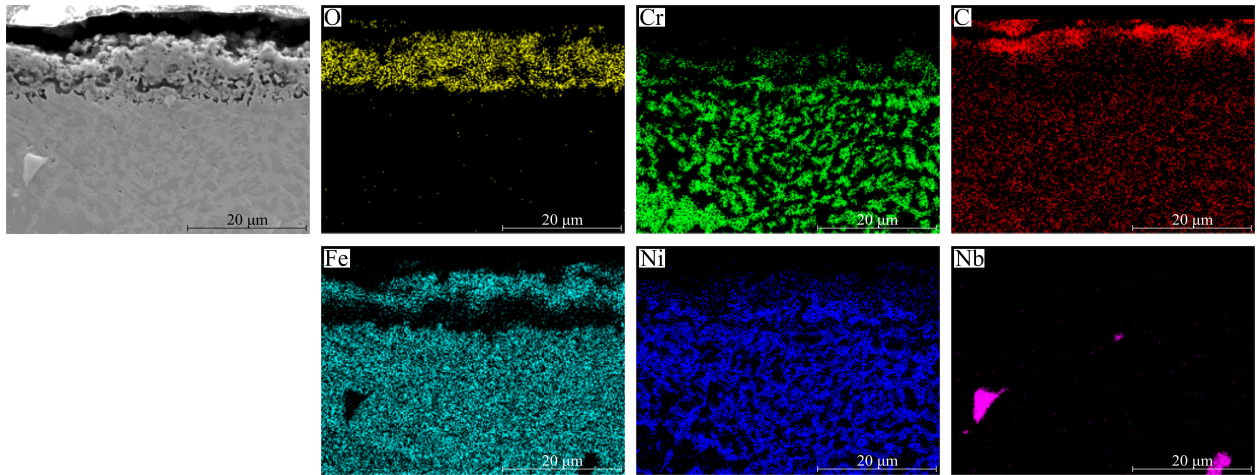


Figure 5.12: EDS mapping cross-section after decoking cycle 10 for HP alloy.

Microhardness test

Vickers microhardness measurements were performed on the samples in the as-cast, preoxidized, and coked/decoked after cycle 10. Microhardness results for both AFA-3.8 and HP alloys are shown in Figure 5.13. Both AFA-3.8 and HP alloy, showed an increase in the hardness after being exposed to the 10 coking-decoking cycles when compared to the as-cast or preoxidized states. The AFA-3.8 alloy, based on microhardness results, shows that hardening occurred to approximately 400 μm from the surface whereas the hardening in the HP alloy, occurred to approximately 900 μm from the surface. Then, carburization in the HP

alloy was as twice as in the AFA-3.8 alloy when being exposed to the same coking-decoking cyclic atmospheres.

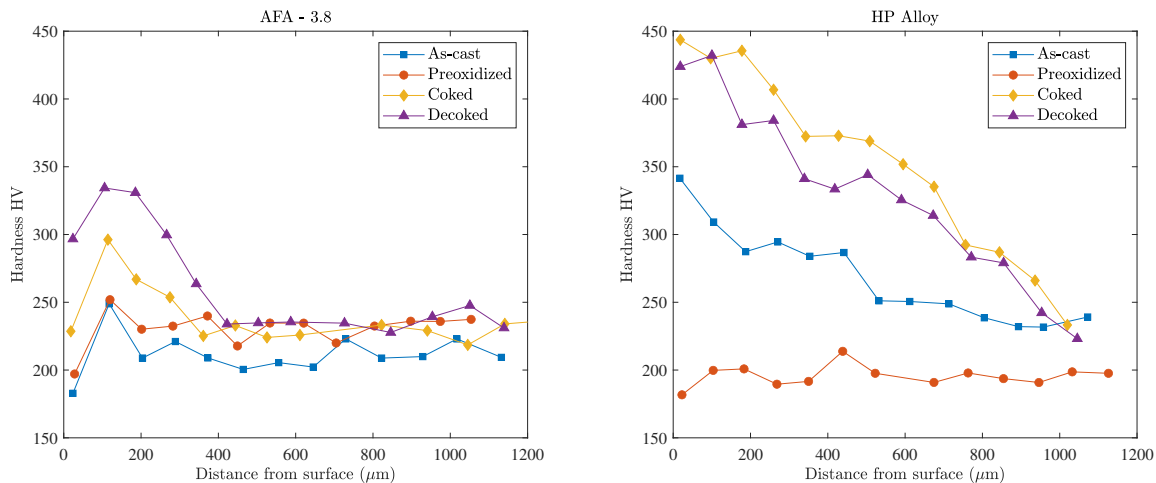


Figure 5.13: Microhardness distribution of each alloy at each stage.

The surface hardening of the alloys is a result of carburization. The microhardness measurements combined with microstructural observations, show that the carburization was more severe in the chromia-forming alloy than in the alumina-forming alloy. This carburization occurred because of the precipitation of Cr-rich carbides near the surface. Investigations have been shown that when a surface hardened layer forms in the HP alloy, the alloy loses the ability to form a continuous protective oxide scale, chromium oxide, on the surface^[61]. In contrast, the formation of Cr-rich carbides in the AFA-3.8 alloy should not affect the formation of the continuous oxide scale, aluminum oxide, as its formation does not depend on the chromium content of the alloy. Therefore, the precipitation of carbides in the HP alloy is greater detriment to the formation of a protective oxide scale than in the AFA-3.8 alloy.

5.4 Conclusions

Three samples of each alumina-forming alloy and chromia-forming alloy were exposed to 10 coking-decoking cycles to simulate coking conditions seen in ethylene thermal cracking.

Alloys were preoxidized before exposure to cyclic atmospheres, forming a continuous oxide scale at its surface. After exposure to 10 coking-decoking cycles, the AFA-3.8 alloy had 85% less mass gained than that of the HP alloy. Overall, the gain in mass in the alloys was the result of: 1) coking, 2) carburization, and 3) oxide growth. The change of mass for the HP alloy showed that the amount of coke deposited on the material increased after each decoking procedure. However, the AFA-3.8 alloy did not present this behavior and its mass reached a stable value after cycle 5.

XRD analysis for the AFA-3.8 alloy showed no major changes in microstructure and aluminum oxide and spinel were observed in the coked and decoked conditions. In the case of the HP alloy, XRD showed that a major change in microstructure occurred, where the intensity of the carbides peaks relative to the matrix was high after successive coking/decoking exposure.

SEM cross-section analysis showed a coke layer at the surface in both alloys with the layer being thicker for the HP alloy. After the decoking procedure, part of this coke layer remained at the surface. Therefore, a decoking treatment with 100% steam at 850 °C for 12 hours seems not to completely remove the coke layer. While the AFA-3.8 alloy had the presence of chromium-rich intermetallics or carbides in the alloy, the aluminum oxide scale at the surface remained in all test conditions. In contrast, the HP alloy showed that the chromium oxide layer formed during the preoxidation step, was not present after exposure to cyclic conditions. Instead, the HP material had a surface layer of spinel as detected by SEM/EDS.

Optical microscopy in the HP alloy revealed a carburization layer of approximately 800 μm in depth from the surface. The carburization of the HP alloy occurred along the entire surface of the sample while the AFA-3.8 alloy had only localized areas of carburization. Furthermore, carburization in the alumina-forming alloy was not as severe as in the chromia-forming alloy and extended only to a depth of 250 μm .

Microhardness tests on both alloys showed that hardening in the surface region occurred

after exposure to coking-decoking cycles. The hardening in the AFA-3.8 alloy was approximately 400 μm from the surface whereas the hardening in the HP alloy, occurred to approximately 900 μm from the surface. This hardening occurred because of precipitation of Cr-rich carbides near the surface.

Overall, the presence of carbides in the HP alloy is undesirable because it means loss of oxidation resistance since the Cr is tied up and less available in the matrix. In contrast to the HP alloy, the presence of these carbides in the AFA-3.8 alloy should not affect the production of the protective scale, aluminum oxide.

With less mass gained during coking, no major microstructural changes, and a better integrity of the oxide scale after exposure to 10 coking-decoking cycles, the AFA-3.8 alloy performed better than the HP alloy in these laboratory tests. The results indicate that a higher longevity of the reactor's material and a possible reduction in the number of coking-decoking cycles can be achieved when implementing alumina-forming alloys instead of chromia-forming alloys in applications where the material is exposed to repeated cycles of coking and decoking conditions.

Manufacturing variables and uniformity of oxide layer can contribute to an uncertainty about how representative the microhardness data is. Therefore, additional testing and further investigation of the mechanical properties in several samples should be done in order to understand how the microhardness changes after exposure to preoxidation, coking, and decoking atmospheres. By testing several samples from different sections of the as-cast pipe, a homogeneity of the results and a better understanding in the mechanical strength can be achieved.

Chapter 6

Conclusions

In this document, the coking resistance performance of several AFA alloys compared to a traditional HP alloy was described. Alloys were preoxidized before exposure to coking atmospheres, with the intent to form the oxide scale at the surface. Then, coking kinetics test were done at 900, 950, and 1000 °C for 100h. This allowed for the determination of coking kinetic parameters, and estimation of carbon diffusion coefficients at different temperatures. In addition, alloys were exposed for 1000 h to evaluate the long-term coking performance. Lastly, the performance in coking-decoking cyclic conditions was presented. Results included specific change of mass, microstructural analysis such as XRD, optical microscopy, SEM/EDS, and mechanical testing such as microhardness. Additionally, element profiles were obtained via EDS analysis allowing for estimation of carbon diffusion in the matrix.

A strong influence of the temperature and time was seen on the coking performance. With higher temperature and longer exposure times, alloys had a higher carburization and microstructural changes. The majority of the AFAs alloy showed ~80% better coking resistance than the HP alloy for all the tests. In general, the presence of carbides in the HP alloy is undesirable because it means loss of oxidation resistance and change in mechanical properties. However, the presence of these carbides in the AFA alloy should not affect the

production of the protective scale, aluminum oxide, allowing for less carbon deposited on the surface and therefore, less carbon diffusion into the matrix.

Coking kinetic parameters in a temperature range between 900 - 1000 °C were calculated for all alloys. Coking kinetics rate was found to follow a parabolic function for both alloys, indicating that kinetics rate is governed by a diffusion mechanism, most probably diffusion of carbon. Activation energies of 91.7, 201.5, 194.4, and 238.2 kJ·mol⁻¹ for the HP, AFA-3.2, AFA-3.5, and AFA-4.0 alloy, respectively, were obtained. On average, the AFA alloys had ~2.3 times the activation energy of the HP alloy, resulting in a better coking resistance.

An estimation of the carbon profiles was achieved by EDS analysis. The apparent carbon content in the alloy with respect to the surface increased with higher temperature. The higher apparent carbon content was associated with carburization attack and formation of Cr-rich carbides, that were confirmed by XRD and SEM analysis. While the AFA alloy had similar carbon content for all tests, the HP alloy showed a significant increment for samples exposed at 1000 °C and +500 h of exposure time.

Based on the obtained carbon profiles, the apparent carbon diffusion coefficients in the temperature range of 900 - 1000 °C have now been measured for both HP and AFA alloys under C₂H₆-H₂ coking conditions. For the HP alloy, the carbon diffusion coefficients were described best by Boltzmann-Matano analysis model, while for the AFA alloys, by Fick's second law solution model. For the HP alloy, the apparent carbon diffusion coefficient was to be found between 2.03 and 2.49 × 10⁻⁹ cm²·s⁻¹. In the case of AFA alloys, the diffusion coefficients were found to be between 1.65 × 10⁻⁹ and 5.24 × 10⁻⁸. The discrepancy in the obtained diffusivities when compared to literature was attributed to alloy composition, presence of a coke layer, presence of an oxide scale, and formation of precipitates.

Furthermore, samples were exposed at 950 °C for 1000 h to the same coking atmosphere to determine material performance. The kinetics at these condition followed a parabolic rate function, agreeing with data at shorter times. The integrity of the oxide layer after exposure to long-term conditions was evaluated by EDS and XRD analysis. Based on both

XRD and SEM analysis, a chromium oxide layer was not detected in the surface, indicating that the oxide layer was partially reduced or spallation occurred, allowing for carbon to diffuse and carburize the material. In contrast, the AFA alloys showed an alumina scale at the surface. XRD surface analysis showed aluminum oxide in all AFA samples, even after 1000 h of exposure. From SEM images, the oxide layer thickness was 2.5, 1.4, and 1.26 μm for the AFA-3.2, AFA-3.5, and AFA-4.0, respectively. Even though the AFA-4.0 had the thinnest oxide layer among the AFAs, the developed aluminum oxide scale had superior density, adherence, and uniformity across the surface. Then, because of the good oxide scale developed in the AFA-4.0 alloy, the mass flux of carbon in the alloy was less than the alloys with porous or reduced oxide scales, such as the case of the HP alloy, resulting in less carburization attack, and better coking resistance.

In addition, samples were exposed to 10 coking-decoking cycles. The AFA alloy had $\sim 85\%$ less mass gained than that of the HP alloy. The change in mass was the result of coking, carburization, and oxide growth. In addition, the amount of coke in the HP alloy increased continuously with each coking-decoking cycle, while the AFA alloy reached a stable value after cycle 5. After decoking, SEM analysis revealed presence of a coke layer at the surface, indicating that the decoking treatment needs to be improved.

Carburization attack was seen in all alloys after exposure to coking and coking-decoking atmospheres. In the coking atmosphere at 950°C , the carburization depth for the HP alloy was 515, 1903, and 800 μm , and for the AFA alloy with best performance (AFA-4.0) was 110, 431, and 250 μm , for the coking kinetics (100 h), long-term coking (1000 h), and cyclic test (10 cycles, with 120 h of total coking), respectively. Then, the carburization in AFA alloys was not as severe as in the HP alloy. The presence of Cr-rich carbides resulted from carburization is undesirable in the HP alloy because results in loss of oxidation resistance. In contrast, the presence of these carbides in the AFA alloys do not affect the production of the protective scale, aluminum oxide, resulting in a more stable oxide layer, and therefore, less coking and carburization attack.

Overall, with less mass gained, no major microstructural changes, and a better integrity of the oxide scale after exposure to different coking tests, the AFA alloys performed better than the HP alloy in these laboratory tests. The results indicate that a higher longevity of the reactor's material and a possible reduction in the number of coking-decoking cycles can be achieved when implementing alumina-forming alloys instead of chromia-forming alloys in applications such as thermal cracking operations.

6.1 Future work

Microstructural analysis can be improved by analyzing samples by using different techniques such as Electron Back-Scattered Diffraction (EBSD) and Electron Probe Micro-Analysis by X-Ray Wavelength Dispersive Spectroscopy (EPMA-WDS). EBSD can be used to distinct M_7C_3 from $M_{23}C_6$ carbides. EPMA-WDS can be used to determine the chemical composition of the carbide precipitates, and thus identify each phase.

The carbon diffusion coefficients for both HP and AFA alloys were estimated from apparent carbon diffusion profiles obtained by EDS means. An analysis of the carbon content in the alloy using a different technique, such as EPMA-WDS, allows for the detection and quantification of light elements like carbon. The use of this technique, can be used to quantify carbon in the alloy with respect to distance, that will result in a more accurate calculated apparent carbon diffusion coefficients.

Improvements in the experimental set-up, such as adding a gas analyzer will provide product yields that can better explain process reactions and its relation with alloy surface interactions. In addition, the development of a bench scale or pilot plant experimental set-up with more representative industrial conditions, will allow for better coking characterization and more accurate material's performance analysis.

Furthermore, studies on the performance of AFA alloys on coking atmospheres alternative feedstocks should be explored. The effect of added elements such as steam, sulfur, and

other compounds, which are typical in thermal cracking atmospheres, should be studied to determine if AFA alloys are equally resistant to coking when these compounds are added.

6.2 Acknowledgments

Electronic microscopy and X-ray diffraction were conducted at the University of Wisconsin-Milwaukee, Advance Analysis Facility. Sample materials were provided by MetalTek International and Duraloy Technologies. This work was sponsored by ARPA-E, DE-AR0000690.

Bibliography

- [1] CH Toh, PR Munroe, and DJ Young. Metal dusting of fe-cr and fe-ni-cr alloys under cyclic conditions. *Oxidation of metals*, 58(1-2):1–21, 2002.
- [2] Jianqiang Zhang and David J Young. Coking and dusting of fe-ni alloys in co-h₂-h₂o gas mixtures. *Oxidation of metals*, 70(3-4):189–211, 2008.
- [3] CM Chun, S Desai, F Hershkowitz, and Trikur A Ramanarayanan. Materials challenges in cyclic carburizing and oxidizing environments for petrochemical applications. *Mater. Corros.*, 65(3):282–295, 2014.
- [4] MS Shokrollahi Yancheshmeh, S Seifzadeh Haghighi, MR Gholipour, O Dehghani, MR Rahimpour, and S Raeissi. Modeling of ethane pyrolysis process: A study on effects of steam and carbon dioxide on ethylene and hydrogen productions. *Chem. Eng. J.*, 215:550–560, 2013.
- [5] Y. Nishiyama and N. Otsuka. Degradation of surface oxide scale on fe-ni-cr-si alloys upon cyclic coking and decoking procedures in a simulated ethylene pyrolysis gas environment. *Corrosion*, 61(1):84–93, 2005.
- [6] Michael P Brady, John Magee, Yukinori Yamamoto, David Helmick, and Lu Wang. Co-optimization of wrought alumina-forming austenitic stainless steel composition ranges for high-temperature creep and oxidation/corrosion resistance. *Materials Science and Engineering: A*, 590:101–115, 2014.

- [7] Rolf R Kirchheiner, Petra Becker, David J Young, Rick Durham, et al. Improved oxidation and coking resistance of a new alumina forming alloy 60 ht for the petrochemical industry. In *CORROSION 2005*. NACE International, 2005.
- [8] Peter Szakalos, M Lundberg, and R Pettersson. Metal dusting on an alumina forming ni-base alloy. *Corrosion Science*, 48(7):1679–1695, 2006.
- [9] Kathy Riggs Larsen. Alumina-forming austenitic alloys resist high-temperature corrosion. *Materials Performance*, 2015.
- [10] Stamatis A Sarris, Steffen H Symoens, Natalia Olahova, Kim Verbeken, Marie-Françoise Reyniers, Guy B Marin, and Kevin M Van Geem. Impact of initial surface roughness and aging on coke formation during ethane steam cracking. *Ind. Eng. Chem. Res.*, 56(44):12495–12507, 2017.
- [11] KM Sundaram and GF Froment. Modeling of thermal cracking kinetics—i: Thermal cracking of ethane, propane and their mixtures. *Chem. Eng. Sci.*, 32(6):601–608, 1977.
- [12] Benjamin Church, Lizeth Ortiz, Elmer Prenzlöw, and James Myers. High temperature coking resistance of an alumina forming alloy. *NACE Int. Corros. Conf. Expo*, 2017.
- [13] Haiyong Cai, Andrzej Krzywicki, and Michael C Oballa. Coke formation in steam crackers for ethylene production. *Chem. Eng. Process.*, 41(3):199–214, 2002.
- [14] A Serna and RA Rapp. Carburization of austenitic and ferritic alloys in hydrocarbon environments at high temperature. *Rev. Metal. (Madrid, Spain)*, pages 162–166, 2003.
- [15] Nickel Development Institute (Canada). *Heat and Corrosion Resistant Castings: Their Engineering Properties and Applications*. Publication (Nickel Development Institute (Canada)). NiDI, 1978.
- [16] Yingying Zhang, Wangfeng Cai, and Feng Xin. Simulation and optimization of coil decoking in ethane pyrolysis furnace. *Chem. Eng. Commun.*, 196(8):950–968, 2009.

- [17] S. R.J. Saunders, M. Monteiro, and F. Rizzo. The oxidation behaviour of metals and alloys at high temperatures in atmospheres containing water vapour: A review. *Prog. Mater. Sci.*, 53(5):775–837, 2008.
- [18] Michael P Brady, Yukinori Yamamoto, Michael L Santella, Philip J Maziasz, Bruce A Pint, CT Liu, ZP Lu, and Hongbin Bei. The development of alumina-forming austenitic stainless steels for high-temperature structural use. *JOM*, 60(7):12, 2008.
- [19] GD Barbela, Luiz Henrique de Almeida, TL Silveira, and IL May. Role of nb in modifying the microstructure of heat-resistant cast hp steel. *Materials Performance*, 26(3):193–197, 1991.
- [20] Yukinori Yamamoto, Michael P Brady, Michael L Santella, Hongbin Bei, Philip J Maziasz, and Bruce A Pint. Overview of strategies for high-temperature creep and oxidation resistance of alumina-forming austenitic stainless steels. *Metall. Trans. A*, 42(4):922–931, 2011.
- [21] Michael P Brady, Yukinori Yamamoto, Michael L Santella, and Bruce A Pint. Effects of minor alloy additions and oxidation temperature on protective alumina scale formation in creep-resistant austenitic stainless steels. *Scripta Materialia*, 57(12):1117–1120, 2007.
- [22] G Muralidharan, Y Yamamoto, MP Brady, LR Walker, HM Meyer III, and DN Leonard. Development of cast alumina-forming austenitic stainless steels. *JOM*, 68(11):2803–2810, 2016.
- [23] Yukinori Yamamoto, Michael L Santella, Michael P Brady, Hongbin Bei, and Philip J Maziasz. Effect of alloying additions on phase equilibria and creep resistance of alumina-forming austenitic stainless steels. *Metallurgical and Materials Transactions A*, 40(8):1868–1880, 2009.
- [24] Xiangqi Xu, Xiaofeng Zhang, Xiaoyang Sun, and ZP Lu. Roles of manganese in the

- high-temperature oxidation resistance of alumina-forming austenitic steels at above 800° c. *Oxidation of metals*, 78(5):349–362, 2012.
- [25] Hans Jürgen Grabke. Carburization, carbide formation, metal dusting, coking. *Mater. Tehnol.*, 36(6):297–306, 2002.
- [26] Sanjit Bhowmick, Gavin Lea, Atul Verma, and Prabhakar Singh. Assessment of chromium evaporation from chromia and alumina forming alloys. *Advances in Solid Oxide Fuel Cells VII*, pages 115–124, 2011.
- [27] Andres Muñoz Gandarillas. *Influence of the reactor coil material on coke formation during steam cracking of hydrocarbons*. PhD thesis, Ghent University, 2014.
- [28] Lizeth Ortiz, Kao Yang, and Benjamin Church. Performance of alumina-forming alloys under coking–decoking cycles. *Ind. Eng. Chem. Res.*, 59(25):11485–11493, 2020.
- [29] Hans Jürgen Grabke, Else Marie Müller-Lorenz, and André Schneider. Carburization and metal dusting on iron. *ISIJ international*, 41(Suppl):S1–S8, 2001.
- [30] Yukinori Yamamoto, Michael P Brady, Govindarajan Muralidharan, Bruce A Pint, Philip J Maziasz, Dongwon Shin, Benjamin Shassere, Sudarsanam Suresh Babu, and C-H Kuo. Development of creep-resistant, alumina-forming ferrous alloys for high-temperature structural use. In *Pressure Technology*, volume 40764, page V001T04A003. American Society of Mechanical Engineers, 2018.
- [31] GR Millward, HE Evans, M Aindow, and CW Mowforth. The influence of oxide layers on the initiation of carbon deposition on stainless steel. *Oxidation of metals*, 56(3):231–250, 2001.
- [32] Benjamin Church, Lizeth Ortiz, Elmer Prenzlöw, Shengyi Li, Bruna Luiza dos Santos, Bryce Erwin, and James Myers. An initial evaluation of the effect of alloy composition

- and oxide layer on high temperature coking resistance of heat resistant alloys. *NACE Int. Corros. Conf. Expo*, 2016.
- [33] YX Xu, JT Lu, WY Li, and XW Yang. Oxidation behaviour of nb-rich ni-cr-fe alloys: Role and effect of carbides precipitates. *Corros. Sci.*, 140:252–259, 2018.
- [34] Michael P Brady, Yukinori Yamamoto, Michael L Santella, and Larry R Walker. Composition, microstructure, and water vapor effects on internal/external oxidation of alumina-forming austenitic stainless steels. *Oxid. Met.*, 72(5-6):311, 2009.
- [35] Michael P Brady, Yukinori Yamamoto, Bruce A Pint, Michael L Santella, Philip J Maziasz, and Larry R Walker. On the loss of protective scale formation in creep-resistant, alumina-forming austenitic stainless steels at 900 c in air. *Mater. Sci. Forum*, 595:725–732, 2008.
- [36] Taymaz Jozaghi, Chung Wang, Raymundo Arroyave, and Ibrahim Karaman. Design of alumina-forming austenitic stainless steel using genetic algorithms. *Mater. Des.*, 186:108198, 2020.
- [37] Geneva Trotter, Bin Hu, Annie Y Sun, Reed Harder, MK Miller, Lan Yao, and Ian Baker. Precipitation kinetics during aging of an alumina-forming austenitic stainless steel. *Mater. Sci. Eng., A*, 667:147–155, 2016.
- [38] Istvan Kucora, Pera Paunjoric, Jasna Tolmac, Marko Vulovic, James G. Speight, and Ljiljana Z. Radovanović. Coke formation in pyrolysis furnaces in the petrochemical industry. *Pet. Sci. Technol.*, 35(3):213–221, 2017.
- [39] KM Sundaram and GF Froment. Kinetics of coke deposition in the thermal cracking of propane. *Chemical Engineering Science*, 34(5):635–644, 1979.
- [40] KM Sundaram, PS Van Damme, and GF Froment. Coke deposition in the thermal cracking of ethane. *AIChE Journal*, 27(6):946–951, 1981.

- [41] R. C. Yin, I. M. Allam, and A. Al-Farayedhi. Carburization behavior of 310 stainless steel in CH_4/H_2 gas mixture with trace amount of oxygen. *Oxid. Met.*, 60(3-4):315–333, 2003.
- [42] Bo Wang, Xianlong Gong, Ziduan Zhang, Quan Zhu, and Xiangyuan Li. Investigation on carburization during the repeated coking and decoking process. *Ind. Eng. Chem. Res.*, 59(29):13051–13059, 2020.
- [43] M Mobaraki, B Afshang, MR Rahimpour, ME Bahrololoom, A Bolhasani, and R Davand. Effect of cracking feedstock on carburization mechanism of cracking furnace tubes. *Eng. Failure Anal.*, 107:104216, 2020.
- [44] HM Tawancy. Correlation between resistance to carburization and resistance to oxidation of selected high-temperature alloys. *Oxid. Met.*, 83(1):167–185, 2015.
- [45] Carl M Schietekat, Stamatis A Sarris, Pieter A Reyniers, Lawrence B Kool, Wenqing Peng, Patrick Lucas, Kevin M Van Geem, and Guy B Marin. Catalytic coating for reduced coke formation in steam cracking reactors. *Ind. Eng. Chem. Res.*, 54(39):9525–9535, 2015.
- [46] D. J. Young. Carburization and metal dusting. *Shreir’s Corros.*, 4:272–303, 2010.
- [47] Andrés E Muñoz Gandarillas, Kevin M Van Geem, Marie-Françoise Reyniers, and Guy B Marin. Coking resistance of specialized coil materials during steam cracking of sulfur-free naphtha. *Ind. Eng. Chem. Res.*, 53(35):13644–13655, 2014.
- [48] MN Rosli and N Aziz. Simulation of ethane steam cracking with severity evaluation. *IOP Conf. Ser. Mater. Sci. Eng.*, 162(1):12017, 2016.
- [49] Marie Françoise S.G. Reyniers and Gilbert F. Froment. Influence of Metal Surface and Sulfur Addition on Coke Deposition in the Thermal Cracking of Hydrocarbons. *Ind. Eng. Chem. Res.*, 34(3):773–785, 1995.

- [50] Zou Reniun, Lou Qiangkun, Liu Huicai, and Niu Fenghui. Investigation of Coke Deposition during the Pyrolysis of Hydrocarbon. *Ind. Eng. Chem. Res.*, 26(12):2528–2532, 1987.
- [51] V. Van Speybroeck, K. Hemelsoet, B. Minner, G. B. Marin, and M. Waroquier. Modeling elementary reactions in coke formation from first principles. *Mol. Simul.*, 33(9-10):879–887, 2007.
- [52] SM Jazayeri and R Karimzadeh. A surface kinetic model for coke deposition over stainless steel, chromium, and iron during ethane pyrolysis. *Petroleum science and technology*, 32(7):821–829, 2014.
- [53] Seyed Mahdi Jazayeri and Ramin Karimzadeh. Experimental investigation of initial coke formation over stainless steel, chromium, and iron in thermal cracking of ethane with hydrogen sulfide as an additive. *Energy Fuels*, 25(10):4235–4247, 2011.
- [54] Steffen H Symoens, Natalia Olahova, Andrés E Muñoz Gandarillas, Hadiseh Karimi, Marko R Djokic, Marie Françoise Reyniers, Guy B Marin, and Kevin M Van Geem. State-of-the-art of coke formation during steam cracking: Anti-coking surface technologies. *Ind. Eng. Chem. Res.*, 57(48):16117–16136, 2018.
- [55] Andrés E Muñoz Gandarillas, Kevin M Van Geem, Marie Françoise Reyniers, and Guy B Marin. Influence of the reactor material composition on coke formation during ethane steam cracking. *Ind. Eng. Chem. Res.*, 53(15):6358–6371, 2014.
- [56] P. R.S. Jackson, D. L. Trimm, and D. J. Young. The coking kinetics of heat resistant austenitic steels in hydrogen-propylene atmospheres. *J. Mater. Sci.*, 21(9):3125–3134, 1986.
- [57] D. R.G. Mitchell and D. J. Young. A kinetic and morphological study of the coking of some heat-resistant steels. *J. Mater. Sci.*, 29(16):4357–4370, 1994.

- [58] Kevin M. Van Geem, Inge Dhuyvetter, Serge Prokopiev, Marie Françoise Reyniers, Dominique Viennet, and Guy B. Marin. Coke formation in the transfer line exchanger during steam cracking of hydrocarbons. *Ind. Eng. Chem. Res.*, 48(23):10343–10358, 2009.
- [59] H. M. Tawancy. On the comparative degradation of selected Cr₂O₃-forming alloys by high-temperature carburization with a case study involving 310 stainless steel. *Eng. Fail. Anal.*, 110(October 2019):104402, 2020.
- [60] G. F. Samaras and G. N. Haidemenopoulos. Carburization of high-temperature steels: A simulation-based ranking of carburization resistance. *Eng. Fail. Anal.*, 51:29–36, 2015.
- [61] Anwar Ul-Hamid, Hani M Tawancy, Said S Al-Jaroudi, AI Mohammed, and Nured-din M Abbas. Carburisation of fe–ni–cr alloys at high temperatures. *Mater. Sci.-Pol.*, 24(2/1):319–331, 2006.
- [62] Hadi Ebrahimifar and Morteza Zandrahimi. Evaluation of the parabolic rate constant during different types of oxidation tests for spinel coated Fe-17%Cr alloy. *Oxid. Met.*, 75(3-4):125–141, 2011.
- [63] Patrice Berthod. Influence of chromium carbides on the high temperature oxidation behavior and on chromium diffusion in nickel-base alloys. *Oxid. Met.*, 68(1-2):77–96, 2007.
- [64] Anjali Talekar, Dhanesh Chandra, Raja Chellappa, Jaak Daemen, Nobumichi Tamura, and Martin Kunz. Oxidation kinetics of high strength low alloy steels at elevated temperatures. *Corros. Sci.*, 50(10):2804–2815, 2008.
- [65] G. M. Smith, D. J. Young, and D. L. Trimm. Carburization kinetics of heat-resistant steels. *Oxid. Met.*, 18(5-6):229–243, 1982.

- [66] C. M. Chun, T. A. Ramanarayanan, and J. D. Mumford. Relationship between coking and metal dusting. *Mater. Corros. - Werkstoffe und Korrosion*, 50(11):634–639, 1999.
- [67] A Chauhan, M Anwar, K Montero, H White, and W Si. Internal carburization and carbide precipitation in fe-ni-cr alloy tubing retired from ethylene pyrolysis service. *J. Phase Equilibria Diffus.*, 27(6):684–690, 2006.
- [68] F. Ernst, A. Avishai, H. Kahn, X. Gu, G. M. Michal, and A. H. Heuer. Enhanced carbon diffusion in austenitic stainless steel carburized at low temperature. In *Metall. Mater. Trans. A Phys. Metall. Mater. Sci.*, volume 40, pages 1768–1780. Springer, jun 2009.
- [69] Xiaoting Gu, Gary M. Michal, Frank Ernst, Harold Kahn, and Arthur H. Heuer. Concentration-dependent carbon diffusivity in austenite. *Metall. Mater. Trans. A Phys. Metall. Mater. Sci.*, 45(9):3790–3799, 2014.
- [70] John Ågren. A revised expression for the diffusivity of carbon in binary FeC austenite. *Scr. Metall.*, 20(11):1507–1510, 1986.
- [71] Philippe Thibaux, A. Métenier, and C. Xhoffer. Carbon diffusion measurement in austenite in the temperature range 500 °C to 900 °C. *Metall. Mater. Trans. A Phys. Metall. Mater. Sci.*, 38(6):1169–1176, jun 2007.
- [72] Seok Jae Lee, David Kidder Matlock, and Chester John Van Tyne. An empirical model for carbon diffusion in austenite incorporating alloying element effects. *ISIJ Int.*, 51(11):1903–1911, 2011.
- [73] ASTM. Astm a297 / a297m-19, standard specification for steel castings, iron-chromium and iron-chromium-nickel, heat resistant, for general application. Technical report, ASTM International, 2019.

- [74] Tm0498-2018 evaluation of the carburization of alloy tubes used for ethylene manufacture. Technical report, 2018.
- [75] EM Müller-Lorenz and HJ Grabke. Coking by metal dusting of steels. *Mater. Corros.*, 50(11):614–621, 1999.
- [76] S. Liu, Q. Q. Guo, X. F. Wu, J. Shen, L. L. Liu, and Y. Niu. Carburization of three fe-19ni-21cr-xal ($x = 0, 2, 6$ at.%) alloys at 900 °c in oxygen-contaminated ch₄/h₂ atmospheres. *Corros. Sci.*, 111:436–445, 2016.
- [77] C Steurbaut, HJ Grabke, D Stobbe, FR Van Buren, SJ Korf, and Jacques Defrancq. Kinetic studies of coke formation and removal on hp40 in cycled atmospheres at high temperatures. *Mater. Corros.*, 49(5):352–359, 1998.
- [78] Hadiseh Karimi, Bolaji Olayiwola, Hany Farag, and Kimberley B. McAuley. Modelling coke formation in an industrial ethane-cracking furnace for ethylene production. *Can. J. Chem. Eng.*, 98(1):158–171, 2020.
- [79] J. Laigo, F. Christien, R. Le Gall, F. Tancrét, and J. Furtado. SEM, EDS, EPMA-WDS and EBSD characterization of carbides in HP type heat resistant alloys. *Mater. Character.*, 59(11):1580–1586, 2008.
- [80] I Wolf, HJ Grabke, and P Schmidt. Carbon transport through oxide scales on fe-cr alloys. *Oxidation of Metals*, 29(3):289–306, 1988.
- [81] DJ Young and J Zhang. Carbon corrosion of alloys at high temperature. *Journal of the Southern African Institute of Mining and Metallurgy*, 113(2):149–154, 2013.
- [82] SANDRA Wauters and GB Marin. Kinetic modeling of coke formation during steam cracking. *Ind. Eng. Chem. Res.*, 41(10):2379–2391, 2002.
- [83] Lyle F Albright. Comments on “kinetic modeling of coke formation during steam cracking”. *Ind. Eng. Chem. Res.*, 41(24):6210–6212, 2002.

- [84] Stamatis A Sarris, Natalia Olahova, Kim Verbeken, Marie Françoise Reyniers, Guy B Marin, and Kevin M Van Geem. Optimization of the in situ pretreatment of high temperature ni–cr alloys for ethane steam cracking. *Ind. Eng. Chem. Res.*, 56(6):1424–1438, 2017.
- [85] J Zhang, A Schneider, and G Inden. Characterisation of the coke formed during metal dusting of iron in co–h₂–h₂o gas mixtures. *Corrosion Science*, 45(6):1329–1341, 2003.
- [86] DJ Young. Kinetic and morphological development of coke formation on heat-resistant alloys. *Mater. Corros.*, 50(12):675–680, 1999.
- [87] Hao Li, Yanjun Zheng, Leslie W Benum, Mike Oballa, and Weixing Chen. Carburization behaviour of mn–cr–o spinel in high temperature hydrocarbon cracking environment. *Corros. Sci.*, 51(10):2336–2341, 2009.
- [88] Hao Li and Weixing Chen. High temperature carburization behaviour of mn–cr–o spinel oxides with varied concentrations of manganese. *Corros. Sci.*, 53(6):2097–2105, 2011.

Curriculum Vitae

Education

- **PhD in Engineering – Materials Science**

University of Wisconsin-Milwaukee, May 2021

Advisor: Benjamin Church

Dissertation topic: Performance of Centrifugally Cast Austenitic Alumina-Forming Alloys in Coking and Decoking Environments

- **Master of Science in Engineering – Materials Science**

University of Wisconsin-Milwaukee, May 2017

Advisor: Benjamin Church

Thesis: Coking Resistance of Alumina-forming cast austenitic Stainless Steels

- **Bachelor of Science - Chemical Engineering**

Universidad Nacional de Colombia – Sede Bogotá, Aug 2015

Publications

- Ortiz, L., & Church, B. Rate of Coke Formation of Centrifugally Cast Austenitic Alumina-Forming Alloys in Coking Conditions. Submitted for review. 2021

- Ortiz, L., Yang, K., & Church, B. Performance of Alumina-Forming Alloys under Coking–Decoking Cycles. *Ind. Eng. Chem. Res.* 59(25), 11485-11493. 2020
- Ortiz Reyes, Lizeth Nayibe, "Coking Resistance of Alumina Forming Cast Austenitic Stainless Steels", 2017. Theses and Dissertations. 1520.
- Church, B., Ortiz, L., Prenzlöw, E., & Myers, J. High Temperature Coking Resistance of an Alumina Forming Alloy. In *CORROSION 2017*. NACE International. 2017
- Church, B., Prenzlöw, E. A., Ortiz, L., & Myers, J. Oxidation Kinetics of Cast Alumina-Forming Austenitic Alloys in Steam. In *CORROSION 2017*. NACE International. 2017
- Church, B., Ortiz, L., Prenzlöw, E., Li, S., dos Santos, B. L., Erwin, B., & Myers, J. An Initial Evaluation of the Effect of Alloy Composition and Oxide Layer on High Temperature Coking Resistance of Heat Resistant Alloys. In *NACE International Corrosion Conference Proceedings* (p. 1). NACE International. 2016

Departmental Assistanships

- TA Manager and Materials Lab Manager. MatlEng 201 - Materials Engineering Lab, and MatlEng 330 - Manufacturing and Processing of Materials Lab. (Fall 2019, Fall 2021)
- Lecturer. MatlEng 443 - Transport Phenomena in Materials Processing. (Spring 2019, Spring 2020)
- Lecturer. MatlEng 330 - Manufacturing and Processing of Materials Lab. (Summer 2019)
- TA MatlEng 201 - Materials Engineering Lab. (Fall 2017, Spring 2018, Fall2018)

Mentoring

- 2020 – 2021: SURF Undergraduate Mentoring. Characterization of alumina-forming alloys exposed to decoking atmospheres.
- 2019 – 2020: SURF Undergraduate Mentoring. Study of the effect of environment in decoking procedures. Participation in CEAS Poster competition Spring 2020. Third place
- 2018-2019: SURF Undergraduate Mentoring. Effect of environment on the oxide layer formation in AFA vs CFA materials. Participation in CEAS Poster competition Spring 2019. Student's choice
- 2017-2018: SURF Undergraduate Mentoring. Mechanical work and recrystallization in Alumina-Forming alloys designed for coking resistance. CEAS Poster Competition Spring 2018. First Place and Student's choice
- 2017 – 2018: International Mentor. Work with UWM International Office mentoring new incoming international students.

Honors, Awards and Scholarships

- Hispanic Professionals of Greater Milwaukee (HPGM) – Scholarship 2020-2021
- Chancellor award: Spring 2018, 2019-2020, 2020-2021 academic years
- CEAS Poster Competition Spring 2019 – Honorable Mention
- FEF Scholarship: Spring 2018
- UWM Victor Vega Scholarship: Spring 2016, Spring 2018
- UWM Advanced Analysis Facility Seminar competition award: Fall 2017
- TMS AIME Henry deWitt Smith Scholarship: Spring 2017

Volunteering

- UWM Virtual Tutoring: Virtual tutoring for K5 students in Math and Spanish. 80 hours. 2020 - 2021
- UWM Materials Advantage Chapter: I promoted and volunteered in events where science demonstrations, such as making ice cream with liquid nitrogen were done to motivate high school students to pursue college studies. Additionally, I participated in engineering camps for Girl Scouts, and high school students (with ASM Milwaukee).
- EastBrook Church – “International Dinner”. I have been helping for the past year making the dinner, coordinating the food, and receiving students every Friday for an International dinner.